Partial quenching of electronic Raman scattering in double-wall carbon nanotubes by interlayer coupling

Dmitry Levshov, Marina Avramenko, Maksiem Erkens, Huy-Nam Tran, Thi Thanh Cao, van Chuc Nguyen, Emmanuel Flahaut, Valentin Popov, Ahmed-Azmi Zahab, Jean-Louis Sauvajol, et al.

To cite this version:

Dmitry Levshov, Marina Avramenko, Maksiem Erkens, Huy-Nam Tran, Thi Thanh Cao, et al.. Partial quenching of electronic Raman scattering in double-wall carbon nanotubes by interlayer coupling. Carbon, 2023, 203, pp.801-812. 10.1016/J.CARBON.2022.12.003 . hal-03929855

HAL Id: hal-03929855
https://cnrs.hal.science/hal-03929855v1

Submitted on 12 Jan 2023

Partial quenching of electronic Raman scattering in double-wall carbon nanotubes by interlayer coupling

Dmitry I. Levshov[1,2,3,], Marina V. Avramenko[1,3], Maksiem Erkens[1], Huy-Nam Tran[2], Thi Thanh Cao[4], Van Chuc Nguyen[4], Emmanuel Flahaut[5], Valentin N. Popov[6], Ahmed-Azmi Zahab[2], Jean-Louis Sauvajol[2], Raul Arenal[7,8,9], Wim Wenseleers[1], Sofie Cambré[1], Matthieu Paillet[2]*

[1]Nanostructured and Organic Optical and Electronic Materials, Department of Physics, University of Antwerp, B-2610 Antwerp, Belgium

[2]Laboratoire Charles Coulomb, Université de Montpellier, CNRS, F-34095, Montpellier, France

[3]Department of Nanotechnology, Faculty of Physics, Southern Federal University, 5, Zorge Street, Rostov-on-Don, 344090, Russia

[4]Institute of Materials Science, Vietnam Academy of Science and Technology, 18 Hoang Quoc Viet, Hanoi, Vietnam

[5]CIRIMAT, CNRS-INP-UPS, Université Toulouse 3 Paul Sabatier, 118 route de Narbonne, F-31062 Toulouse cedex 9, France

[6]Faculty of Physics, University of Sofia, BG-1164, Sofia, Bulgaria

[7]Instituto de Nanociencia y Materiales de Aragon (INMA), CSIC-U. de Zaragoza, 50009 Zaragoza, Spain

[8]Laboratorio de Microscopias Avanzadas (LMA), Universidad de Zaragoza, 50018 Zaragoza, Spain

[9]ARAID Foundation, 50018 Zaragoza, Spain

---

[*] Corresponding author: Tel: +32 3 265 24 79; Email: dmitry.levshov@uantwerpen.be

KEYWORDS: double-wall carbon nanotubes, electronic Raman scattering, van der Waals interaction, interlayer coupling, structural characterization

Abstract

Measuring electronic Raman scattering (ERS) has become an efficient method for structural characterization of metallic single-wall carbon nanotubes (SWCNT). However, applying this method to other types of SWCNT-based structures, *e.g.*, those with strong van der Waals (VDW) coupling, is currently not well studied. In this work, we combine electron diffraction, Rayleigh and Raman spectroscopies to investigate the ERS process near 36 metallic transitions in 21 individual double-wall carbon nanotubes (DWCNTs) with all types of electronic configurations. We observe the partial suppression of ERS intensity in DWCNTs compared to SWCNTs and mainly attribute it to the effect of dielectric screening of Coulomb interactions. We probe ultra-pure macroscopic multi-chirality DWCNT solutions and identify the role of inhomogeneous broadening in observing ERS peaks in Raman spectra. Based on the experimental findings, we propose an adapted method for the structural identification of DWCNT samples from the ERS data. The obtained results can be generalized to the characterization of the emerging 1D VDW heterostructures based on metallic SWCNTs.

Graphical Abstract:

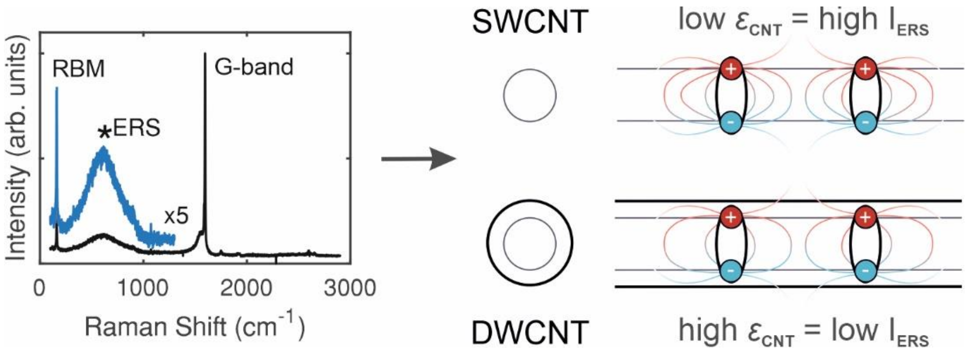

1. Introduction

Knowing the atomic structure of nanomaterials is essential for their applications in modern science and technology, as even slight structural variations will result in distinct physical properties. One typical example is a single-wall carbon nanotube (SWCNT), a quasi-one-dimensional cylindrical crystal, conceptually obtained by rolling up a sheet of graphene [1]. Two geometrically similar SWCNTs can be either metallic (M) or semiconducting (SC), differing only in one carbon atom along their circumferences. This difference, however, essentially defines the area of application: whether in digital electronics requiring at least 99.99% purity of SC-SWCNTs [2], as high-performance interconnects based on M-SWCNTs [3], or as nanoscale electromagnets, inductors, and transformers demanding particular coaxial combinations of both M- and SC-SWCNTs [4].

Identifying the SWCNT structure is possible either through microscopy-based techniques [5–7] or through spectroscopic methods [8–10]. One of the most powerful and non-invasive approaches relies on optical spectroscopy [8]. It is routinely performed using infrared photoluminescence excitation (PLE) spectroscopy [8,11], absorption spectroscopy [12], resonant Raman spectroscopy (RRS) [9,13], or their combinations [14]. RRS is particularly important since it provides both excitonic and vibrational information about SWCNTs [15,16] but requires measuring Raman spectra at multiple excitation energies for full characterization accuracy.

Recently, an alternative SWCNT identification method was proposed providing information about excitonic resonances from a single wide-range Raman spectrum, which is based on registering the so-called electronic Raman scattering (ERS) in individual metallic [17–19] or semiconducting [20] SWCNTs. The ERS is associated with electronic transitions [21] as opposed to vibrational transitions in conventional RRS and has been employed extensively in other fields, *e.g.*, as an ultra-sensitive probe for strain effects in semiconductors [22] or for determining band gap magnitudes and nodes in superconductors [23,24]. In SWCNTs, such electronic transitions originate from the inelastic scattering of photoexcited excitons by the low-energy excitons from the linear band of M-SWCNTs or by high-energy E_{11} excitons of SC-SWCNTs. The ERS manifests itself in Raman spectra as a broad dispersive line located between 0 and 4000 cm^{-1} for M-SWCNTs [19] or around 6000 - 9000 cm^{-1} for SC-SWCNTs [20]. Although the Raman shift of the ERS varies with the laser excitation wavelength, its absolute scattered energy is always equal to the energy of the excited E_{ii} transition. Saito *et al.* proposed a detailed theoretical description of the ERS process, highlighting the spectral changes originating from the interference between ERS and Raman-active phonons [25,26]. Note that ERS peaks have also been observed in the low-frequency region (between 0-10 cm^{-1}) of the anti-Stokes Raman spectrum of SC-SWCNTs, but they were assigned to a different mechanism, namely, scattering by single-particle excitation [27].

The ERS-based structural characterization of SWCNTs was shown to be robust due to its weak sensitivity to local variations in the nanotube environment [13,19]. However, it is unclear whether it can be extended for characterizing the emerging one-dimensional van-der-Waals (VDW) heterostructures [28–30] based on SWCNTs. For instance, the VDW coupling was shown to significantly affect the electronic, optical and vibrational properties of double-wall carbon nanotubes (DWCNT) [31], which can be viewed as the simplest 1D VDW structure comprised of two concentric SWCNTs [30]. The electronic VDW coupling modulates the excitonic energies [32] or leads to the appearance of entirely new optical transitions [33–36], while efficient interlayer energy transfer is proposed to quench the inner layer photoluminescence (PL) [37,73]. On the other hand, the mechanical VDW coupling is responsible for new collective vibrations [10,38] and frequency shifts due to internal pressure [39,40].

The current knowledge of the effect of VDW coupling on the ERS is incomplete. ERS has so far not been detected in DWCNTs due to the general difficulty of its observation and the lack of individual samples with precisely defined chirality. Although much progress has been made recently in the sorting of DWCNTs [41], *e.g.*, sorting the DWCNTs by metallicity of the constituting layers, it is not yet possible to achieve single-chirality purity of DWCNTs on a macroscopic scale. In this work, we therefore measure the ERS in 21 well-identified individual suspended DWCNTs with different electronic configurations, structurally characterized by electron diffraction (ED) or all-optical methods. We observe the partial suppression of ERS intensity in DWCNTs compared to SWCNTs and discuss it in terms of the effect of dielectric screening, interlayer energy and charge transfers. Afterwards, we investigate the ERS in ultra-pure macroscopic and mixed-chirality DWCNT solutions where ERS is hardly observed due to the effects of inhomogeneous broadening and polydispersity in chiral structures. Finally, based on the experimental findings, we propose an adapted method for the structural characterization of DWCNT samples from the ERS data.

2. Materials and methods

2.1 Synthesis of individual free-standing DWCNTs: Ultralong individual DWCNTs were grown by the CCVD method directly across open slit structures (~50×1000 μm^2) fabricated on silicon substrates ((100) orientation, 200 μm thick) with a 90 nm thick SiO_2 layer, according to the method described in Ref. [42].

2.2 Preparation of macroscopic UP-DWCNT sample: The pristine DWCNT powder (batch R281010) was synthesized following the method of Ref. [43]. It was purified from MgO-supported catalytic particles using the acid treatment and then solubilized in D_2O (99.8%, Cortecnet) with 2 wt./V% of sodium deoxycholate (DOC, 99%, Acros Organics) at a concentration of 4 mg CNT powder per ml surfactant solution, using only gentle magnetic stirring, avoiding ultrasonication. Finally, the DWCNT sample was purified from SWCNT impurities remaining from the synthesis by density gradient ultracentrifugation. More details are given in Ref. [44].

2.3 High-resolution electron microscopy and Electron Diffraction: HRTEM images and ED patterns were recorded in a FEI Titan Cube microscope (equipped with a spherical aberration corrector) operating at 80 kV and within short acquisition times (less than 5 s for ED) to reduce damage induced by electron diffraction.

2.4 Rayleigh spectroscopy: Rayleigh spectra of individual free-standing DWCNTs were measured in a backscattering geometry using a cross-polarization scheme with a Fianium supercontinuum laser as a light source and a fiber-fitted QE-Pro Ocean Optics spectrometer for detection.

2.5 Raman spectroscopy of free-standing DWCNTs: Resonant micro-Raman scattering measurements were performed in a backscattering configuration on two separate homemade setups including an iHR550 Jobin-Yvon spectrometer (gratings with 1200 or 1800 grooves/mm) and an Acton SP2500 spectrometer (grating with 1800 grooves/mm), both equipped with a liquid-nitrogen-cooled silicon CCD detectors. The first system was used for the NIR tunable measurements, while the second for the measurements in the visible range. The home-made microscopes in both systems were equipped with 100x objectives (numerical aperture = 0.95). The samples were mounted on a three-axis piezo-electric stage (PIMars P-563, Physik Instrumente) to ensure the precise positioning and focusing of the laser spot. Incident excitations from various continuous-wave lasers were used: HeNe at 632.8 nm (1.96 eV), diode-pumped solid-state lasers at 457 nm (2.71 eV), 532 nm (2.33 eV) and 561 nm (2.21 eV), and a Ti-Sapphire with a tunable laser line filter in the NIR (700 – 885 nm; 1.4 – 1.77 eV). To avoid heating effects, we kept the laser intensity impinging the sample below 40 kW/cm^2.

2.6 Raman spectroscopy of macroscopic UP-DWCNTs: Resonant Raman spectroscopy was performed with a Dilor XY800 triple spectrometer (gratings with 1800 grooves/mm) in backscattering geometry equipped with a liquid nitrogen-cooled CCD detector. For the near-infrared excitation wavelengths (695 nm – 855 nm), a tunable Ti:sapphire laser (Spectraphysics, model 3900S) pumped by a 5 W Ar$^+$-laser (Spectra Physics, model 2020) was used. The range 670 – 690 nm was covered by a dye laser (Spectra Physics, model 375) equipped with the dye DCM (4-(Dicyanomethylene)-2-methyl-6-(4-dimethylaminostyryl)-4H-pyran). The excitation wavelength was increased in approximately 5 nm steps. The laser power variations between the spectra were corrected using a tetrachloromethane (CCl_4) reference sample, which is transparent throughout the entire wavelength range and thus exhibits non-resonant Raman scattering. In addition, all of the Raman spectra were corrected for the setup's sensitivity and the spectrometer's wavelength calibration.

3. Results

3.1 Experimental observation of ERS in individual free-standing DWCNTs

The optical signals present in the Raman spectra of DWCNTs may vary depending on the purity and environmental interaction in the probed samples. The latter can be in the form of as-grown DWCNT powders [45], mixed-chirality or partially sorted DWCNT dispersions [41,46], individual DWCNTs on substrates [47] or DWCNTs suspended over open slits [16,48]. The first two sample types often contain impurities like SWCNTs, whose optical response may be confused with the signal from DWCNTs [49,50]. In addition, the intrinsic DWCNT optical properties can be drastically changed through the interaction with the environment, *e.g.*, due to unintentional doping of nanotubes lying on substrates [51] or through strain [52]. In this work, to exclude the majority of the extrinsic effects and thoroughly control the probed samples' purity, we investigate individual DWCNTs grown by the catalytic chemical vapor deposition technique (CCVD) over open slits. As demonstrated previously [48], this approach allowed us to combine Rayleigh spectroscopy, Raman spectroscopy, and ED measurements on the same free-standing parts of a DWCNT (Fig. 1a).

First, we identify the atomic structure of individual suspended DWCNTs by analyzing the ED patterns or by combining Rayleigh and Raman spectroscopic information [10,14] (further details in the Supporting Information (SI) Section S1). Having determined the DWCNT chiral indices, we then estimate the layers' optical resonance energies by referring to the atlas of SWCNT electronic transitions [53]. The transition energy shifts induced by the interlayer VDW electronic coupling in the inner and outer DWCNT layers were calculated using the approach of Chalin *et al.* [35]. This coupling modulates optical resonances by shifting them from -200 to +50 meV [32,54] or even creating new intertube resonances absent in isolated layers [33–35]. Using the calculated data as input parameters, we then fitted the DWCNT Rayleigh spectra with a complex optical susceptibility function $\omega^3|\chi|^2$ (see Section S5). An example of such deconvolution of the Rayleigh spectrum is shown in Figure 1b for (14,1)@(15,12) DWCNT, where we detect five optical resonances in the visible range corresponding to the M_{11L}^{out} (~1.44 eV), M_{22L}^{out} (~2.61 eV) and M_{22H}^{out} (~2.69 eV) transitions of the outer metallic layer (blue lines; L and H stand for lower and higher transitions) and the S_{22}^{in} (~1.54 eV) and S_{33}^{in} (~2.44 eV) transitions and their electron-phonon sidebands (*e.g.*, at ~1.72 eV) of the inner semiconducting layer (orange lines). To confirm the transition energy assignments for metallic layers, we measured the RBLM and G-band Raman spectra at the incoming ($E_{laser} = E_{ii}$) and outgoing (*e.g.*, $E_{laser} = E_{ii} + \hbar\omega_G$) resonance conditions (Figure 1c). The observation of a broad LO mode [39,55] proved the presence of the metallic layer, as is the case for the G-band spectra of (15,12) metallic layer at 1.46 and 2.71 eV (incoming resonance) and 1.65 eV (outgoing resonance) in Figure 1c. The complete set of fitted Rayleigh spectra and RBLM and G-band spectra for all studied DWCNTs are presented in the SI Section S2.

We then probed the ERS signals of the identified metallic transitions by measuring wide-range Raman spectra from ~80 to ~3000 cm^{-1} at multiple excitation energies from near-infrared (NIR) to ultra-violet for each characterized DWCNT. Overall, we investigated 36 metallic resonances in 15 DWCNTs with different electronic configurations, summarized in SI Section S1. Some typical examples of ERS peaks are shown in Figure 1d for SC@M, M@SC, and M@M DWCNTs. The Raman spectra are multiplied to highlight the ERS features relative to the intense phonon peaks (in blue in comparison with the original black spectra; the multiplication factor is provided).

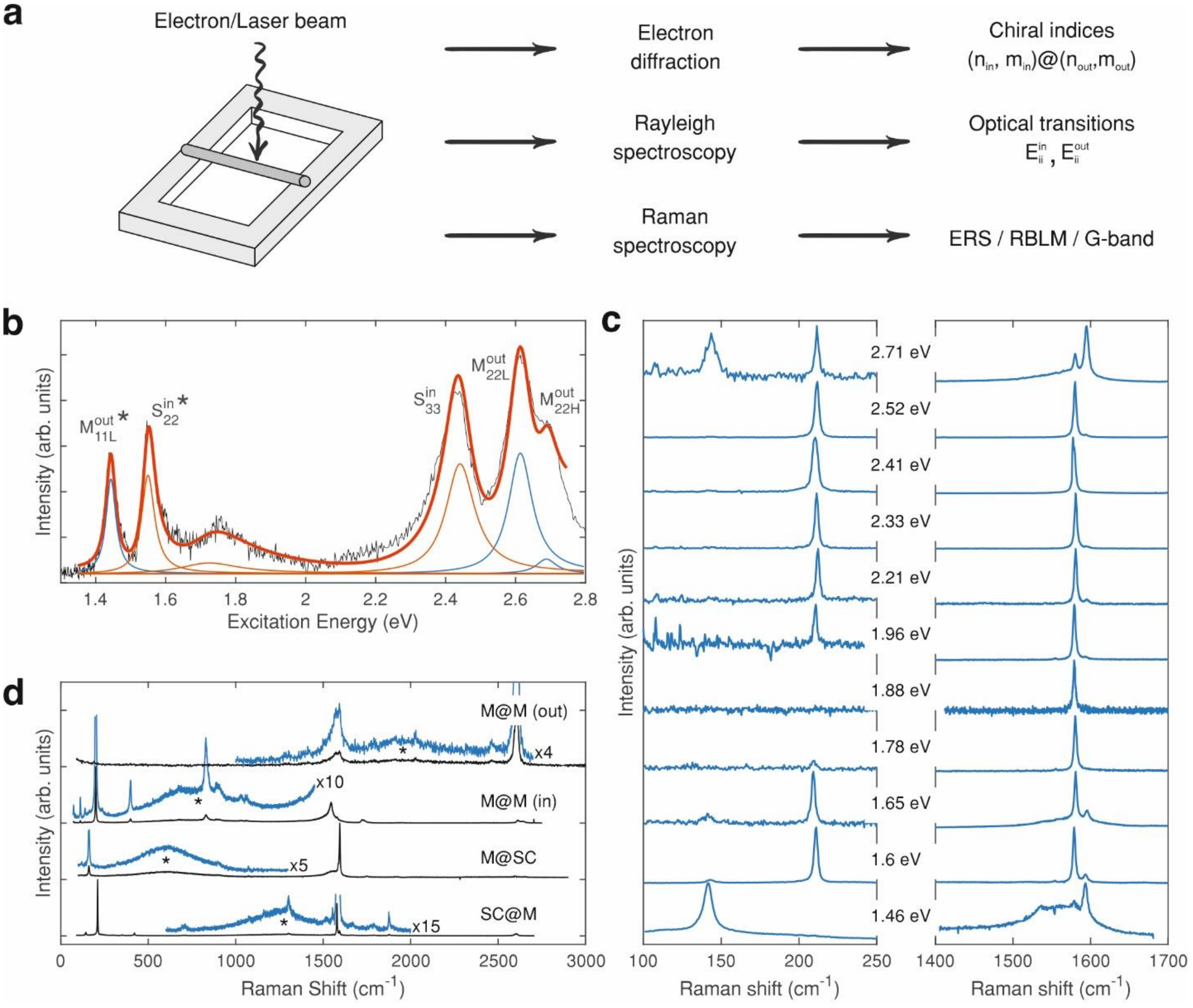

Figure 1. (a) Schematics of the experimental approach. (b) Experimental (black) and fitted (red) Rayleigh spectra showing the individual fitted transitions of the metallic (blue) and semiconducting (orange) layers in the (14,1)@(15,12) DWCNT. The asterisk shows two possible positions of M_{11H} transition (see SI Section S4). (c) Excitation energy dependence of RBLM and *G*-band regions of the Raman spectra of the individual (14,1)@(15,12) DWCNT. (d) ERS lines (marked by stars) in DWCNTs with different electronic configurations (from bottom to top): SC@M (14,1)@(15,12), M@SC (14,8)@(19,14), M@M (14,2)@(22,4) (inner layer in resonance), M@M (11,8)@(19,10) (outer layer in resonance) excited at 1.60, 1.66, 1.96 and 1.60 eV,

respectively. The Raman spectra are shown, either normalized on the intensity of the strongest peak (black) or scaled (blue), in order to highlight the ERS signal (with the given multiplication).

We summarize the observed behavior of ERS in all studied DWCNTs in Figure 2. It is best illustrated by two distinctive cases of (14,1)@(15,12) and (22,13)@(39,2) DWCNTs. For the former (Figure 2a), we detect almost all metallic transitions as ERS peaks in the Raman spectra: the M_{11L}^{out} is visible when exciting at 1.60 and 1.65 eV, and M_{22L}^{out} and M_{22H}^{out} when exciting at 2.71 eV. The M_{11H}^{out} is not clearly resolved and can overlap either with M_{11L}^{out} or S_{22}^{in} transitions as shown by an asterisk (see SI Section S4 for the discussion of two possible attributions, however considering one or the other doesn't change the conclusions drawn here). On the other hand, all ERS peaks around 2.2 eV in the (22,13)@(39,2) DWCNT are suppressed, independent of the laser excitation energy (M_{22L}^{in} and M_{22H}^{in} in Figure 2b). To quantitatively describe this suppression, we fitted ERS peaks in 79 available wide-range Raman spectra and presented the ERS intensity (peak height) in relation to the intensity of the broad LO mode of the metallic layer, *i.e.*, I_{ERS}/I_{LO} (arguments for representing the data in this form and details of the fitting procedure are given in the Sections S6-S7 in the SI). We find that the I_{ERS}/I_{LO} ratio in DWCNTs rapidly decays when increasing the difference between the laser energy E_{laser} and the energy E_{ii} of the excited transition (Figure 2c, bottom panel). Therefore, it becomes challenging to resolve ERS features within the noise level or distinguish them from the intense Raman modes when Raman spectra are excited more than 200-300 meV above the optical transition, *i.e.*, when the ERS peak falls in the range between *G*- and *2D*-bands.

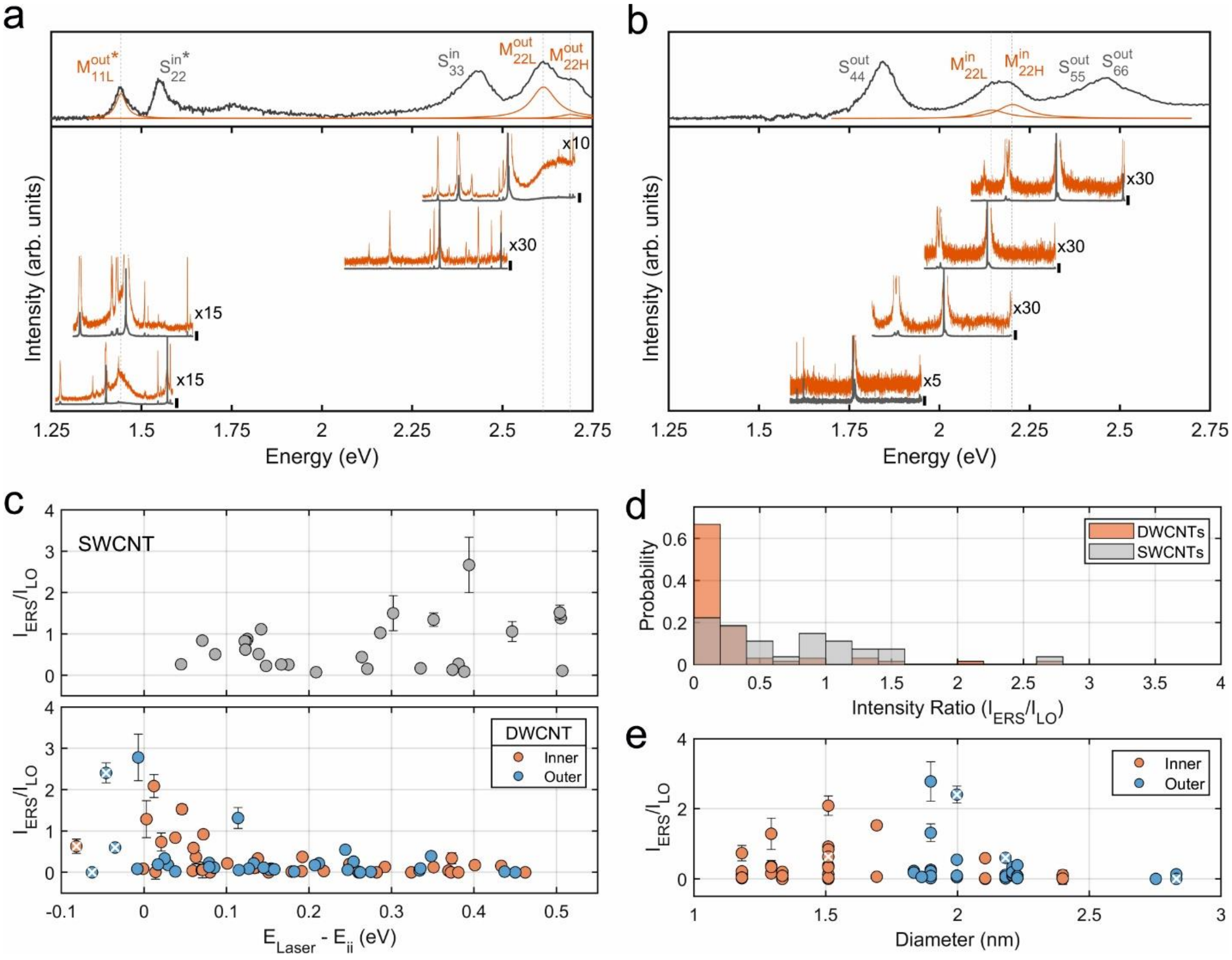

Figure 2. Details of the Electronic Raman scattering process in individual DWCNTs. The Rayleigh (top) and Raman spectra (bottom) of individual DWCNTs (a) (14,1)@(15,12) and (b) (22,13)@(39,2). The spectra were measured at 1.60, 1.65, 2.52 and 2.71 eV for (a) and at 1.96, 2.21, 2.33 and 2.52 eV for (b), counting from bottom to top. These laser excitation energies are marked by black vertical bars on the right side of each spectrum. The Raman spectra are plotted in absolute energy scale so that the ERS peak positions can be directly compared to the metallic transitions in the corresponding Rayleigh spectra. Raman spectra are multiplied (orange lines) by a certain factor to emphasize the ERS features among stronger phonon peaks. The asterisk in (a) shows two possible positions of M_{11H}^{out} transition (see SI Section S4); (c) Dependence of the I_{ERS}/I_{LO} ratio on the difference between laser energy E_{laser} and optical transition energy E_{ii} in individual

suspended SWCNTs (top panel) and DWCNTs (bottom panel). White crosses indicate data points with E_{Laser} - E_{ii} < -0.01 eV obtained through a simultaneous fit of ERS peak tails in Stokes Raman spectra (SI Section S6; peak linewidths and positions in these cases were fixed by the parameters of the same ERS lines in other spectra with E_{Laser} - E_{ii} > 0) and do not correspond to Anti-Stokes Raman spectra. The SWCNT data points were taken from Refs. [17–19]. The error bars for DWCNTs correspond to two standard deviations; (d) Intensity distribution of I_{ERS}/I_{LO} ratio for SWCNTs (gray bars) and DWCNTs (orange bars) (data from (c) except for data points with E_{Laser} - E_{ii} < -0.01 eV); (e) Dependence of the I_{ERS}/I_{LO} ratio on the diameter for inner and outer layers (orange and blue dots, respectively). The white crosses have the same meaning as in (c).

In general, we find that the ERS signal in DWCNTs has lower intensities than in isolated metallic SWCNTs, as is clear from comparing the intensity distributions in Figure 2d. For instance, the I_{ERS}/I_{LO} ratios in DWCNTs (orange bars) are mainly distributed below 0.5, while those in SWCNTs (gray bars) have a more slowly-varying distribution up to a value of 1.5. Moreover, we can directly compare I_{ERS}/I_{LO} ratios for three DWCNT layers, which were probed as individual SWCNTs in Refs. [17–19], namely (11,8), (14,2) and (14,5) (see Table 1). When compared under similar excitation (resonance) conditions, the I_{ERS}/I_{LO} ratios for six optical transitions are at least a factor of two lower in DWCNTs than in SWCNTs (see Section S9 for further discussion of this comparison). In one case, namely the M_{11L} transition of the (14,5) layer, the ERS peak was completely quenched in the DWCNT.

Furthermore, we find no noticeable difference between the ERS behavior in the inner and outer DWCNT layers, represented by orange and blue dots in Figure 2e, respectively. Both cases are characterized by the strong influence of the resonance effect (represented by the vertical spread of the points for the given diameter) and the significant suppression of the ERS signal in large diameter layers (> 2.3 nm). The dependences of the I_{ERS}/I_{LO} ratio on the other DWCNT structural parameters, namely interlayer distance $\Delta r = (d_{out} - d_{in})/2$, chiral angle θ and interlayer twist angle $\Delta\theta = |\theta_{in}|-|\theta_{out}|$, are given in the Section S10 with similar conclusions as made from Figure 2e.

Table 1. Comparison of I_{ERS}/I_{LO} ratios for selected *(n,m)* chiralities measured as individual SWCNTs [18,19] or as layers of DWCNTs. For each *(n,m)* chirality, the diameter *d*, chiral angle θ, type of optical transition, laser excitation energy E_{laser}, experimental transition energy E_{ii} and energy separation $dE = E_{laser} - E_{ii}$ are given. $R_{DW/SW}$ corresponds to the ratio of (I_{ERS}/I_{LO}) in DWCNT to the (I_{ERS}/I_{LO}) in SWCNT.

#	*(n,m)*	***d*** **(nm)**	***θ*** **(°)**	**Trans.**	**CNT**	E_{laser} **(eV)**	E_{ii} **(eV)**	***dE*** **(eV)**	I_{ERS}/I_{LO}	$R_{DW/SW}$
1	(11,8)	1.29	24.8	M_{11L}	SW	2.33	1.94	0.39	2.67 ± 0.67	0.06 (±0.03)
					DW	2.33	1.90	0.43	0.16 ±0.07	
2	(11,8)	1.29	24.8	M_{11H}	SW	2.33	2.03	0.30	1.50 ±0.43	0.23 (±0.11)
					DW	2.33	1.96	0.37	0.34 ±0.13	
3	(14,2)	1.18	6.6	M_{11L}	SW	2.33	1.95	0.30	0.28 ±0.01	0.43 (±0.05)
					DW	2.21	1.86	0.35	0.12 ±0.01	
4	(14,5)	1.34	14.7	M_{11L}	SW	2.33	1.83	0.50	1.38 ±0.06	0.13 (±0.07)
					DW	2.21	1.81	0.40	0.18 ±0.10	
5	(14,5)	1.34	14.7	M_{11L}	SW	1.96	1.84	0.12	0.83 ±0.02	0.00
					DW	1.96	1.81	0.15	0.00	
6	(14,5)	1.34	14.7	M_{11H}	SW	2.33	2.07	0.26	0.44 ±0.04	0.46 (±0.09)
					DW	2.21	1.96	0.25	0.20 ±0.03	

3.2 Tunable wavelength study of the ERS process in individual free-standing DWCNTs.

Although analyzing the behavior of ERS lines in terms of I_{ERS}/I_{LO} intensity ratios provides a quick practical way to compare SWCNT and DWCNT data, it has a certain drawback, namely the ratio depends not only on the intrinsic properties of the ERS process but also on the intensity variations of the LO phonon peaks. For instance, quantum interference between exciton states in the *G*-band excitation profiles was previously reported for SWCNTs [56] and DWCNTs [57], manifesting in the peculiar intensity variation of the *G*-band lines.

To avoid the influence of *G*-band properties, we analyze the evolution of the ERS peak's integrated intensity (peak area) instead of intensity ratios with the excitation energy. We measured the Raman excitation maps (REM) in the range between RBLM and *G*-band, as shown in Figure 3a,c for DWCNTs (14,1)@(15,12) and (18,6)@(21,14), respectively. The maximum intensities in Figures 3a,c are chosen in such a way to highlight the ERS peaks; hence RBLM and *G*-band regions appear saturated (dark red color). We fitted the spectra of the REM simultaneously using a set of Lorentzians (peak parameters were shared between the spectra) and neglecting the interference effects [25] between the ERS and phonon lines for simplicity (see details in Section S6). The ERS, RBLM and LO integrated intensities extracted from the REM fits are presented as filled symbols in Figures 3b,d.

In addition, we calculated the absorption spectra of (14,1)@(15,12) and (18,6)@(21,14) DWCNTs within an *ab initio*-based non-orthogonal tight-binding (NTB) approach [34], which allowed us to clarify the positions of the M_{ii} transitions within the measured excitation range (see Section S4, Tables S4.1 and S4.2). By combining these calculations and the experimental behavior of LO and TO REPs, we find that the M_{11H}^{in} transition is overlapping with M_{11L}^{in} in (18,6)@(21,14) DWCNT and with M_{11L}^{out} or S_{22}^{in} transitions in (14,1)@(15,12) DWCNT (shown by the asterisks in Figure 3b). Based on these transition energy assignments, we fitted the RBLM and LO Raman excitation profiles (REP) using the approach of Tran *et al.* [57] accounting for the interference between M_{11L} and M_{11H} transitions. The results of the fit are shown as solid lines in the bottom panels of Figures 3b,d. In contrast to RBLM and LO modes, we fitted the ERS REP using a single

Lorentzian component. We find that the evolution of the ERS integrated intensity has one common feature for two investigated DWCNTs: it rapidly decays with the increase of the laser excitation energy. Hence, the ratio of the ERS and LO integrated intensities should tend to very small values with the increase of $E_{laser} - M_{ii}$, which reflects well the behavior observed in Figure 2c for DWCNTs. The only deviation from this trend may occur when the LO integrated intensity vanishes between the incoming and outgoing resonances (*e.g.*, at 1.59 eV in Figure 3b or 1.65 eV in Figure 3d) leading to the high values of the I_{ERS}/I_{LO} ratio despite the low ERS intensity.

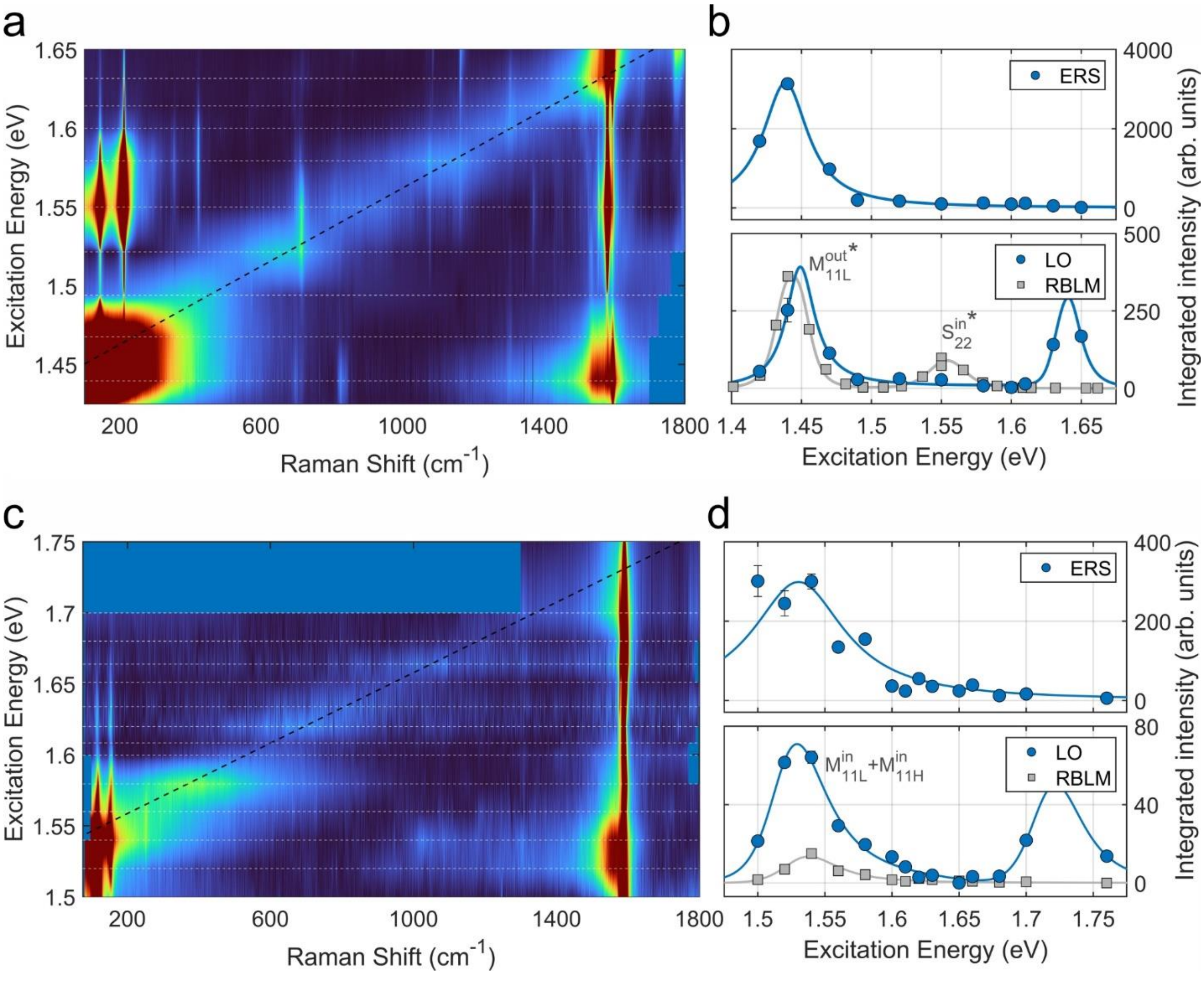

Figure 3. Tunable wavelength study of ERS in individual index-identified DWCNTs (14,1)@(15,12) and (18,6)@(21,14). (a) REM for (14,1)@(15,12) DWCNT. The dashed line

shows the Raman shift of the calculated position of the M_{ii} transition upon changing the excitation energy; the solid blue area around 1800 cm^{-1} represents the non-measured spectral regions. (b) Top panel: REP for the ERS peak integrated intensity; bottom panel: in-phase RBLM integrated intensity and LO *G*-mode integrated intensity for DWCNT (14,1)@(15,12) (experiment: solid dots; fit: solid lines). The asterisk shows two possible positions of M_{11H} transition (see SI Section S4). (c) REM for (18,6)@(21,14) DWCNT. (d) Top panel: REP for the ERS peak integrated intensity; bottom panel: in-phase RBLM and LO *G*-mode integrated intensities for DWCNT (18,6)@(21,14) (experiment: solid dots; fit: solid lines).

4. Discussion

4.1 Origin of ERS intensity suppression

We now discuss the possible origins of the ERS signal attenuation (or occasional complete suppression) in DWCNTs compared to SWCNTs. In the previous studies [17–19,25], the ERS intensity in SWCNTs was assumed to depend on both intrinsic and extrinsic factors. The latter comprises heating by the laser beam [18], electrostatic or electrochemical doping [17], and environmental effects (increased dielectric screening and charge transfer) when SWCNTs are located on substrates or in bundles [18]. In this work, we tried to reduce such extrinsic factors. For example, we minimized the heating of DWCNTs by employing low laser powers ($P < 0.4$ nW/nm^2), which should lead to negligible effects according to Ref. [18]. Doping from the substrate was excluded due to the suspended character of individual DWCNT samples. An effect of the water molecules adsorbed on the outer surface of DWCNTs [58,59] is hard to estimate but should be minor since we do not observe any notable difference between ERS behavior in the outer and inner layers (Figure 2e). Indeed, the inner layers are known to be chemically well shielded from the external environment and should behave differently in case of strong interactions with water vapor [60]. Moreover, the latter should also be present in reference SWCNTs since they were also studied in air [17–19]. As for the influence of defects in the DWCNT crystal structure on the ERS intensity quenching, it should be negligible since we observe almost no D-band (see Raman spectra in SI Section S3) and hence we have a minimal amount of defects in all our studied DWCNTs. Therefore, we argue that intrinsic effects contribute more significantly to the observed change of the ERS signal in DWCNTs.

The intrinsic aspects affecting the ERS intensity in SWCNTs include the chirality- and diameter-dependent exciton-exciton coupling, the curvature-induced bandgap opening and the resonance factor governed by the difference between laser energy E_L and the M_{ii} transition energy [25]. In multi-layer systems, like DWCNTs, other types of intrinsic effects can be present, namely, a reduced Coulomb (exciton-exciton) interaction resulting from an increase in the environmental dielectric screening [18] (Figure 4a), the interlayer energy or exciton transfer (IET) according to the Forster-Dexter mechanism [61] (Figure 4b) or interlayer charge transfer (ICT) predicted theoretically for commensurate DWCNTs due to the orbital mixing [62].

We first consider the SWCNT-specific effects. In principle, observing inconsistent I_{ERS}/I_{LO} ratios in Refs. [17–19] and this work may be explained by purely statistical reasons, *e.g.*, due to different probed structural types of CNTs. Hence, we analyzed the dependence of I_{ERS}/I_{LO} ratios on diameter d and chiral angle θ for all studied DWCNTs and SWCNTs in Figure S9. It turns out that the diameters of the SWCNTs from the literature overlap mostly with the diameters of the inner layers of our DWCNTs, but apart from this, the structural distributions of the probed SWCNTs and DWCNT layers are rather similar. The latter implies, for instance, that the curvature-induced bandgap opening (Section S11) should have the same effect for both SWCNTs and DWCNTs, and is therefore disregarded. Furthermore, the different I_{ERS}/I_{LO} ratios obtained from comparing the same chiralities in SWCNT and DWCNT forms (Table 1) suggest that the partial quenching of ERS is intrinsic for DWCNTs and unrelated to statistical effects.

As for the influence of interlayer coupling, we first considered the ICT by calculating its dependence on the interlayer distance Δr using the formula from Zólyomi *et al.* [62] (Section S12). It turns out that the calculated ICT for inner and outer layers is five times lower than the one required for the complete suppression of the ERS signal due to doping, according to Ref. [17]. Although it is still possible to interpret the partial suppression of the ERS features as a result of doping due to non-zero ICT, this effect should be most efficient in commensurate DWCNTs with strong coupling (so far studied only theoretically [62]) and less in the incommensurate DWCNTs from this work. Alternatively, the partial suppression of ERS intensity can be related to the Forster-Dexter IET predicted for both commensurate and incommensurate DWCNTs [61,63]. The fast IET process (lifetime τ ~ 70-220 fs [61,63]) can act as a non-radiative decay channel for photoexcited excitons competing with the fast exciton-exciton or electron-electron scattering processes (τ ~ 10 fs [64] for individual SWCNTs or ~200 fs for SWCNT ropes [65]) responsible for the ERS peak appearance (Figure 4b). The IET efficiency is known to depend on the distance between the interacting layers and the spectral overlap between the involved optical transitions [61], however, revealing these dependencies in the experimental distributions of I_{ERS}/I_{LO} values (Section S10) turned out impossible because the data points are significantly scattered due to the resonance effect (*i.e.*, dependence of I_{ERS}/I_{LO} value on the $|E_{laser} - M_{ii}|$). Therefore, further experimental and theoretical studies are necessary to estimate the exact contribution of IET to ERS intensity suppression. Another factor affecting the ERS intensity can be the reduction of Coulomb interaction between photoexcited excitons and low-energy excitons due to increased dielectric screening in DWCNTs compared to SWCNTs. Indeed, this screening was used to explain the ERS peak intensity suppression in SWCNTs deposited on substrates or for SWCNTs in bundles [18,19]. Since previous optical studies on suspended DWCNTs reported the existence of dielectric screening manifesting in a constant redshift of layer transition energies by about 50-60 meV [32,54], we suppose it should also have a significant influence on the ERS process in DWCNTs with metallic layers leading to the suppression of ERS intensity.

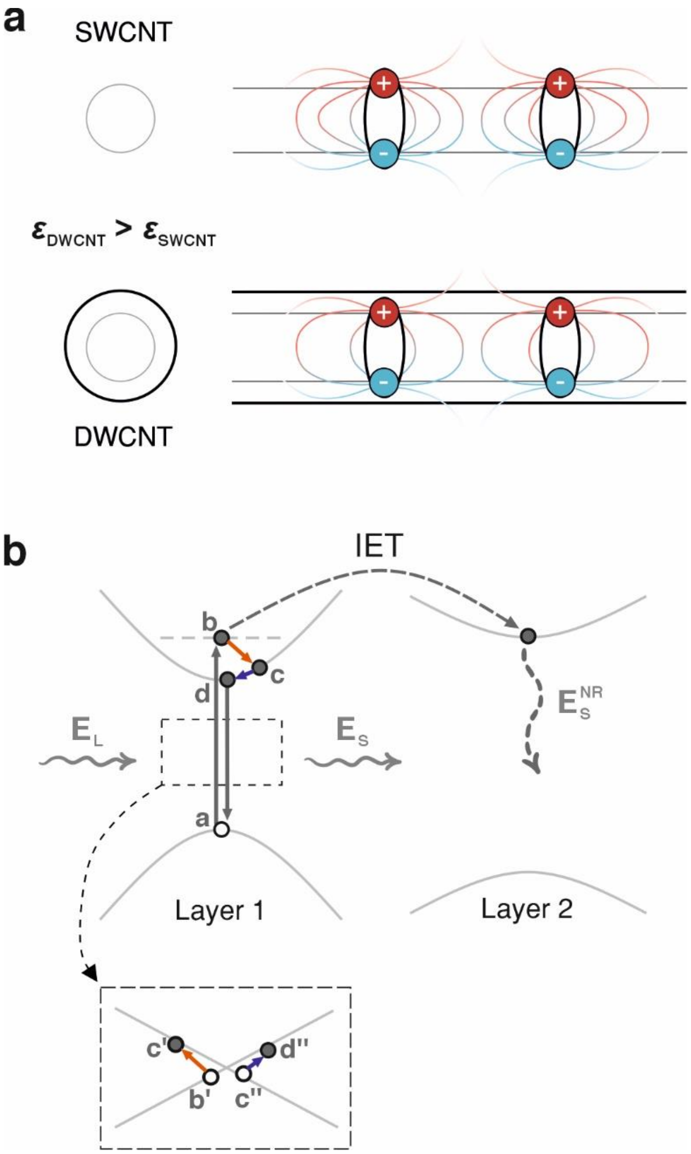

Figure 4. The ERS schematics and principal effects leading to the suppression of ERS intensity in DWCNTs. (a) The screening of Coulomb interactions between two excitons upon an increase of

dielectric screening in DWCNTs. The density of lines illustrates the different strengths of the electric field in a SWCNT and a DWCNT. (b) Schematics of the second-order ERS process with IET in a DWCNT: the incident photon with energy E_L creates an exciton by promoting the electron from state a to state b. The exciton is then scattered twice (b → c, c → d), creating through Coulomb interaction two low-energy excitons in the linear band of the metallic layer (inset: transitions $b' \rightarrow c'$ and $c'' \rightarrow d''$) and eventually recombines (d → a) by emitting a photon with energy E_S. Changing the excitation energy E_L involves different b and c states in the ERS process but keeps the final transition (d → a) and scattered photon energy the same. The IET is also shown (dashed line) acting as an additional non-radiative decay channel for photoexcited excitons which can compete with the intralayer exciton-exciton scattering responsible for ERS.

We also analyzed the Raman spectra of DWCNTs with semiconducting layers to investigate previously reported semiconducting-to-metal transitions [66,67] and the appearance of mini-Dirac points in DWCNTs [68]. Such changes in the electron band structure can, in principle, lead to the observation of ERS signals in the Raman spectra of semiconducting DWCNTs. In total, we probed 20 semiconducting layers (including six S@S DWCNTs), represented by blue hexagons in Figure 5. We did not find any ERS signals in such DWCNTs, which may be partly explained by the difficulty in finding DWCNT combinations with strong electronic coupling. Further systematic studies are necessary to observe such semiconducting-to-metal transitions in strongly coupled DWCNTs.

Interestingly, analyzing the dependence of the I_{ERS}/I_{LO} ratio on the structural parameters in DWCNTs can give additional insights into the SWCNT intrinsic properties. In particular, Hasdeo *et al.* [25] previously argued that the ERS signal should be absent in large diameter nanotubes (> 2 nm) due to the reduced Coulomb interaction and, hence, smaller exciton-exciton coupling strength. The CVD-grown DWCNTs act as perfect systems for exploring these effects since outer layers can reach 3 nm or more. In our study, there are nine outer SWCNTs (layers) with $d > 2$ nm (see Figure 2b,d), and we indeed observed almost complete quenching of ERS in the range above 2.3 nm.

4.2 Indexation of metallic DWCNTs based on the ERS features.

We now address the practical use of the ERS effect for indexing metallic layers of DWCNTs. Previously, Yang *et al.* [13,19] proposed a procedure for the structural characterization of individual SWCNTs that relied on measuring distinct M_{iiL} and M_{iiH} energies from ERS peaks and an RBM frequency in the Raman spectra. Due to the small dependence of the $|M_{iiH} - M_{iiL}|$ energy difference on the environmental interaction, the index-assignment of the SWCNT can be made with high accuracy by combining optical and vibrational information in the so-called bilayer plots.

In principle, the interlayer coupling between DWCNT layers can make some of the characterization methods established for SWCNTs highly challenging, as is the case of PL-based indexation. For instance, we previously estimated the PL from inner semiconducting layers of DWCNTs, including the (14,1)@(15,12) studied here, to be four orders of magnitude smaller than in isolated SWCNTs[37]. In comparison, the ERS signal from metallic layers of DWCNTs is much less quenched and therefore can still be used for structural identification of DWCNTs.

Based on our experimental findings and former theoretical predictions [25,26], we divide the available SWCNT chirality map into three zones (Figure 5). DWCNT layers with the highest expected ERS signal are located in Zone II with diameters up to ~2.3 nm. Zone I represents those CNTs where the curvature-induced bandgap can complicate the detection of ERS features above 100 cm^{-1} as described in Section S11. Zone III corresponds to the large-diameter layers, where the ERS intensity should be affected by the reduced exciton-exciton interaction. Of course, the partition of the chirality space into three zones is somewhat arbitrary, but it can nevertheless guide future research until more statistical data about the ERS effect are available.

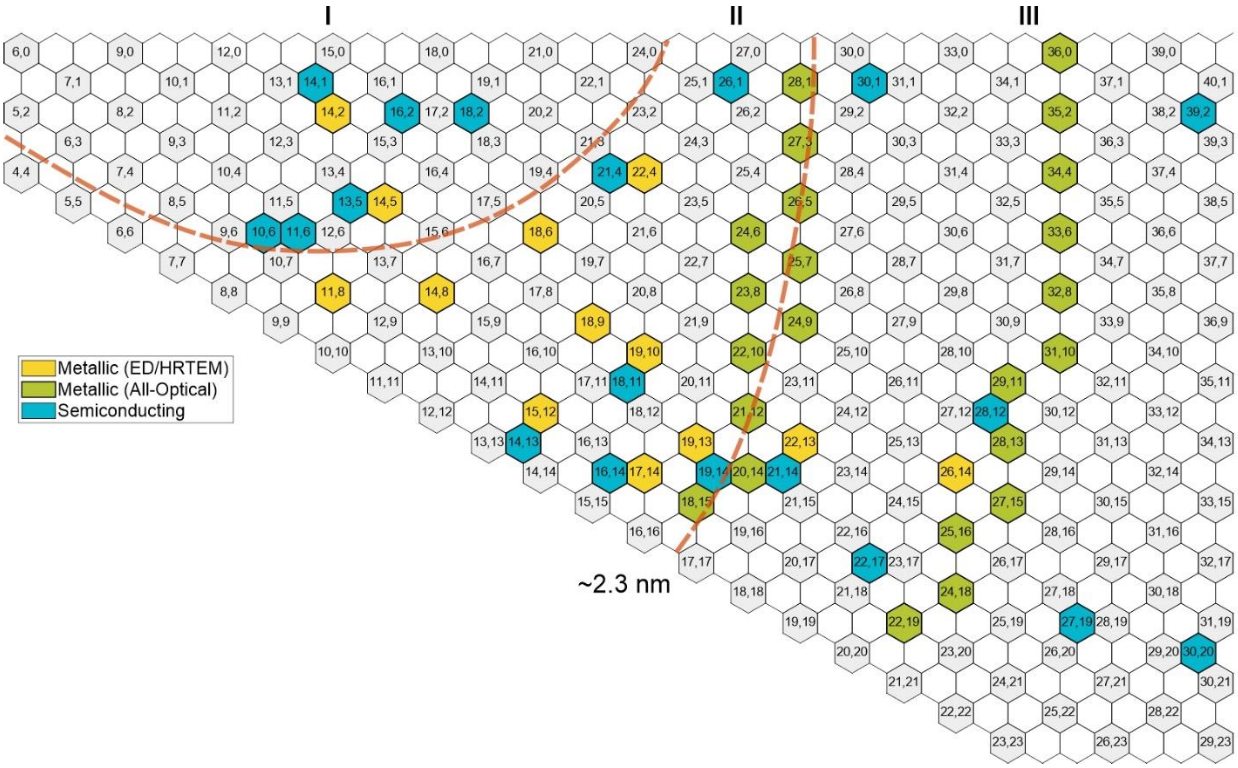

Figure 5. Experimental chirality distribution of studied DWCNT layers. Yellow and blue hexagons correspond to the metallic and semiconducting DWCNT layers, respectively, index-assigned by ED in this work. Green hexagons represent DWCNT layers characterized by the all-optical approach [14], hence several candidates are possible. Grey hexagons denote all geometrically possible metallic CNTs. Dashed lines tentatively partition the chirality map into three zones with the different expected intensity of ERS signal: Zone I – layers affected by curvature-induced bandgap; Zone II – layers with the expected maximum ERS intensity; Zone III – layers with suppressed ERS intensity due to reduced exciton-exciton interaction at large diameters.

In practice, it is first crucial to estimate the diameter of the involved DWCNTs from the RBLM frequencies. This can be done using the coupled-oscillator model from Refs. [10,16]. The knowledge of the layers' diameters points to the zones in Figure 5 and the expected strength of the

ERS signal. For instance, for large DWCNT layers, we can expect that even if the ERS signal is not quenched, it can be hard to measure due to reduced exciton-exciton interaction and IET. When the information of layer chirality is available, *e.g.*, from *G*-band lineshape analysis [10,69] or from additional methods (like ED or HRTEM), one can position the studied CNT more precisely within Zones I and II. Then, for layers from Zone I, the curvature-induced bandgap opening can influence the ERS, and the measurement should be performed with caution.

Based on the data from Figure 2c, we find that it is best to measure ERS peaks when they are located between the RBLM and *G*-band of the metallic layer. It corresponds to the DWCNT excitation with laser energy from a few meV to 200 meV above the M_{ii} transition. However, at large energy separation (*e.g.*, ERS peak near the *G*-band), it may be difficult to spot the small and broad ERS peaks among much stronger and narrow phonon lines due to the fast ERS intensity decay with energy separation (Figure 3b,d). In this case, it is necessary to zoom in on the spectrum 10-20 times to observe ERS unambiguously, as shown in Figure 2a (orange spectra). Repeating the ERS peak measurement at several laser excitation energies separated by 200 meV should allow the detection of most M_{ii} transitions of the probed metallic layer.

It is worth noting that the ERS can be useful for determining M_{ii} energies in case of strong overlap between the optical transitions of the layers, which is quite often the situation for DWCNTs. A good example is the DWCNT (14,8)@(19,14) (see DWCNT-4 in SI Section S3), where M_{11L} of the inner layer and S_{33} of the outer layer constitute a single broad peak centered at around 1.614 eV in the Rayleigh spectrum. Nevertheless, measuring the M_{11L} energy from the ERS line in Raman spectra allows identifying the exact position of the metallic transition at 1.590 eV.

4.3. Probing ERS in macroscopic samples of ultra-pure DWCNTs.

Recent progress in sorting DWCNTs by electronic type [41] and the development of macroscopic chirality-sorting procedures [70] call for fast structural characterization methods of the macroscopic ensemble samples sensitive to specific SWCNT and DWCNT chiralities. ERS may become in this regard a useful tool for characterizing metallic layers, however it has been so far studied and applied only on microscopic individual SWCNTs and DWCNTs. Here, we investigate its behavior in a mixed-chirality ultra-pure DWCNT (UP-DWCNT) sample for the first time. The as-grown DWCNT sample was carefully purified from SWCNT and MWCNT species by a two-step density gradient ultracentrifugation approach, as discussed in Ref. [44,73]. We then measured its RBLM REM in the region of the outer layers' M_{11} transitions by continuously varying the excitation energy between 1.45 and 1.85 eV. The map is shown in Figure 6a, where we observe a series of maxima, each corresponding to several non-resolved DWCNT configurations. Each such maximum can potentially lead to a separate ERS peak in the Raman spectra. However, in contrast to ERS from individual free-standing DWCNT layers, we expect these peaks to be broadened in the UP-DWCNT sample due to different local environments and multiple contributing DWCNT configurations.

In consequence, we first estimate the inhomogeneous broadening of the M_{ii} transitions in the macroscopic UP-DWCNT sample. For this purpose, we obtained the RBLM REPs by summing up the Raman spectrum intensities between 141-153.5, 153.5-163 and 163-177 cm^{-1} (see yellow, red and blue data points in Figure 6b labeled P3, P2 and P1, respectively). Fitting these RBLM REPs (solid curves in Figure 6b) allowed us to estimate the M_{11} linewidths, which are approximately equal to ERS linewidths in the Raman spectra according to the studies on individual free-standing DWCNTs.

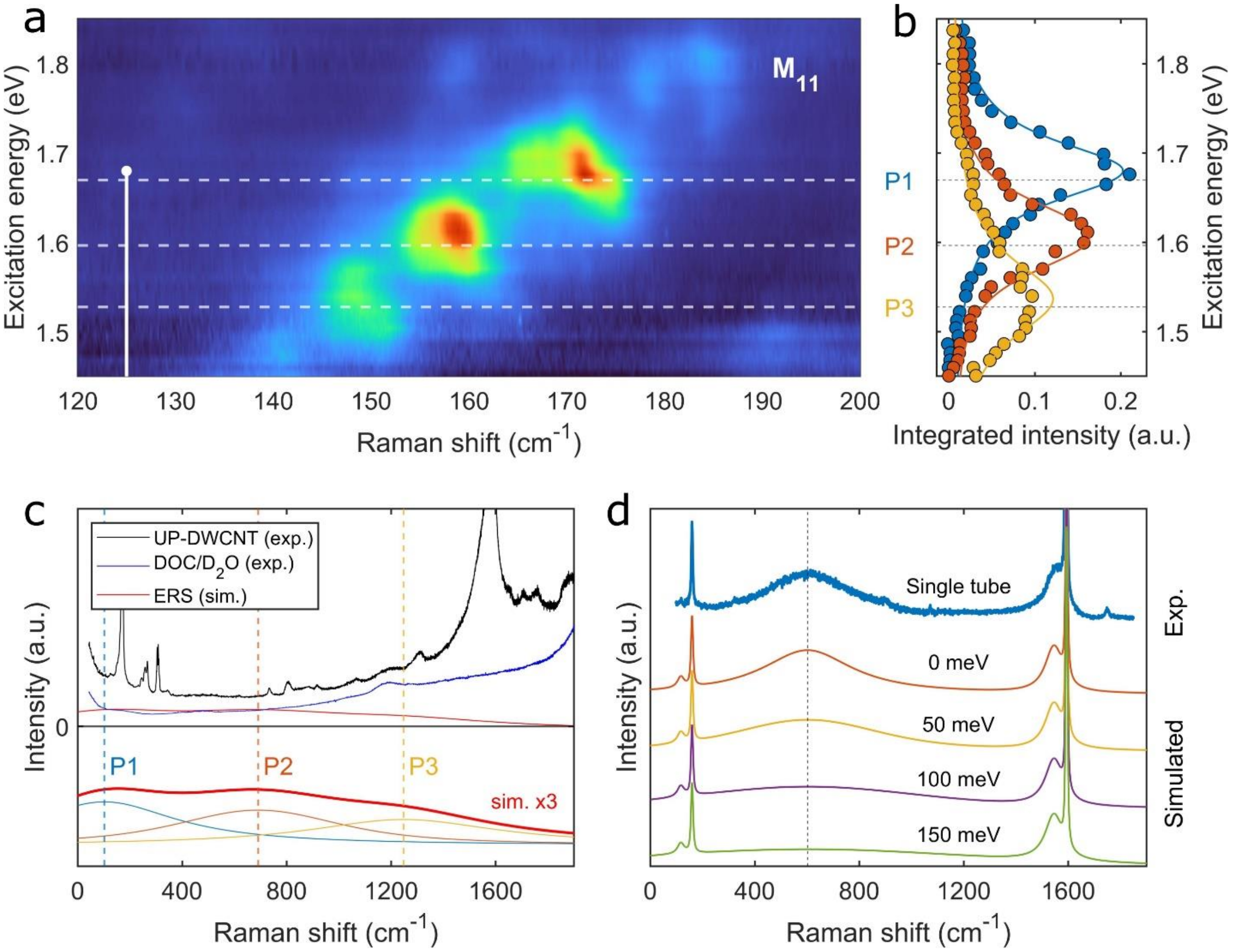

Figure 6. ERS process in macroscopic samples of mixed-chirality DWCNTs. (a) REM for in-phase RBLM of UP-DWCNTs in the range of *M₁₁* optical transitions. Different maxima correspond to different DWCNT outer layers present in the macroscopic solution. Dashed horizontal lines show the position of the *M₁₁* maxima determined from REP fits. The white solid vertical line between 1.45 and 1.68 eV denotes the range covered by the Raman spectrum in (c). (b) RBLM REPs for the three intense maxima present in (a). The yellow, red and blue data points are obtained by summing up Raman spectrum intensity between 141-153.5, 153.5-163 and 163-177 cm^{-1}, respectively. The solid lines correspond to the results of the REP fits with Voigt functions, while dashed lines and P1, P2 and P3 labels show fitted *M₁₁* transition energies. (c) Experimental Raman spectra of UP-DWCNTs (black) and DOC/D_2O (blue) excited at 1.68 eV (737 nm) with vertical dashed lines showing the expected positions of ERS peaks corresponding to *M₁₁* transitions identified in (b). The three colored Voigt curves below the experimental spectrum are the calculated ERS peaks with the inhomogeneous broadening obtained from REP

fits, while the red solid line is the sum of these curves. All simulated curves were multiplied by a factor of 3 for presentation purposes (d) Comparison of experimental Raman spectrum of the individual (14,8)@(19,14) DWCNT excited at 746 nm (top blue curve) and the calculated Raman spectra with ERS peaks having different inhomogeneous broadening due to interaction with the environment, namely 0, 50, 100 and 150 meV.

We then measured Raman spectra in the range from RBLM to *G*-band by exciting the UP-DWCNT sample at 737 nm (1.68 eV), as shown in Figure 6c (black curve). The spectrum is also compared with the reference solvent spectrum (blue curve) of a 2% solution of sodium deoxycholate (DOC) in D_2O measured in identical conditions. The UP-DWCNT spectrum contains the contributions from the RBLMs (100 – 400 cm^{-1}), intermediate frequency modes [71] (400 – 1100 cm^{-1}), *D*-band (~1300 cm^{-1}) and the intense signal from largely overlapping *G*-band, M-band [72] and *D′*-band above 1500 cm^{-1}. Using the colored dashed lines, we also show in Figure 6c the predicted positions of ERS peaks corresponding to three M_{11} transitions from Figures 6a,b. Interestingly, we do not observe any distinctive ERS features in the spectrum. This fact may be explained if we simulate the ERS peaks by using the linewidth and intensity values obtained from REP fits (see blue, red and yellow solid curves at the bottom of Figure 6c). Superimposing these ERS curves results in a featureless background (red solid line), which illustrates the effect of multi-chirality in macroscopic samples. We want to point out that the experimental DWCNT spectrum in Figure 6c is not proof of the ERS signal detection, but on the contrary, emphasizes the difficulty of the measurements on the mixed-chirality macroscopic DWCNT samples.

To get more insights into the ERS behavior in macro samples containing just one DWCNT chirality, we again modeled ERS lines using the example of individual free-standing DWCNT (14,8)@(19,14) (top solid blue line in Figure 6d). The effect of inhomogeneous broadening on the ERS was estimated using the Voigt functions with a varying Gaussian linewidth from 0 to 150 meV (see bottom four curves in Figure 6d). It becomes evident that above 50 meV, the ERS peak becomes too broad for practical detection. We, therefore, conclude that the successful observation of ERS features in macroscopic DWCNT samples should be possible only when they are sufficiently sorted, ideally to the single chirality level, or have well-separated electronic transitions and minimum possible inhomogeneous broadening (below ~ 50 meV). These conclusions should apply both for macroscopic mixed-chirality DWCNT solutions and DWCNT powders and thin films since the major difficulties in detecting ERS signals are common for both solid and liquid samples.

5. Conclusions

In this work, we report the observation of the ERS signal in individual index-identified DWCNTs having all types of electronic configurations with metallic layers. By comparing SWCNT and DWCNT data, we show that the increased dielectric screening in DWCNTs is most likely responsible for the suppression of the intensity of ERS peaks, in some cases leading to their complete disappearance from the Raman spectra.

Besides, we probe the ERS process in a macroscopic mixed-chirality ultra-pure DWCNT sample. It is found that the ERS lines are not distinguishable due to the large overlap between ERS peaks from different DWCNT chiralities present in the multi-chirality sample leading to a broad featureless background. We propose that observing ERS lines at the macroscale should be possible when the DWCNT samples can be sufficiently sorted, ideally to the single chirality level, or have well-separated electronic transitions and minimal inhomogeneous broadening.

Finally, we adapt a structural characterization procedure based on the ERS for DWCNTs with the dielectric screening and IET effects. The obtained results can be generalized to the structural description of other 1D VDW heterostructures based on metallic SWCNTs [30] if they have similar dielectric properties as DWCNT systems.

Declaration of competing interest

The authors declare that they have no conflicts of interest.

Acknowledgment

DL thanks Prof. S. Rochal and D. Chalin for providing MAPLE code for calculating DWCNT transition energy shifts and W. Van Werveke and M. De Clercq for providing MATLAB code for creating chirality distribution maps. A part of the experimental data (*i.e.*, microscopic Rayleigh and Raman spectra, ED patterns) was obtained and preliminary processed within the framework of Russian Foundation for Basic Research grant 18-32-00397 mol_a. Further data analysis (*i.e.*, developing models for ERS, Raman and Rayleigh spectra fitting) was performed by DL with the support of the postdoctoral grant (12ZP720N) of the Fund for Scientific Research Flanders (FWO). The TEM measurements were performed in the Laboratorio de Microscopias Avanzadas (LMA), Universidad de Zaragoza (Spain). R.A. gratefully acknowledges the support from the Spanish MICINN (PID2019-104739GB-100/AEI/10.13039/501100011033), Government of Aragon (projects DGA E13-20R (FEDER, EU)) and from the European Union H2020 program "ESTEEM3" (Grant number 823717). V.N.P. acknowledges financial support for NTB calculations from the National Science Fund of Bulgaria under grant KP-06-N38/10 from 06.12.2019. T.T.C acknowledges financial support from Vietnam Academy of Science and Technology (grant number: VAST03.06/22-23). H.N.T, E.F., A.A.Z, J.L.S. and M.P. acknowledge financial support by the ANR GAMBIT project, grant ANR-13-BS10-0014 of the French Agence Nationale de la Recherche.

The characterization of the macroscopic UP-DWCNT samples was financially supported by a PhD fellowship for M. Erkens of the Research Foundation of Flanders (FWO, grant number: 11C9220N). D.L. acknowledges the financial support from the University of Antwerp Research Fund (grant BOF KP 43770). D.L., M.A., W.W. and S.C. also acknowledge funding from FWO projects (G040011N, G02112N, G035918N and G036618N).

Supporting information

Supporting Information is available online at ….. and includes (1) Details of the DWCNT structure identification procedure, (2) Complete set of Rayleigh, RBLM and G-band spectra for investigated DWCNTs, (3) Complete set of wide-range Raman and ERS data for investigated DWCNTs, (4) Complete set of tunable Raman spectra and results of absorption spectrum calculations for DWCNTs (14,1)@(15,12) and (18,6)@(21,14), (5), Details on the Rayleigh data processing and fitting procedures, (6) Details on the ERS data processing and fitting procedures, (7) Table with results of the ERS fitting for DWCNTs, (8) Table with results of the ERS data digitization for SWCNTs, (9) Comparison of I_{ERS}/I_{LO} ratios in individual free-standing SWCNTs and DWCNTs, (10) Dependence of I_{ERS}/I_{LO} ratio on structural parameters of DWCNT layers, (11) Effect of curvature-induced bandgap on ERS lines, (12) Estimation of the interlayer charge transfer between the layers of DWCNTs.

References

[1] S. Reich, C. Thomsen, J. Maultzsch, Carbon Nanotubes: Basic Concepts and Physical Properties, 1st ed., WILEY-VCH Verlag GmbH & Co. KGaA, 2004. https://www.wiley.com/en-be/Carbon+Nanotubes:+Basic+Concepts+and+Physical+Properties-p-9783527403868 (accessed September 6, 2018).

[2] R. Rao, C.L. Pint, A.E. Islam, R.S. Weatherup, S. Hofmann, E.R. Meshot, F. Wu, C. Zhou, N. Dee, P.B. Amama, J. Carpena-Nuñez, W. Shi, D.L. Plata, E.S. Penev, B.I. Yakobson, P.B. Balbuena, C. Bichara, D.N. Futaba, S. Noda, H. Shin, K.S. Kim, B. Simard, F. Mirri, M. Pasquali, F. Fornasiero, E.I. Kauppinen, M. Arnold, B.A. Cola, P. Nikolaev, S. Arepalli, H.-M. Cheng, D.N. Zakharov, E.A. Stach, J. Zhang, F. Wei, M. Terrones, D.B. Geohegan, B. Maruyama, S. Maruyama, Y. Li, W.W. Adams, A.J. Hart, Carbon Nanotubes and Related Nanomaterials: Critical Advances and Challenges for Synthesis toward Mainstream Commercial Applications, ACS Nano. 12 (2018) 11756–11784. doi:10.1021/acsnano.8b06511.

[3] P. Avouris, Z. Chen, V. Perebeinos, Carbon-based electronics., Nat. Nanotechnol. 2 (2007) 605–15. doi:10.1038/nnano.2007.300.

[4] D. Nakar, G. Gordeev, L.D. MacHado, R. Popovitz-Biro, K. Rechav, E.F. Oliveira, P. Kusch, A. Jorio, D.S. Galvaõ, S. Reich, E. Joselevich, Few-Wall Carbon Nanotube Coils, Nano Lett. 20 (2020) 953–962. doi:10.1021/acs.nanolett.9b03977.

[5] C.S. Allen, C. Zhang, G. Burnell, A.P. Brown, J. Robertson, B.J. Hickey, A review of methods for the accurate determination of the chiral indices of carbon nanotubes from electron diffraction patterns, Carbon. 49 (2011) 4961–4971. doi:10.1016/j.carbon.2011.06.100.

[6] J.H. Warner, N.P. Young, A.I. Kirkland, G.A.D. Briggs, Resolving strain in carbon nanotubes at the atomic level, Nat. Mater. 10 (2011) 958–962. doi:10.1038/nmat3125.

[7] T.W. Odom, J.L. Huang, P. Kim, C.M. Lieber, Atomic structure and electronic properties of single-walled carbon nanotubes, Nature. 391 (1998) 62–64. doi:10.1038/34139.

[8] J. Lefebvre, P. Finnie, J. Fagan, M. Zheng, A.R. Hight Walker, Metrological Assessment of Single-Wall Carbon Nanotube Materials by Optical Methods, in: World Sci. Ser. Carbon Nanosci., World Scientific Publishing Co. Pte Ltd, 2019: pp. 45–104. doi:10.1142/9789813235465_0002.

[9] A. Castan, S. Forel, F. Fossard, J. Defillet, A. Ghedjatti, D. Levshov, W. Wenseleers, S. Cambré, A. Loiseau, Assessing the reliability of the Raman peak counting method for the

characterization of SWCNT diameter distributions: a cross characterization with TEM, Carbon. 171 (2021) 968–979. doi:10.1016/j.carbon.2020.09.012.

[10] D.I. Levshov, H.N. Tran, M. Paillet, R. Arenal, X.T. Than, A.A. Zahab, Y.I. Yuzyuk, J.-L. Sauvajol, T. Michel, Accurate determination of the chiral indices of individual carbon nanotubes by combining electron diffraction and Resonant Raman spectroscopy, Carbon. 114 (2017) 141–159. doi:10.1016/j.carbon.2016.11.076.

[11] S.M. Bachilo, M.S. Strano, C. Kittrell, R.H. Hauge, R.E. Smalley, R.B. Weisman, Structure-assigned optical spectra of single-walled carbon nanotubes., Science. 298 (2002) 2361–2366. doi:10.1126/science.1078727.

[12] M. Pfohl, D.D. Tune, A. Graf, J. Zaumseil, R. Krupke, B.S. Flavel, Fitting Single-Walled Carbon Nanotube Optical Spectra, ACS Omega. 2 (2017) 1163–1171. doi:10.1021/acsomega.6b00468.

[13] J. Yang, D. Zhang, Y. Hu, C. Xia, S. Sun, Y. Li, Bilayer Plots for Accurately Determining the Chirality of Single-Walled Carbon Nanotubes Under Complex Environments, ACS Nano. 11 (2017) acsnano.7b05860. doi:10.1021/acsnano.7b05860.

[14] S. Berciaud, V. V. Deshpande, R. Caldwell, Y. Miyauchi, C. Voisin, P. Kim, J. Hone, T.F. Heinz, All-optical structure assignment of individual single-walled carbon nanotubes from Rayleigh and Raman scattering measurements, Phys. Status Solidi. 249 (2012) 2436–2441. doi:10.1002/pssb.201200152.

[15] A. Jorio, R. Saito, Raman spectroscopy for carbon nanotube applications, J. Appl. Phys. 129 (2021). doi:10.1063/5.0030809.

[16] T. Michel, D. Levshov, A.-A. Zahab, J.-L. Sauvajol, M. Paillet, Probing the Intrinsic Vibrational and Optical Properties of Individual Chirality-Identified Carbon Nanotubes by Raman Spectroscopy, in: R.B. Weisman, J. Kono (Eds.), Handb. Carbon Nanomater. Vol. 10 Opt. Prop. Carbon Nanotub., World Scientific Publishing, Singapore, 2019: pp. 75–112. doi:10.1142/9789813235465_0010.

[17] H. Farhat, S. Berciaud, M. Kalbac, R. Saito, T.F. Heinz, M.S. Dresselhaus, J. Kong,

Observation of Electronic Raman Scattering in Metallic Carbon Nanotubes, Phys. Rev. Lett. 107 (2011) 157401. doi:10.1103/PhysRevLett.107.157401.

[18] D. Zhang, J. Yang, E.H. Hasdeo, C. Liu, K. Liu, R. Saito, Y. Li, Multiple electronic Raman scatterings in a single metallic carbon nanotube, Phys. Rev. B. 93 (2016) 245428. doi:10.1103/PhysRevB.93.245428.

[19] D. Zhang, J. Yang, M. Li, Y. Li, (n , m) Assignments of Metallic Single-Walled Carbon Nanotubes by Raman Spectroscopy: The Importance of Electronic Raman Scattering, ACS Nano. 10 (2016) 10789–10797. doi:10.1021/acsnano.6b04453.

[20] Y. Hu, S. Chen, X. Cong, S. Sun, J. Wu, D. Zhang, F. Yang, J. Yang, P.-H. Tan, Y. Li, Electronic Raman Scattering in Suspended Semiconducting Carbon Nanotubes, J. Phys. Chem. Lett. (2020) 1–12. doi:10.1021/acs.jpclett.0c03320.

[21] E. Burstein, D.L. Mills, R.F. Wallis, Interband electronic raman scattering in semimetals and semiconductors, Phys. Rev. B. 4 (1971) 2429–2436. doi:10.1103/PhysRevB.4.2429.

[22] B. Fluegel, A. V. Mialitsin, D.A. Beaton, J.L. Reno, A. Mascarenhas, Electronic Raman scattering as an ultra-sensitive probe of strain effects in semiconductors, Nat. Commun. 6 (2015) 7136. doi:10.1038/ncomms8136.

[23] L. Alonso Vazquez-Zuniga, S. Chung, Y. Jeong -, A. Takeuchi, Y. Suzuki, K. Uesugi, al - , C. Microbalance Asuman Unal, A. Robert Hillman, K.S. Ryder, New insights into the phase diagram of the copper oxide superconductors from electronic Raman scattering, Reports Prog. Phys. 76 (2013) 022502. doi:10.1088/0034-4885/76/2/022502.

[24] G.R. Boyd, T.P. Devereaux, P.J. Hirschfeld, V. Mishra, D.J. Scalapino, Probing the pairing symmetry of the iron pnictides with electronic Raman scattering, Phys. Rev. B. 79 (2009) 174521. doi:10.1103/PhysRevB.79.174521.

[25] E.H. Hasdeo, A.R.T. Nugraha, K. Sato, M.S. Dresselhaus, R. Saito, Electronic Raman scattering and the Fano resonance in metallic carbon nanotubes, Phys. Rev. B. 88 (2013) 115107. doi:10.1103/PhysRevB.88.115107.

[26] R. Saito, A.R.T. Nugraha, E.H. Hasdeo, N.T. Hung, W. Izumida, Electronic and Optical

Properties of Single Wall Carbon Nanotubes, Top. Curr. Chem. 375 (2017) 7. doi:10.1007/s41061-016-0095-2.

[27] X. Chen, B. Zhu, A. Zhang, H. Zeng, Q. Zhang, X. Cui, Electronic Raman scattering on individual semiconducting single walled carbon nanotubes., Sci. Rep. 4 (2014) 5969. doi:10.1038/srep05969.

[28] R. Xiang, S. Maruyama, Heteronanotubes: Challenges and Opportunities, Small Sci. 1 (2021) 2000039. doi:https://doi.org/10.1002/smsc.202000039.

[29] R. Xiang, T. Inoue, Y. Zheng, A. Kumamoto, Y. Qian, Y. Sato, M. Liu, D. Tang, D. Gokhale, J. Guo, K. Hisama, S. Yotsumoto, T. Ogamoto, H. Arai, Y. Kobayashi, H. Zhang, B. Hou, A. Anisimov, M. Maruyama, Y. Miyata, S. Okada, S. Chiashi, Y. Li, J. Kong, E.I. Kauppinen, Y. Ikuhara, K. Suenaga, S. Maruyama, One-dimensional van der Waals heterostructures, Science. 367 (2020) 537–542. doi:10.1126/science.aaz2570.

[30] S. Cambré, M. Liu, D. Levshov, K. Otsuka, S. Maruyama, R. Xiang, Nanotube-Based 1D Heterostructures Coupled by van der Waals Forces, Small. 2102585 (2021) 1–26. doi:10.1002/smll.202102585.

[31] S. Zhao, R. Kitaura, P. Moon, M. Koshino, F. Wang, Interlayer Interactions in 1D Van der Waals Moiré Superlattices, Adv. Sci. 2103460 (2021) 2103460. doi:10.1002/advs.202103460.

[32] K. Liu, C. Jin, X. Hong, J. Kim, A. Zettl, E. Wang, F. Wang, Van der Waals-coupled electronic states in incommensurate double-walled carbon nanotubes, Nat. Phys. 10 (2014) 737–742. doi:10.1038/nphys3042.

[33] S. Zhao, P. Moon, Y. Miyauchi, T. Nishihara, K. Matsuda, M. Koshino, R. Kitaura, Observation of Drastic Electronic-Structure Change in a One-Dimensional Moiré Superlattice, Phys. Rev. Lett. 124 (2020) 106101. doi:10.1103/physrevlett.124.106101.

[34] V.N. Popov, Theoretical evidence of a significant modification of the electronic structure of double-walled carbon nanotubes due to the interlayer interaction, Carbon. 170 (2020) 30–36. doi:10.1016/j.carbon.2020.07.036.

[35] D. V. Chalin, S.B. Rochal, Band structure and inter-tube optical transitions in double-walled carbon nanotubes, Phys. Rev. B. 102 (2020) 115426. doi:10.1103/PhysRevB.102.115426.

[36] M. Paillet, V.N. Popov, H.N. Tran, J.-C. Blancon, D.I. Levshov, R. Arenal, R. Parret, A. Ayari, A. San Miguel, F. Vallée, N. Del Fatti, A.A. Zahab, J.-L. Sauvajol, Optically active cross-band transition in double-walled carbon nanotube and its impact on Raman resonances, Carbon. 196 (2022) 950–960. doi:10.1016/j.carbon.2022.05.044.

[37] D.I. Levshov, R. Parret, H.-N. Tran, T. Michel, T.T. Cao, V.C. Nguyen, R. Arenal, V.N. Popov, S.B. Rochal, J.-L. Sauvajol, A.-A. Zahab, M. Paillet, Photoluminescence from an individual double-walled carbon nanotube, Phys. Rev. B. 96 (2017) 195410. doi:10.1103/PhysRevB.96.195410.

[38] K. Liu, X. Hong, M. Wu, F. Xiao, W. Wang, X. Bai, J.W. Ager, S. Aloni, A. Zettl, E. Wang, F. Wang, Quantum-coupled radial-breathing oscillations in double-walled carbon nanotubes, Nat. Commun. 4 (2013) 1375. doi:10.1038/ncomms2367.

[39] D.I. Levshov, H.N. Tran, T. Michel, T.T. Cao, V.C. Nguyen, R. Arenal, V.N. Popov, J.-L. Sauvajol, A.-A. Zahab, M. Paillet, Interlayer Interaction Effects on the G Modes in Double-Walled Carbon Nanotubes With Different Electronic Configurations, Phys. Status Solidi. 254 (2017) 1700251. doi:10.1002/pssb.201700251.

[40] V.N. Popov, D.I. Levshov, J.-L. Sauvajol, M. Paillet, Computational study of the shift of the G band of double-walled carbon nanotubes due to interlayer interactions, Phys. Rev. B. 97 (2018) 165417. doi:10.1103/PhysRevB.97.165417.

[41] H. Li, G. Gordeev, S. Wasserroth, V.S.K. Chakravadhanula, S.K.C. Neelakandhan, F. Hennrich, A. Jorio, S. Reich, R. Krupke, B.S. Flavel, Inner- and outer-wall sorting of double-walled carbon nanotubes, Nat. Nanotechnol. 12 (2017) 1176–1182. doi:10.1038/nnano.2017.207.

[42] T.X. Tinh, N. Van Chuc, V. Jourdain, M. Paillet, D.-Y. Kim, J.-L. Sauvajol, N.T.T. Tam, P.N. Minh, Synthesis of individual ultra-long carbon nanotubes and transfer to other substrates, J. Exp. Nanosci. 6 (2011) 547–556. doi:10.1080/17458080.2010.498839.

[43] E. Flahaut, R. Bacsa, A. Peigney, C. Laurent, Gram-scale CCVD synthesis of double-walled carbon nanotubes, Chem. Commun. 3 (2003) 1442–1443. doi:10.1039/B301514A.

[44] M. Erkens, S. Cambré, E. Flahaut, F. Fossard, A. Loiseau, W. Wenseleers, Ultrasonication-induced extraction of inner shells from double-wall carbon nanotubes characterized via in situ spectroscopy after density gradient ultracentrifugation, Carbon. 185 (2021) 113–125. doi:10.1016/j.carbon.2021.07.075.

[45] H. Kuzmany, W. Plank, R. Pfeiffer, F. Simon, Raman scattering from double-walled carbon nanotubes, J. Raman Spectrosc. 39 (2008) 134–140. doi:10.1002/jrs.1824.

[46] A.A. Green, M.C. Hersam, Properties and application of double-walled carbon nanotubes sorted by outer-wall electronic type, ACS Nano. 5 (2011) 1459–1467. doi:10.1021/nn103263b.

[47] F. Villalpando-Paez, H. Son, D. Nezich, Y.P. Hsieh, J. Kong, Y. a Kim, D. Shimamoto, H. Muramatsu, T. Hayashi, M. Endo, M. Terrones, M.S. Dresselhaus, Raman spectroscopy study of isolated double-walled carbon nanotubes with different metallic and semiconducting configurations., Nano Lett. 8 (2008) 3879–86. doi:10.1021/nl802306t.

[48] S. Rochal, D. Levshov, M. Avramenko, R. Arenal, T.T. Cao, V.C. Nguyen, J.-L. Sauvajol, M. Paillet, Chirality manifestation in elastic coupling between the layers of double-walled carbon nanotubes, Nanoscale. 11 (2019) 16092–16102. doi:10.1039/C9NR03853A.

[49] D.A. Tsyboulski, Y. Hou, N. Fakhri, S. Ghosh, R. Zhang, S.M. Bachilo, M. Pasquali, L. Chen, J. Liu, R.B. Weisman, Do inner shells of double-walled carbon nanotubes fluoresce?, Nano Lett. 9 (2009) 3282–3289. doi:10.1021/nl901550r.

[50] A.A. Green, M.C. Hersam, Processing and properties of highly enriched double-wall carbon nanotubes, Nat. Nanotechnol. 4 (2009) 64–70. doi:10.1038/nnano.2008.364.

[51] K.T. Nguyen, A. Gaur, M. Shim, Fano Lineshape and Phonon Softening in Single Isolated Metallic Carbon Nanotubes, Phys. Rev. Lett. 98 (2007) 145504. doi:10.1103/PhysRevLett.98.145504.

[52] T. Hertel, R.E. Walkup, P. Avouris, Deformation of carbon nanotubes by surface van der

Waals forces, Phys. Rev. B. 58 (1998) 13870–13873. doi:10.1103/PhysRevB.58.13870.

[53] K. Liu, J. Deslippe, F. Xiao, R.B. Capaz, X. Hong, S. Aloni, A. Zettl, W. Wang, X. Bai, S.G. Louie, E. Wang, F. Wang, An atlas of carbon nanotube optical transitions, Nat. Nanotechnol. 7 (2012) 325–329. doi:10.1038/nnano.2012.52.

[54] S. Zhao, T. Kitagawa, Y. Miyauchi, K. Matsuda, H. Shinohara, R. Kitaura, Rayleigh scattering studies on inter-layer interactions in structure-defined individual double-wall carbon nanotubes, Nano Res. 7 (2014) 1548–1555. doi:10.1007/s12274-014-0515-y.

[55] T. Michel, M. Paillet, a Zahab, D. Nakabayashi, V. Jourdain, R. Parret, J.-L. Sauvajol, About the indexing of the structure of single-walled carbon nanotubes from resonant Raman scattering, Adv. Nat. Sci. Nanosci. Nanotechnol. 1 (2011) 045007. doi:10.1088/2043-6262/1/4/045007.

[56] J.G. Duque, H. Telg, H. Chen, A.K. Swan, A.P. Shreve, X. Tu, M. Zheng, S.K. Doorn, Quantum Interference between the Third and Fourth Exciton States in Semiconducting Carbon Nanotubes Using Resonance Raman Spectroscopy, Phys. Rev. Lett. 108 (2012) 117404. doi:10.1103/PhysRevLett.108.117404.

[57] H.N. Tran, J.-C. Blancon, R. Arenal, R. Parret, A.A. Zahab, A. Ayari, F. Vallée, N. Del Fatti, J.-L. Sauvajol, M. Paillet, Quantum interference effects on the intensity of the G modes in double-walled carbon nanotubes, Phys. Rev. B. 95 (2017) 205411. doi:10.1103/PhysRevB.95.205411.

[58] S. Chiashi, K. Kono, D. Matsumoto, J. Shitaba, N. Homma, A. Beniya, T. Yamamoto, Y. Homma, Adsorption effects on radial breathing mode of single-walled carbon nanotubes, Phys. Rev. B - Condens. Matter Mater. Phys. 91 (2015) 1–5. doi:10.1103/PhysRevB.91.155415.

[59] Y. Homma, S. Chiashi, T. Yamamoto, K. Kono, D. Matsumoto, J. Shitaba, S. Sato, Photoluminescence measurements and molecular dynamics simulations of water adsorption on the hydrophobic surface of a carbon nanotube in water vapor, Phys. Rev. Lett. 110 (2013) 1–4. doi:10.1103/PhysRevLett.110.157402.

[60] K.E. Moore, D.D. Tune, B.S. Flavel, Double-Walled Carbon Nanotube Processing, Adv. Mater. 27 (2015) 3105–3137. doi:10.1002/adma.201405686.

[61] T. Koyama, Y. Asada, N. Hikosaka, Y. Miyata, H. Shinohara, A. Nakamura, Ultrafast Exciton Energy Transfer between Nanoscale Coaxial Cylinders: Intertube Transfer and Luminescence Quenching in Double-Walled Carbon Nanotubes, ACS Nano. 5 (2011) 5881–5887. doi:10.1021/nn201661q.

[62] V. Zólyomi, J. Koltai, Á. Rusznyák, J. Kürti, Á. Gali, F. Simon, H. Kuzmany, Á. Szabados, P. Surján, Intershell interaction in double walled carbon nanotubes: Charge transfer and orbital mixing, Phys. Rev. B. 77 (2008) 245403. doi:10.1103/PhysRevB.77.245403.

[63] O. Postupna, R. Long, O. V. Prezhdo, Time-Domain Ab Initio Simulation of Energy Transfer in Double-Walled Carbon Nanotubes, J. Phys. Chem. C. 119 (2015) 12088–12094. doi:10.1021/acs.jpcc.5b03629.

[64] K. Liu, X. Hong, Q. Zhou, C. Jin, J. Li, W. Zhou, J. Liu, E. Wang, A. Zettl, F. Wang, High-throughput optical imaging and spectroscopy of individual carbon nanotubes in devices, Nat. Nanotechnol. 8 (2013) 917–922. doi:10.1038/nnano.2013.227.

[65] A. Hagen, G. Moos, V. Talalaev, T. Hertel, Electronic structure and dynamics of optically excited single-wall carbon nanotubes, Appl. Phys. A Mater. Sci. Process. 78 (2004) 1137–1145. doi:10.1007/s00339-003-2465-1.

[66] V. Zolyomi, A. Rusznyak, J. Kurti, A. Gali, F. Simon, H. Kuzmany, A. Szabados, P.R. Surjan, Semiconductor-to-metal transition of double walled carbon nanotubes induced by inter-shell interaction, Phys. Status Solidi Basic Res. 243 (2006) 3476–3479. doi:10.1002/pssb.200669161.

[67] S. Okada, A. Oshiyama, Curvature-Induced Metallization of Double-Walled Semiconducting Zigzag Carbon Nanotubes, Phys. Rev. Lett. 91 (2003) 216801. doi:10.1103/PhysRevLett.91.216801.

[68] R. Bonnet, A. Lherbier, C. Barraud, M.L. Della Rocca, P. Lafarge, J. Charlier, Charge transport through one-dimensional Moiré crystals, Sci. Rep. 6 (2016) 19701.

doi:10.1038/srep19701.

[69] Y. Wu, J. Maultzsch, E. Knoesel, B. Chandra, M. Huang, M.Y. Sfeir, L.E. Brus, J. Hone, T.F. Heinz, Variable Electron-Phonon Coupling in Isolated Metallic Carbon Nanotubes Observed by Raman Scattering, Phys. Rev. Lett. 99 (2007) 027402. doi:10.1103/PhysRevLett.99.027402.

[70] F. Yang, M. Wang, D. Zhang, J. Yang, M. Zheng, Y. Li, Chirality Pure Carbon Nanotubes: Growth, Sorting, and Characterization, Chem. Rev. 120 (2020) 2693–2758. doi:10.1021/acs.chemrev.9b00835.

[71] T. Inaba, Y. Tanaka, S. Konabe, Y. Homma, Effects of Chirality and Defect Density on the Intermediate Frequency Raman Modes of Individually Suspended Single-Walled Carbon Nanotubes, J. Phys. Chem. C. 122 (2018) 9184–9190. doi:10.1021/acs.jpcc.8b01017.

[72] A. Vierck, F. Gannott, M. Schweiger, J. Zaumseil, J. Maultzsch, ZA-derived phonons in the Raman spectra of single-walled carbon nanotubes, Carbon. 117 (2017) 360–366. doi:10.1016/j.carbon.2017.02.101.

[73] M. Erkens, D. Levshov, W. Wenseleers, H. Li, B. Flavel, J. Fagan, V. Popov, M. Avramenko, S. Forel, E. Flahaut, S. Cambre, Efficient Inner-to-Outer Wall Energy Transfer in Highly Pure Double-Wall Carbon Nanotubes Revealed by Detailed Spectroscopy, ACS Nano 16 (10) (2022) 16038–16053.

SUPPORTING INFORMATION FOR:

Partial quenching of electronic Raman scattering in double-wall carbon nanotubes by interlayer coupling

Dmitry I. Levshov[1,2,3,*], *Marina V. Avramenko*[1,3], *Maksiem Erkens*[1], *Huy-Nam Tran*[2], *Thi Thanh Cao*[4], *Van Chuc Nguyen*[4], *Emmanuel Flahaut*[5], *Valentin N. Popov*[6], *Ahmed-Azmi Zahab*[2], *Jean-Louis Sauvajol*[2], *Raul Arenal*[7,8,9], *Wim Wenseleers*[1], *Sofie Cambré*[1], *Matthieu Paillet*[2]

[1]Nanostructured and Organic Optical and Electronic Materials, Department of Physics, University of Antwerp, B-2610 Antwerp, Belgium

[2]Laboratoire Charles Coulomb, Université de Montpellier, CNRS, F-34095, Montpellier, France

[3]Department of Nanotechnology, Faculty of Physics, Southern Federal University, 5, Zorge Street, Rostov-on-Don, 344090, Russia

[4]Institute of Materials Science, Vietnam Academy of Science and Technology, 18 Hoang Quoc Viet, Hanoi, Vietnam

[5]CIRIMAT, CNRS-INP-UPS, Université Toulouse 3 Paul Sabatier, 118 route de Narbonne, F-31062 Toulouse cedex 9, France

[6]Faculty of Physics, University of Sofia, BG-1164, Sofia, Bulgaria

[7]Instituto de Nanociencia y Materiales de Aragon (INMA), CSIC-U. de Zaragoza, 50009 Zaragoza, Spain

[8]Laboratorio de Microscopias Avanzadas (LMA), Universidad de Zaragoza, 50018 Zaragoza, Spain

[9]ARAID Foundation, 50018 Zaragoza, Spain

* Corresponding author: Tel: +32 3 265 24 79; Email: dmitry.levshov@uantwerpen.be

Table of Contents

Section S1. Details of the DWCNT structure identification procedure

We characterized the structure of individual free-standing DWCNTs following either the electron diffraction (ED) based method from Ref. [1] or by combining Rayleigh and Raman spectroscopic information [2]. Tables S1.1 and S1.2 summarize the *(n,m)* indices of the studied DWCNTs and the indexation method used. The first column introduces the notation, *e.g.,* DWCNT-1, that will be used throughout this SI for referring to specific DWCNTs. The ED patterns of the studied DWCNTs were previously provided in the Supplementary Materials of Ref. [3].

Table S1.1. List of the studied DWCNTs with metallic layers.

#	**(n_{in},m_{in})@(n_{out},m_{out})**	**Indexation Method**	**Electronic Configuration**	**Source**
DWCNT-1	(14,1)@(15,12)	ED	SC@M	Ref. [3]
DWCNT-2	(14,2)@(22,4)	ED	M@M	Ref. [3]
DWCNT-3	(11,8)@(19,10)	Rayleigh+Raman	M@M	Ref. [4]
DWCNT-4	(14,8)@(19,14)	ED	M@SC	Ref. [3]
DWCNT-5	(14,5)@(26,1)	ED	M@SC	Ref. [3]
DWCNT-6	(18,2)@(19,13)	ED	SC@M	Ref. [3]
DWCNT-7	(18,6)@(21,14)	ED	M@SC	Ref. [3]
DWCNT-8	(22,13)@(39,2)	ED	M@SC	Ref. [3]
DWCNT-9	(17,14)@(26,14)	ED	M@M	Ref. [3]
DWCNT-10	(17,14)@(28,12)	ED	M@SC	Ref. [3]
DWCNT-11	multiple candidates	Rayleigh+Raman	SC@M	this work
DWCNT-12	multiple candidates	Rayleigh+Raman	M@SC	this work
DWCNT-13	multiple candidates	Rayleigh+Raman	SC@M	this work
DWCNT-14	multiple candidates	Rayleigh+Raman	SC@M	this work
DWCNT-15	(11,6)@(18,9)	ED	SC@M	Ref. [3]

Table S1.2. List of the studied DWCNTs with purely semiconducting layers.

#	**(n_{in},m_{in})@(n_{out},m_{out})**	**Indexation Method**	**Electronic Configuration**	**Source**
DWCNT-16	(10,6)@(14,13)	Rayleigh+Raman	SC@SC	Ref. [5]
DWCNT-17	(16,2)@(16,14)	ED	SC@SC	Ref. [3]
DWCNT-18	(14,1)@(21,4)	Rayleigh+Raman	SC@SC	Ref. [3]
DWCNT-19	(30,1)@(27,19)	ED	SC@SC	Ref. [3]
DWCNT-20	(13,5)@(18,11)	Rayleigh+Raman	SC@SC	this work
DWCNT-21	(22,17)@(30,20)	ED	SC@SC	this work

Section S2. Complete set of Rayleigh, RBLM and G-band spectra for investigated DWCNTs

DWCNT-1: **(14,1)@(15,12), SC@M**

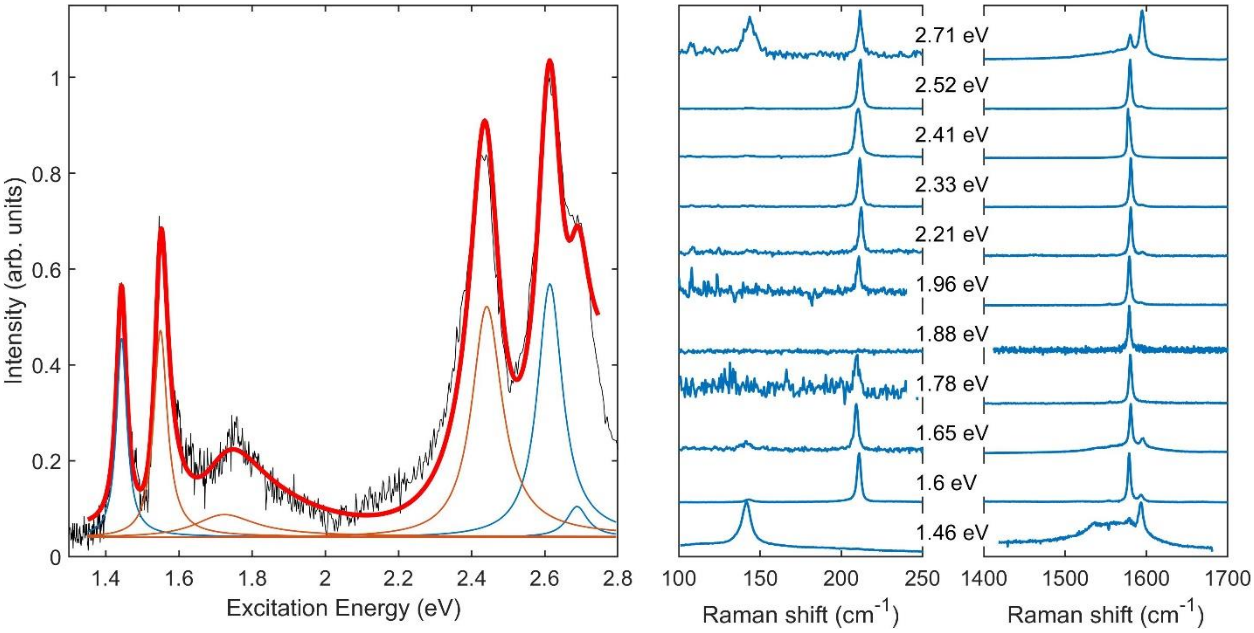

Figure S2.1. Rayleigh spectrum (left) and RBLM and G-band Raman spectra (right) for DWCNT (14,1)@(15,12). The peak at ~1.72 eV in the Rayleigh spectrum corresponds to the electron-phonon sideband of the S_{22}^{in} transition.

Table S2.1. Optical transition energies for isolated SWCNTs and van-der-Waals coupled layers of DWCNT (14,1)@(15,12) with equal and opposite handedness, shown as DW(1) and DW(-1), respectively. SWCNT energies were estimated using the formula from Ref. [6], while those of DWCNT layers were calculated using the adapted code from Ref. [7]. The transition energy values are given in eV.

	In	$\mathbf{S_{11}^{in}}$	$\mathbf{S_{22}^{in}}$	$\mathbf{S_{33}^{in}}$	$\mathbf{S_{44}^{in}}$	$\mathbf{S_{55}^{in}}$	$\mathbf{S_{66}^{in}}$
(14,1)@(15,12) **SC1@M**	SWCNT	0.841	1.671	2.504	3.735	-	-
	DW(1)	0.788	1.57	2.309	3.588	-	-
	DW(-1)	0.789	1.571	2.394	3.592	-	-
	Out	$\mathbf{M_{11L}^{out}}$	$\mathbf{M_{11H}^{out}}$	$\mathbf{M_{22L}^{out}}$	$\mathbf{M_{22H}^{out}}$	$\mathbf{M_{33L}^{out}}$	$\mathbf{M_{33H}^{out}}$
	SWCNT	1.467	1.498	2.673	2.778	-	-
	DW(1)	1.413	1.443	2.617	2.695	-	-
	DW(-1)	1.413	1.444	2.615	2.721	-	-

DWCNT-2: **(14,2)@(22,4), M@M**

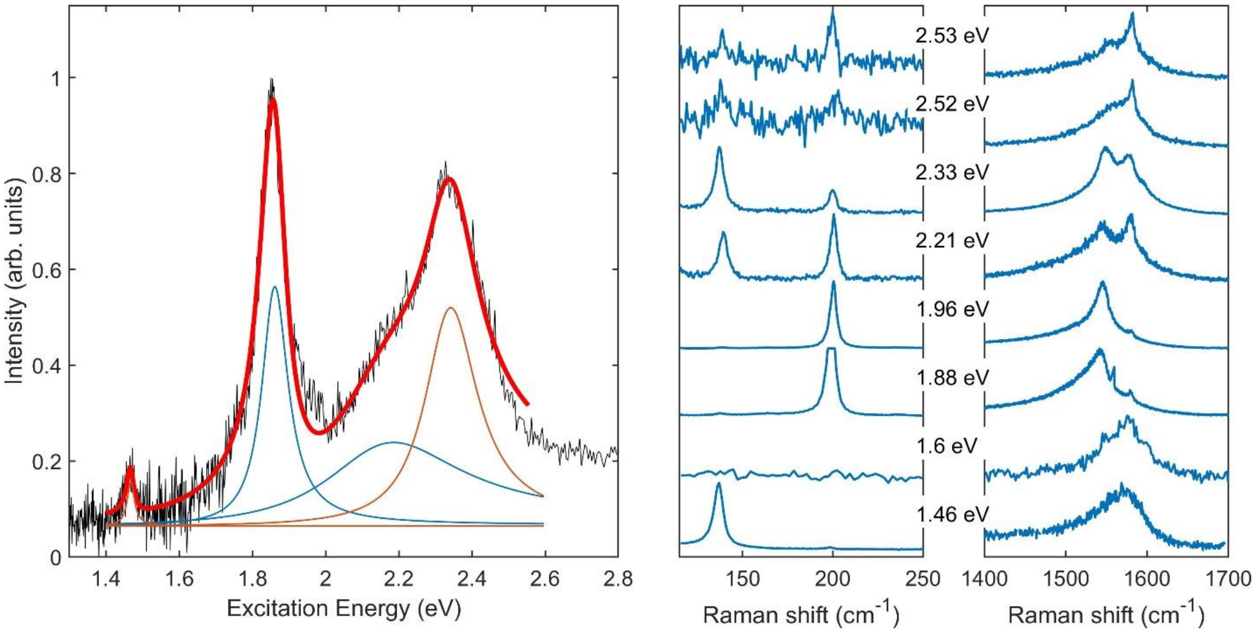

Figure S2.2. Rayleigh spectrum (left) and RBLM and G-band Raman spectra (right) for DWCNT (14,2)@(22,4).

Table S2.2. Optical transition energies for isolated SWCNTs and van-der-Waals coupled layers of DWCNT (14,2)@(22,4) with equal and opposite handedness, shown as DW(1) and DW(-1), respectively. SWCNT energies were estimated using the formula from Ref. [6], while those of DWCNT layers were calculated using the adapted code from Ref. [7]. The transition energy values are given in eV.

(14,2)@(22,4) M@M	**In**	$\mathbf{M}_{\mathbf{11L}}^{\boldsymbol{in}}$	$\mathbf{M}_{\mathbf{11H}}^{\boldsymbol{in}}$	$\mathbf{M}_{\mathbf{22L}}^{\boldsymbol{in}}$	$\mathbf{M}_{\mathbf{22H}}^{\boldsymbol{in}}$	$\mathbf{M}_{\mathbf{33L}}^{\boldsymbol{in}}$	$\mathbf{M}_{\mathbf{33H}}^{\boldsymbol{in}}$
	SWCNT	1.941	2.307	2.900	4.150	-	-
	DW(1)	1.872	2.238	2.786	4.064	-	-
	DW(-1)	1.853	2.207	3.62	4.182	-	-
	Out	$\mathbf{M}_{\mathbf{11L}}^{\mathbf{out}}$	$\mathbf{M}_{\mathbf{11H}}^{\mathbf{out}}$	$\mathbf{M}_{\mathbf{22L}}^{\mathbf{out}}$	$\mathbf{M}_{\mathbf{22H}}^{\mathbf{out}}$	$\mathbf{M}_{\mathbf{33L}}^{\mathbf{out}}$	$\mathbf{M}_{\mathbf{33H}}^{\mathbf{out}}$
	SWCNT	1.370	1.508	2.426	2.894	3.038	3.891
	DW(1)	1.312	1.455	2.385	2.842	3.017	3.839
	DW(-1)	1.316	1.451	2.369	2.839	2.974	3.837

DWCNT-3: **(11,8)@(19,10), M@M**

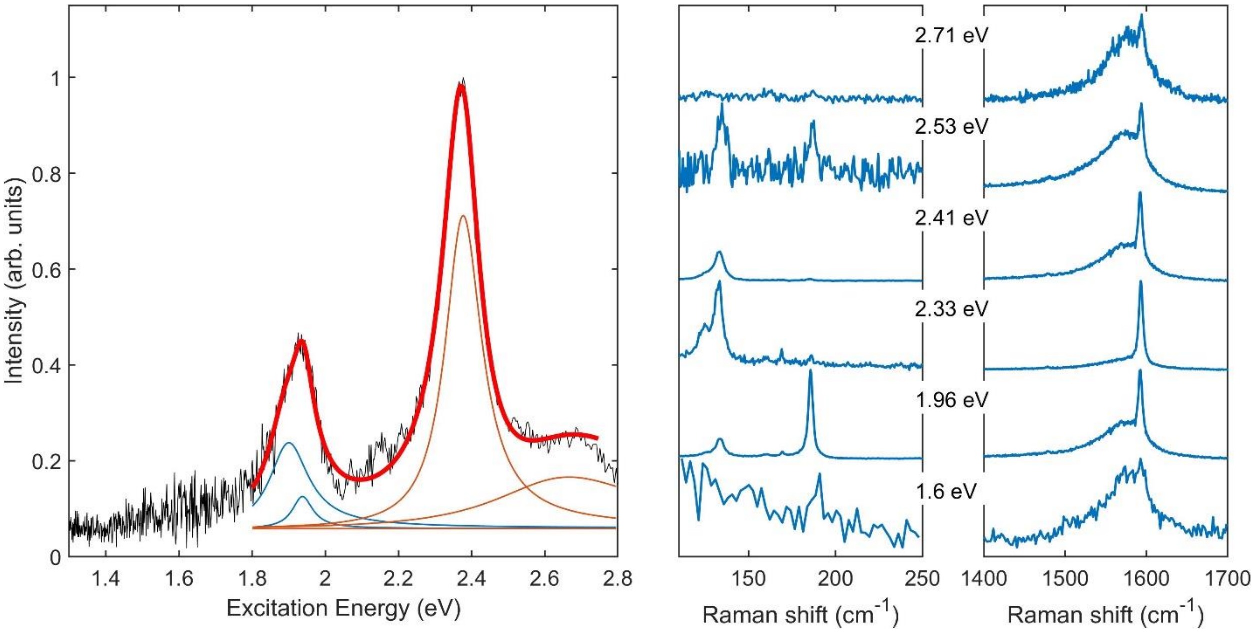

Figure S2.3. Rayleigh spectrum (left) and RBLM and G-band Raman spectra (right) for DWCNT (11,8)@(19,10).

Table S2.3. Optical transition energies for isolated SWCNTs and van-der-Waals coupled layers of DWCNT (11,8)@(19,10) with equal and opposite handedness, shown as DW(1) and DW(-1), respectively. SWCNT energies were estimated using the formula from Ref. [6], while those of DWCNT layers were calculated using the adapted code from Ref. [7]. The transition energy values are given in eV.

(11,8)@(19,10) **M@M**	**In**	$\mathbf{M_{11L}^{in}}$	$\mathbf{M_{11H}^{in}}$	$\mathbf{M_{22L}^{in}}$	$\mathbf{M_{22H}^{in}}$	$\mathbf{M_{33L}^{in}}$	$\mathbf{M_{33H}^{in}}$
	SWCNT	1.936	2.024	3.228	3.527	3.626	4.171
	DW(1)	1.856	1.984	3.098	3.454	3.24	4.081
	DW(-1)	1.863	1.941	3.167	3.413	3.516	3.981
	Out	$\mathbf{M_{11L}^{out}}$	$\mathbf{M_{11H}^{out}}$	$\mathbf{M_{22L}^{out}}$	$\mathbf{M_{22H}^{out}}$	$\mathbf{M_{33L}^{out}}$	$\mathbf{M_{33H}^{out}}$
	SWCNT	1.342	1.411	2.447	2.682	3.159	3.589
	DW(1)	1.269	1.357	2.417	2.629	3.15	3.534
	DW(-1)	1.289	1.357	2.378	2.629	3.133	3.534

DWCNT-4: **(14,8)@(19,14), M@SC**

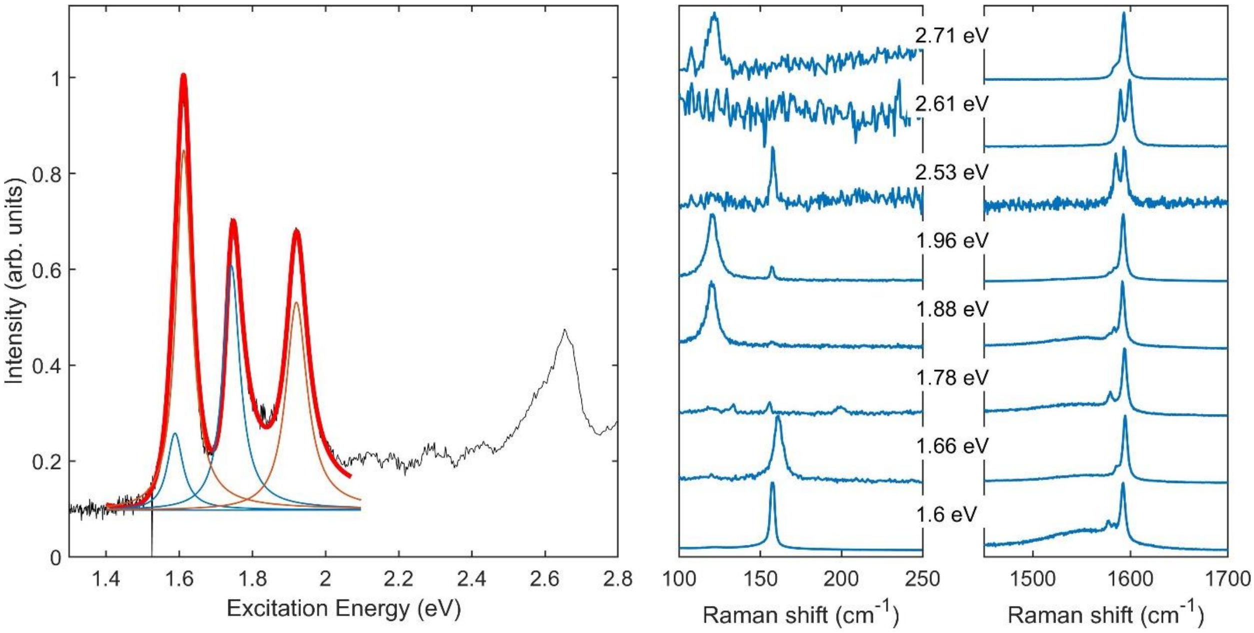

Figure S2.4. Rayleigh spectrum (left) and RBLM and G-band Raman spectra (right) for DWCNT (14,8)@(19,14).

Table S2.4. Optical transition energies for isolated SWCNTs and van-der-Waals coupled layers of DWCNT (14,8)@(19,14) with equal and opposite handedness, shown as DW(1) and DW(-1), respectively. SWCNT energies were estimated using the formula from Ref. [6], while those of DWCNT layers were calculated using the adapted code from Ref. [7]. The transition energy values are given in eV.

(14,8)@(19,14) M@SC2	**In**	$\mathbf{M}_{11L}^{in}$	$\mathbf{M}_{11H}^{in}$	$\mathbf{M}_{22L}^{in}$	$\mathbf{M}_{22H}^{in}$	$\mathbf{M}_{33L}^{in}$	$\mathbf{M}_{33H}^{in}$	-
	SWCNT	1.693	1.801	2.912	3.280	3.462	4.132	-
	DW(1)	1.651	1.794	2.862	3.224	3.406	4.203	-
	DW(-1)	1.634	1.737	2.862	3.207	3.4	4.043	-
	Out	$\mathbf{S}_{11}^{out}$	$\mathbf{S}_{22}^{out}$	$\mathbf{S}_{33}^{out}$	$\mathbf{S}_{44}^{out}$	$\mathbf{S}_{55}^{out}$	$\mathbf{S}_{66}^{out}$	$\mathbf{S}_{77}^{out}$
	SWCNT	0.468	0.830	1.686	1.981	2.700	2.837	3.507
	DW(1)	0.447	0.766	1.599	1.917	2.633	2.772	3.437
	DW(-1)	0.407	0.77	1.625	1.917	2.639	2.786	3.445

DWCNT-5: **(14,5)@(26,1), M@SC**

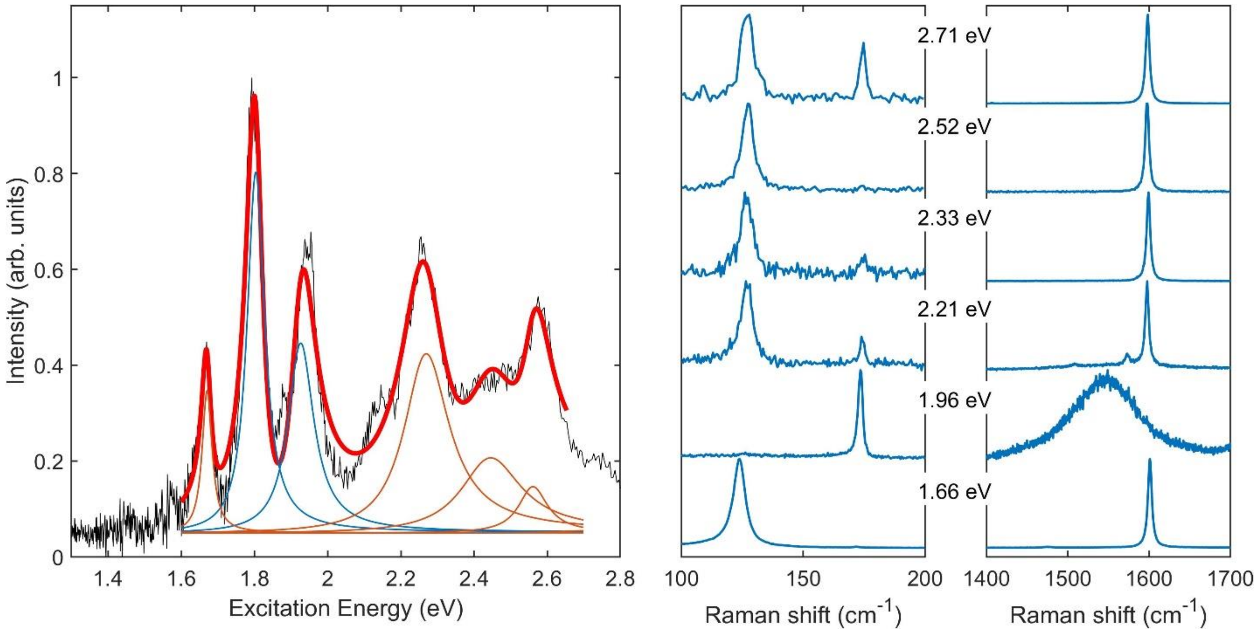

Figure S2.5. Rayleigh spectrum (left) and RBLM and G-band Raman spectra (right) for DWCNT (14,5)@(26,1).

Table S2.5. Optical transition energies for isolated SWCNTs and van-der-Waals coupled layers of DWCNT (14,5)@(26,1) with equal and opposite handedness, shown as DW(1) and DW(-1), respectively. SWCNT energies were estimated using the formula from Ref. [6], while those of DWCNT layers were calculated using the adapted code from Ref. [7]. The transition energy values are given in eV.

(14,5)@(26,1) M@SC1	**In**	$\mathbf{M}_{\mathbf{11L}}^{in}$	$\mathbf{M}_{\mathbf{11H}}^{in}$	$\mathbf{M}_{\mathbf{22L}}^{in}$	$\mathbf{M}_{\mathbf{22H}}^{in}$	$\mathbf{M}_{\mathbf{33L}}^{in}$	$\mathbf{M}_{\mathbf{33H}}^{in}$
	SWCNT	1.821	2.040	2.948	3.695	-	-
	DW(1)	1.761	1.976	2.873	3.669	-	-
	DW(-1)	1.76	1.976	2.869	3.62	-	-
	Out	$\mathbf{S}_{\mathbf{11}}^{\mathbf{out}}$	$\mathbf{S}_{\mathbf{22}}^{\mathbf{out}}$	$\mathbf{S}_{\mathbf{33}}^{\mathbf{out}}$	$\mathbf{S}_{\mathbf{44}}^{\mathbf{out}}$	$\mathbf{S}_{\mathbf{55}}^{\mathbf{out}}$	$\mathbf{S}_{\mathbf{66}}^{\mathbf{out}}$
	SWCNT	0.487	0.943	1.684	2.294	2.562	3.407
	DW(1)	0.427	0.881	1.623	2.233	2.497	3.346
	DW(-1)	0.427	0.881	1.623	2.233	2.499	3.346

DWCNT-6: **(18,2)@(19,13), SC@M**

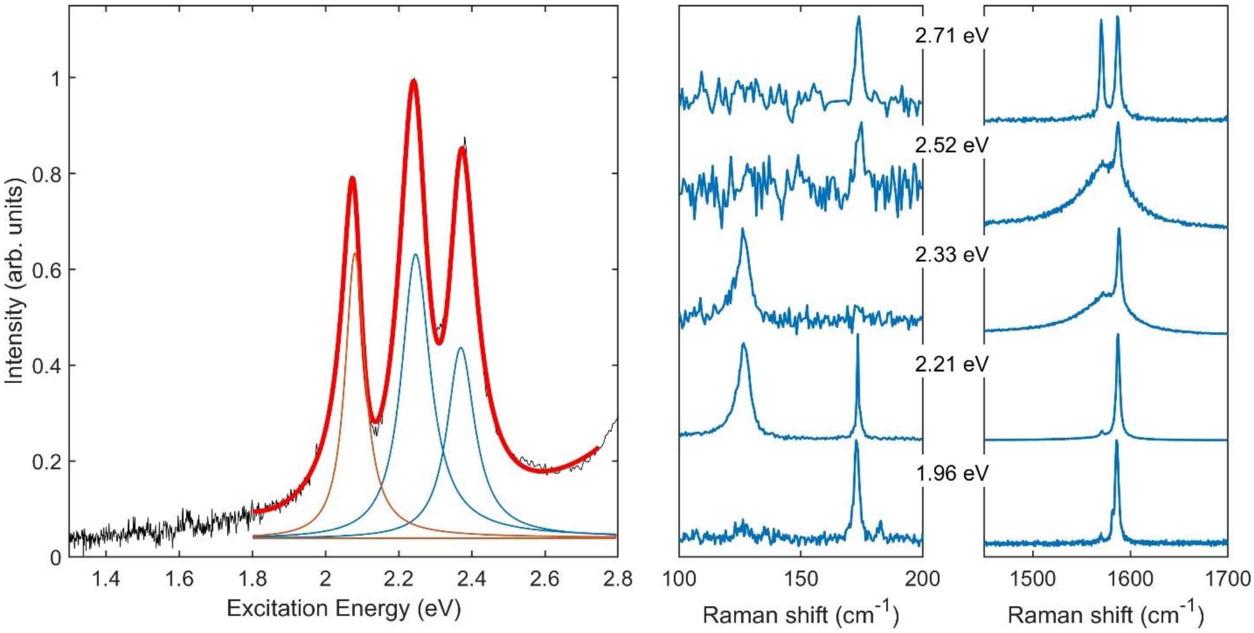

Figure S2.6. Rayleigh spectrum (left) and RBLM and G-band Raman spectra (right) for DWCNT (18,2)@(19,13).

Table S2.6. Optical transition energies for isolated SWCNTs and van-der-Waals coupled layers of DWCNT (18,2)@(19,13) with equal and opposite handedness, shown as DW(1) and DW(-1), respectively. SWCNT energies were estimated using the formula from Ref. [6], while those of DWCNT layers were calculated using the adapted code from Ref. [7]. The transition energy values are given in eV.

(18,2)@(19,13) **SC1@M**	**In**	$\mathbf{S_{11}^{in}}$	$\mathbf{S_{22}^{in}}$	$\mathbf{S_{33}^{in}}$	$\mathbf{S_{44}^{in}}$	$\mathbf{S_{55}^{in}}$	$\mathbf{S_{66}^{in}}$
	SWCNT	0.660	1.290	2.140	3.018	-	-
	DW(1)	0.609	1.188	1.982	2.881	-	-
	DW(-1)	0.611	1.192	2.054	2.887	-	-
	Out	$\mathbf{M_{11L}^{out}}$	$\mathbf{M_{11H}^{out}}$	$\mathbf{M_{22L}^{out}}$	$\mathbf{M_{22H}^{out}}$	$\mathbf{M_{33L}^{out}}$	$\mathbf{M_{33H}^{out}}$
	SWCNT	1.255	1.292	2.339	2.463	3.096	3.322
	DW(1)	1.201	1.236	2.283	2.349	3.035	3.287
	DW(-1)	1.202	1.238	2.283	2.407	3.031	3.251

DWCNT-7: **(18,6)@(21,14), M@SC**

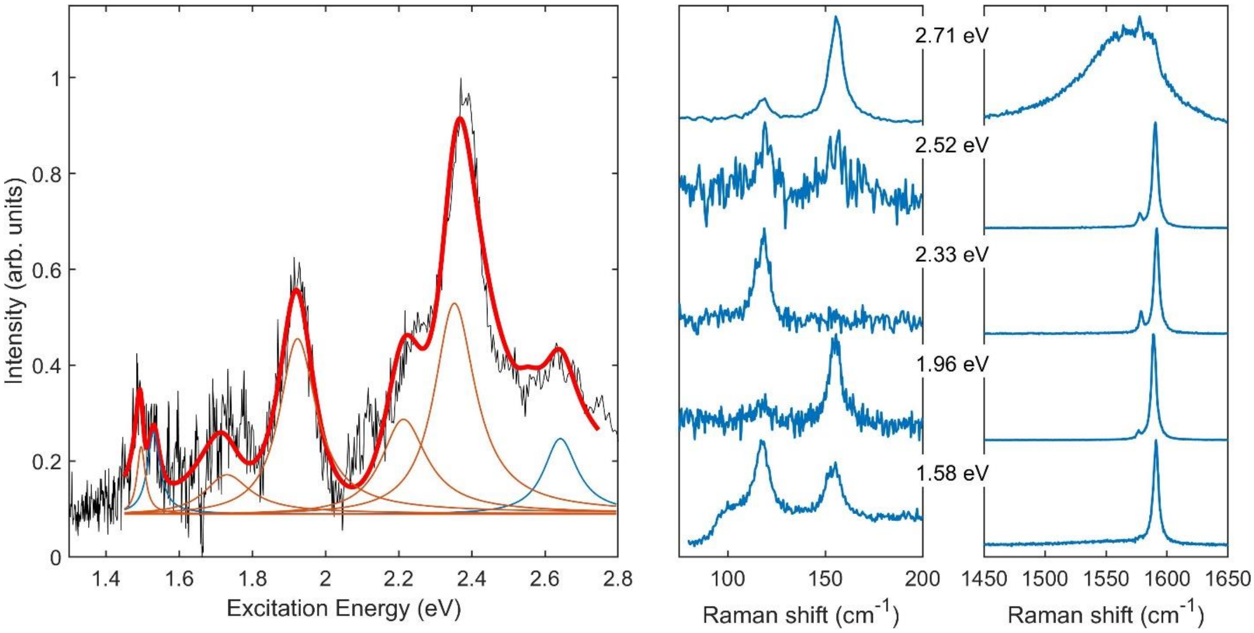

Figure S2.7. Rayleigh spectrum (left) and RBLM and G-band Raman spectra (right) for DWCNT (18,6)@(21,14).

Table S2.7. Optical transition energies for isolated SWCNTs and van-der-Waals coupled layers of DWCNT (18,6)@(21,14) with equal and opposite handedness, shown as DW(1) and DW(-1), respectively. SWCNT energies were estimated using the formula from Ref. [6], while those of DWCNT layers were calculated using the adapted code from Ref. [7]. The transition energy values are given in eV.

(18,6)@(21,14) **M@SC1**	**In**	$\mathbf{M}_{\mathbf{11L}}^{\boldsymbol{in}}$	$\mathbf{M}_{\mathbf{11H}}^{\boldsymbol{in}}$	$\mathbf{M}_{\mathbf{22L}}^{\boldsymbol{in}}$	$\mathbf{M}_{\mathbf{22H}}^{\boldsymbol{in}}$	$\mathbf{M}_{\mathbf{33L}}^{\boldsymbol{in}}$	$\mathbf{M}_{\mathbf{33H}}^{\boldsymbol{in}}$	-
	SWCNT	1.516	1.658	2.636	3.119	3.209	4.089	-
	DW(1)	1.574	1.56	2.605	2.983	3.162	3.83	-
	DW(-1)	1.457	1.572	2.54	3.011	3.223	3.949	-
	Out	$\mathbf{S}_{\mathbf{11}}^{\mathbf{out}}$	$\mathbf{S}_{\mathbf{22}}^{\mathbf{out}}$	$\mathbf{S}_{\mathbf{33}}^{\mathbf{out}}$	$\mathbf{S}_{\mathbf{44}}^{\mathbf{out}}$	$\mathbf{S}_{\mathbf{55}}^{\mathbf{out}}$	$\mathbf{S}_{\mathbf{66}}^{\mathbf{out}}$	$\mathbf{S}_{\mathbf{77}}^{\mathbf{out}}$
	SWCNT	0.434	0.803	1.554	1.953	2.471	2.882	3.125
	DW(1)	0.371	0.73	1.489	1.919	2.402	2.843	3.049
	DW(-1)	0.374	0.741	1.492	1.891	2.403	2.818	3.017

DWCNT-8: **(22,13)@(39,2), M@SC**

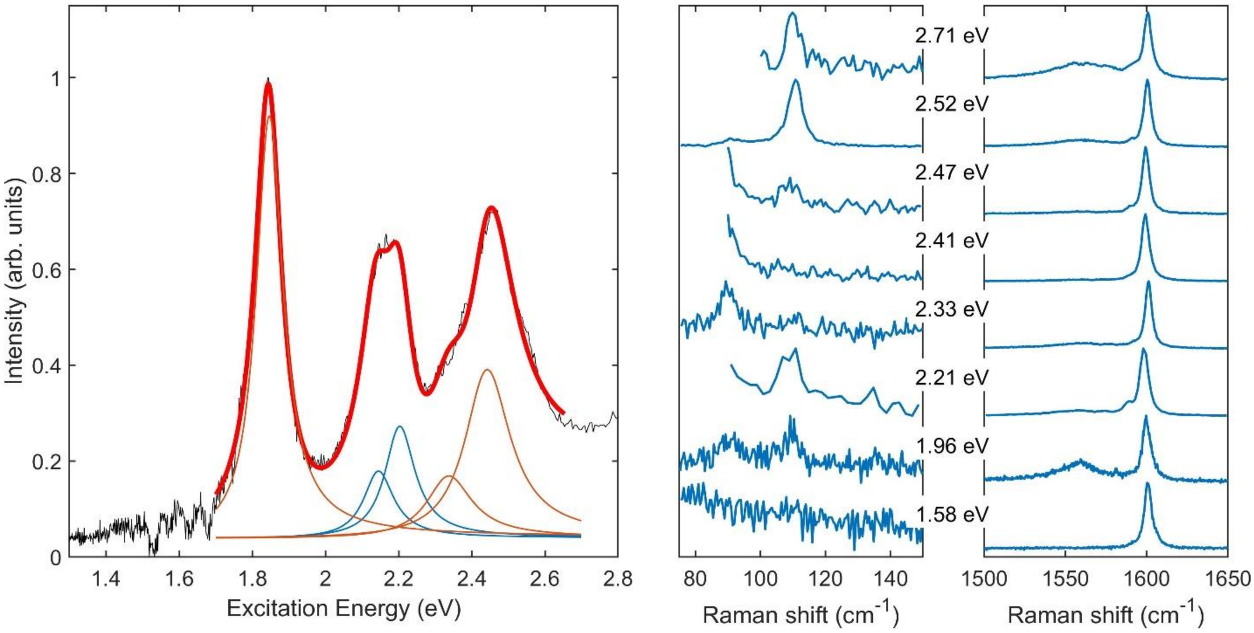

Figure S2.8. Rayleigh spectrum (left) and RBLM and G-band Raman spectra (right) for DWCNT (22,13)@(39,2).

Table S2.8. Optical transition energies for isolated SWCNTs and van-der-Waals coupled layers of DWCNT (22,13)@(39,2) with equal and opposite handedness, shown as DW(1) and DW(-1), respectively. SWCNT energies were estimated using the formula from Ref. [6], while those of DWCNT layers were calculated using the adapted code from Ref. [7]. The transition energy values are given in eV.

(22,13)@(39,2) **M@SC1**	**In**	$\mathbf{M_{11L}^{in}}$	$\mathbf{M_{11H}^{in}}$	$\mathbf{M_{22L}^{in}}$	$\mathbf{M_{22H}^{in}}$	$\mathbf{M_{33L}^{in}}$	$\mathbf{M_{33H}^{in}}$	-
	SWCNT	1.150	1.191	2.163	2.301	2.901	3.153	-
	DW(1)	1.092	1.132	2.098	2.237	2.825	3.081	-
	DW(-1)	1.094	1.132	2.101	2.238	2.83	3.083	-
	Out	$\mathbf{S_{11}^{out}}$	$\mathbf{S_{22}^{out}}$	$\mathbf{S_{33}^{out}}$	$\mathbf{S_{44}^{out}}$	$\mathbf{S_{55}^{out}}$	$\mathbf{S_{66}^{out}}$	$\mathbf{S_{77}^{out}}$
	SWCNT	0.330	0.631	1.201	1.586	1.945	2.435	2.492
	DW(1)	0.269	0.57	1.14	1.524	1.884	2.373	2.428
	DW(-1)	0.269	0.57	1.14	1.525	1.884	2.374	2.429

DWCNT-9: **(17,14)@(26,14), M@M**

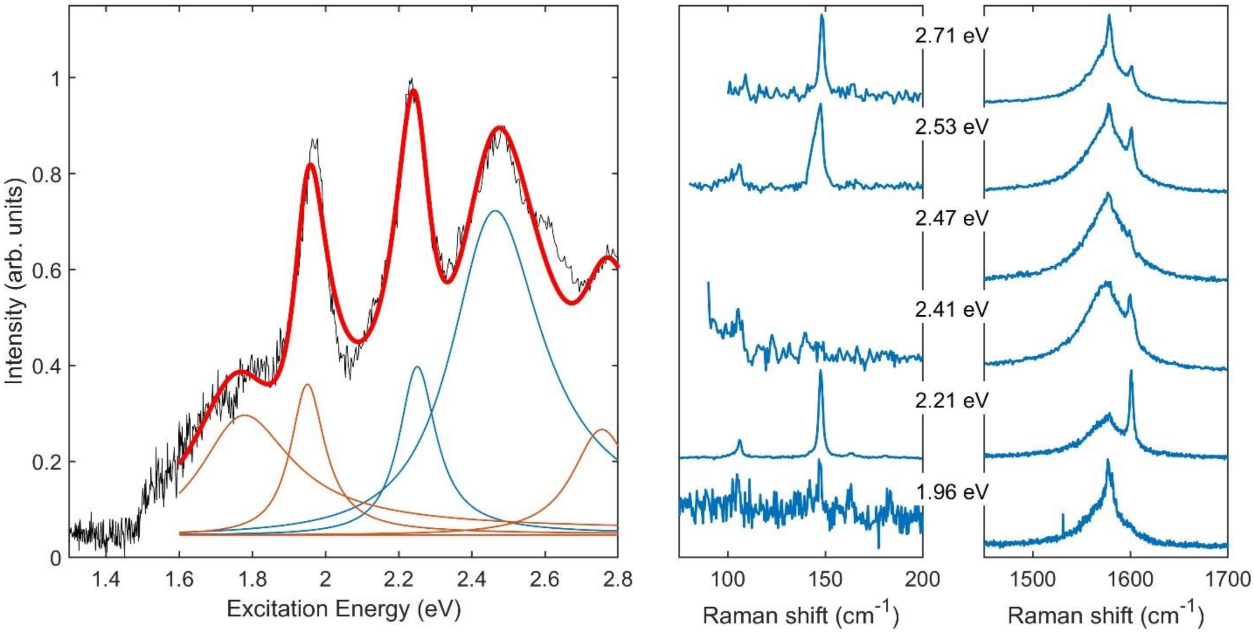

Figure S2.9. Rayleigh spectrum (left) and RBLM and G-band Raman spectra (right) for DWCNT (17,14)@(26,14).

Table S2.9. Optical transition energies for isolated SWCNTs and van-der-Waals coupled layers of DWCNT (17,14)@(26,14) with equal and opposite handedness, shown as DW(1) and DW(-1), respectively. SWCNT energies were estimated using the formula from Ref. [6], while those of DWCNT layers were calculated using the adapted code from Ref. [7]. The transition energy values are given in eV.

(17,14)@(26,14) M@M	**In**	$\mathbf{M_{11L}^{in}}$	$\mathbf{M_{11H}^{in}}$	$\mathbf{M_{22L}^{in}}$	$\mathbf{M_{22H}^{in}}$	$\mathbf{M_{33L}^{in}}$	$\mathbf{M_{33H}^{in}}$
	SWCNT	1.304	1.325	2.432	2.502	3.214	3.341
	DW(1)	1.161	1.14	2.203	2.489	2.801	3.243
	DW(-1)	1.215	1.182	1.98	2.292	3.24	3.046
	Out	$\mathbf{M_{11L}^{out}}$	$\mathbf{M_{11H}^{out}}$	$\mathbf{M_{22L}^{out}}$	$\mathbf{M_{22H}^{out}}$	$\mathbf{M_{33L}^{out}}$	$\mathbf{M_{33H}^{out}}$
	SWCNT	1.016	1.051	1.939	2.060	2.649	2.869
	DW(1)	0.946	0.984	2.091	1.993	NA	2.790
	DW(-1)	0.960	0.988	1.843	1.995	3.051	2.800

DWCNT-10: **(17,14)@(28,12), M@SC**

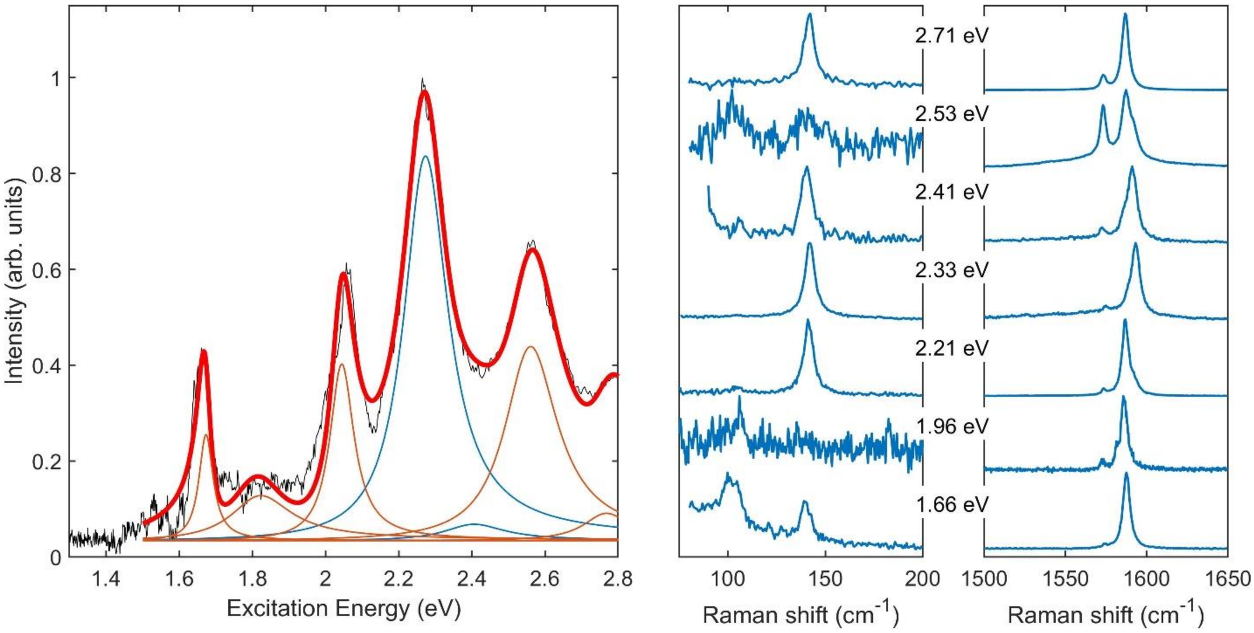

Figure S2.10. Rayleigh spectrum (left) and RBLM and G-band Raman spectra (right) for DWCNT (17,14)@(28,12).

Table S2.10. Optical transition energies for isolated SWCNTs and van-der-Waals coupled layers of DWCNT (17,14)@(28,12) with equal and opposite handedness, shown as DW(1) and DW(-1), respectively. SWCNT energies were estimated using the formula from Ref. [6], while those of DWCNT layers were calculated using the adapted code from Ref. [7]. The transition energy values are given in eV.

(17,14)@(28,12) **M@SC1**	**In**	$\mathbf{M}_{\mathbf{11L}}^{in}$	$\mathbf{M}_{\mathbf{11H}}^{in}$	$\mathbf{M}_{\mathbf{22L}}^{in}$	$\mathbf{M}_{\mathbf{22H}}^{in}$	$\mathbf{M}_{\mathbf{33L}}^{in}$	$\mathbf{M}_{\mathbf{33H}}^{in}$	-
	SWCNT	1.304	1.325	2.432	2.502	3.214	3.341	-
	DW(1)	1.210	1.246	2.302	2.315	3.036	3.273	-
	DW(-1)	1.237	1.232	2.318	2.378	3.201	3.179	-
	Out	$\mathbf{S}_{\mathbf{11}}^{\mathbf{out}}$	$\mathbf{S}_{\mathbf{22}}^{\mathbf{out}}$	$\mathbf{S}_{\mathbf{33}}^{\mathbf{out}}$	$\mathbf{S}_{\mathbf{44}}^{\mathbf{out}}$	$\mathbf{S}_{\mathbf{55}}^{\mathbf{out}}$	$\mathbf{S}_{\mathbf{66}}^{\mathbf{out}}$	$\mathbf{S}_{\mathbf{77}}^{\mathbf{out}}$
	SWCNT	0.372	0.701	1.348	1.737	2.170	2.623	2.773
	DW(1)	0.317	0.634	1.281	1.671	1.984	2.556	2.738
	DW(-1)	0.313	0.637	1.284	1.673	2.094	2.558	2.617

DWCNT-11: **SC@M**

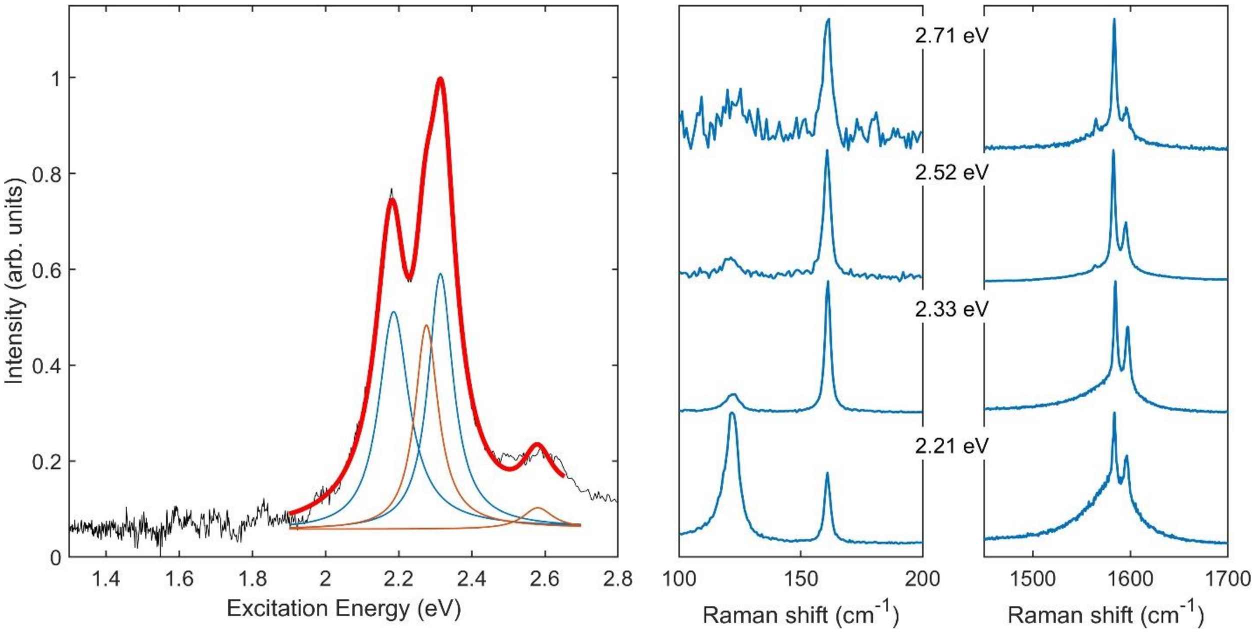

Figure S2.11. Rayleigh spectrum (left) and RBLM and G-band Raman spectra (right) for DWCNT-11.

Table S2.11. Optical transition energies for isolated SWCNTs and van-der-Waals coupled layers of DWCNT-11 with equal and opposite handedness, shown as DW(1) and DW(-1), respectively. SWCNT energies were estimated using the formula from Ref. [6], while those of DWCNT layers were calculated using the adapted code from Ref. [7]. The "std" and "mad" stand for standard deviation and mean absolute deviation. All energy values are given in eV.

SC1@M	**In**	$\boldsymbol{S_{11}^{in}}$	$\mathbf{S_{22}^{in}}$	$\mathbf{S_{33}^{in}}$	$\mathbf{S_{44}^{in}}$	$\mathbf{S_{55}^{in}}$	$\mathbf{S_{66}^{in}}$
	SWCNT	0.668	1.276	2.184	2.96	3.157	4.023
	std	0.011	0.021	0.055	0.059	0.106	0.134
	DW(1)	-0.061	-0.071	-0.067	-0.072	-0.064	-0.081
	mad	0.002	0.008	0.008	0.008	0.019	0.016
	DW(-1)	-0.060	-0.071	-0.071	-0.080	-0.079	-0.084
	mad	0.001	0.005	0.007	0.014	0.025	0.017
	Out	$\mathbf{M_{11L}^{out}}$	$\mathbf{M_{11H}^{out}}$	$\mathbf{M_{22L}^{out}}$	$\mathbf{M_{22H}^{out}}$	$\mathbf{M_{33L}^{out}}$	$\mathbf{M_{33H}^{out}}$
	SWCNT	1.217	1.287	2.247	2.485	2.955	3.389
	std	0.02	0.016	0.052	0.048	0.089	0.088
	DW(1)	-0.053	-0.053	-0.053	-0.053	-0.054	-0.052
	mad	0.001	0.000	0.003	0.000	0.008	0.001
	DW(-1)	-0.053	-0.053	-0.054	-0.053	-0.055	-0.053
	mad	0.000	0.000	0.001	0.000	0.003	0.001

DWCNT-12: **M@SC**

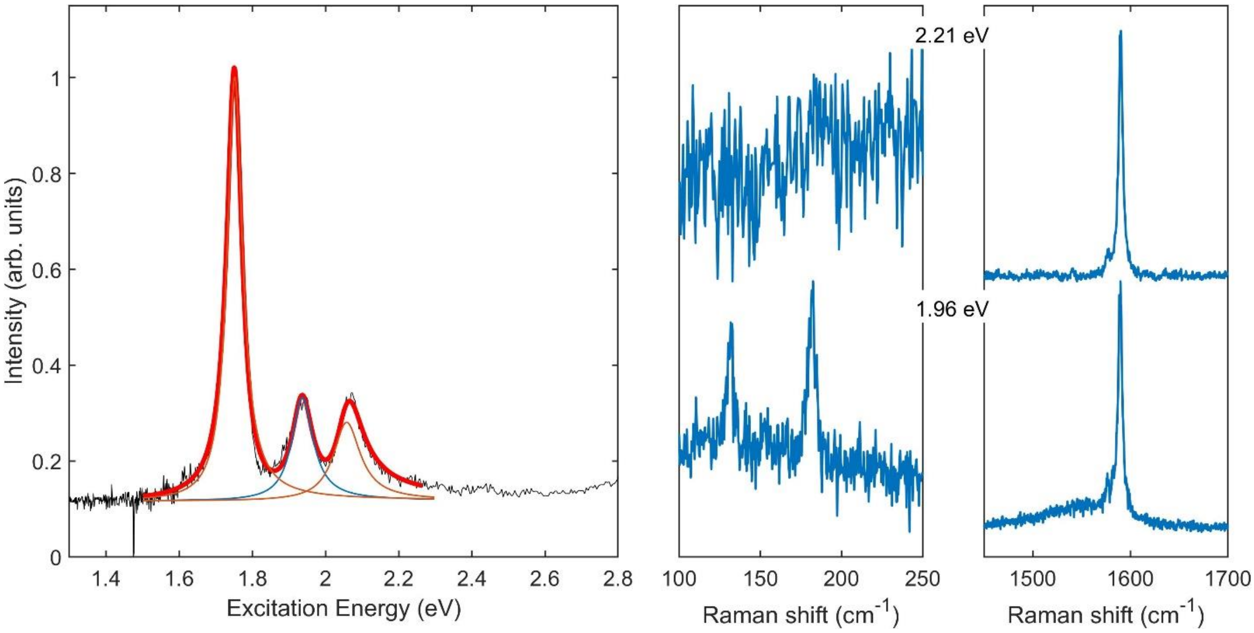

Figure S2.12. Rayleigh spectrum (left) and RBLM and G-band Raman spectra (right) for DWCNT-12.

Table S2.12. Optical transition energies for isolated SWCNTs and van-der-Waals coupled layers of DWCNT-12 with equal and opposite handedness, shown as DW(1) and DW(-1), respectively. SWCNT energies were estimated using the formula from Ref. [6], while those of DWCNT layers were calculated using the adapted code from Ref. [7]. The "std" and "mad" stand for standard deviation and mean absolute deviation. All energy values are given in eV.

	In	$\mathbf{M^{in}_{11L}}$	$\mathbf{M^{in}_{11H}}$	$\mathbf{M^{\mathit{in}}_{22L}}$	$\mathbf{M^{\mathit{in}}_{22H}}$	$\mathbf{M^{in}_{33L}}$	$\mathbf{M^{in}_{33H}}$
M@SC1	SWCNT	1.866	2.035	3.054	3.631	3.803	3.978
	std	0.072	0.067	0.182	0.173	0.114	0.124
	DW(1)	-0.068	-0.064	-0.063	-0.071	-0.080	-0.063
	mad	0.030	0.014	0.045	0.018	0.048	0.020
	DW(-1)	-0.067	-0.074	-0.071	-0.102	-0.063	-0.095
	mad	0.016	0.020	0.059	0.044	0.067	0.047
	Out	$\mathbf{S^{out}_{11}}$	$\mathbf{S^{out}_{22}}$	$\mathbf{S^{out}_{33}}$	$\mathbf{S^{out}_{44}}$	$\mathbf{S^{out}_{55}}$	$\mathbf{S^{out}_{66}}$
	SWCNT	0.505	0.950	1.758	2.286	2.697	3.334
	std	0.010	0.026	0.030	0.069	0.069	0.126
	DW(1)	-0.061	-0.063	-0.063	-0.062	-0.064	-0.061
	mad	0.002	0.002	0.003	0.002	0.009	0.002
	DW(-1)	-0.061	-0.062	-0.063	-0.062	-0.064	-0.062
	mad	0.000	0.001	0.002	0.002	0.005	0.002

DWCNT-13: **SC@M**

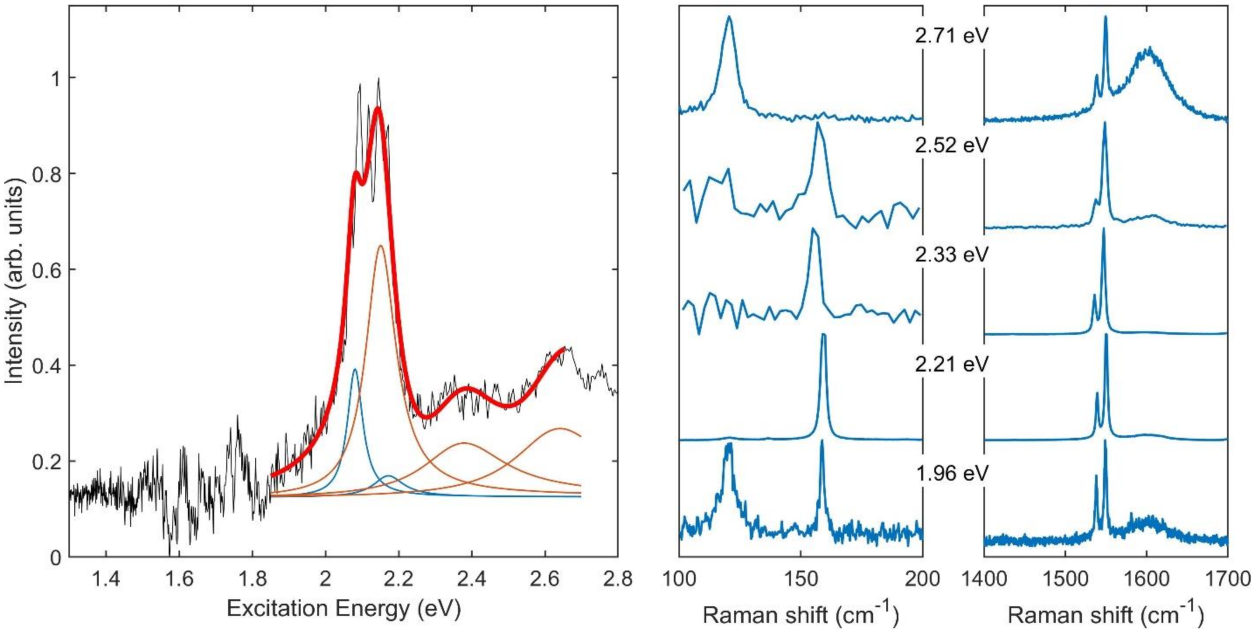

Figure S2.13. Rayleigh spectrum (left) and RBLM and G-band Raman spectra (right) for DWCNT-13.

Table S2.13. Optical transition energies for isolated SWCNTs and van-der-Waals coupled layers of DWCNT-13 with equal and opposite handedness, shown as DW(1) and DW(-1), respectively. SWCNT energies were estimated using the formula from Ref. [6], while those of DWCNT layers were calculated using the adapted code from Ref. [7]. The "std" and "mad" stand for standard deviation and mean absolute deviation. All energy values are given in eV.

	In	$\mathbf{S_{11}^{in}}$	$\mathbf{S_{22}^{in}}$	$\mathbf{S_{33}^{in}}$	$\mathbf{S_{44}^{in}}$	$\mathbf{S_{55}^{in}}$	$\mathbf{S_{66}^{in}}$
SC1@M	SWCNT	0.67	1.265	2.201	2.924	3.181	3.948
	std	0.017	0.041	0.062	0.113	0.122	0.186
	DW(1)	-0.061	-0.068	-0.068	-0.070	-0.073	-0.079
	mad	0.002	0.012	0.014	0.009	0.018	0.017
	DW(-1)	-0.061	-0.072	-0.070	-0.082	-0.073	-0.086
	mad	0.001	0.009	0.009	0.019	0.020	0.023
	Out	$\mathbf{M_{11L}^{out}}$	$\mathbf{M_{11H}^{out}}$	$\mathbf{M_{22L}^{out}}$	$\mathbf{M_{22H}^{out}}$	$\mathbf{M_{33L}^{out}}$	$\mathbf{M_{33H}^{out}}$
	SWCNT	1.224	1.286	2.265	2.477	2.984	3.37
	std	0.026	0.022	0.06	0.061	0.104	0.105
	DW(1)	-0.053	-0.053	-0.053	-0.053	-0.053	-0.053
	mad	0.001	0.001	0.003	0.001	0.011	0.002
	DW(-1)	-0.053	-0.053	-0.054	-0.053	-0.055	-0.053
	mad	0.000	0.001	0.002	0.001	0.005	0.001

DWCNT-14: **SC@M**

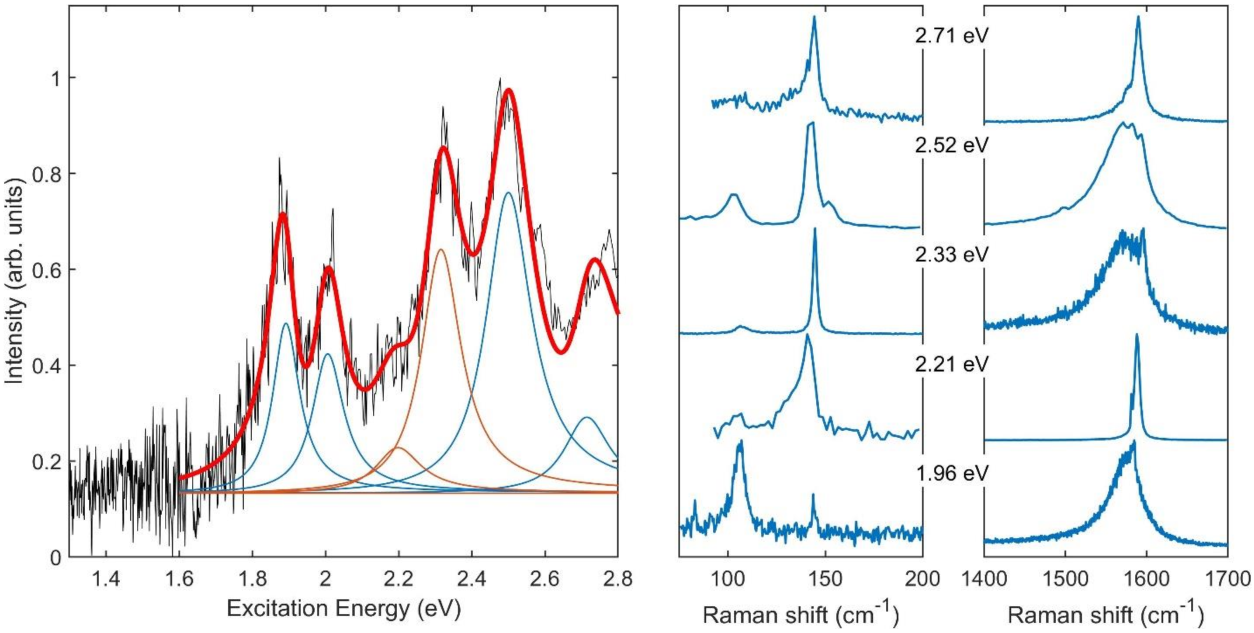

Figure S2.14. Rayleigh spectrum (left) and RBLM and G-band Raman spectra (right) for DWCNT-14.

Table S2.14. Optical transition energies for isolated SWCNTs and van-der-Waals coupled layers of DWCNT-14 with equal and opposite handedness, shown as DW(1) and DW(-1), respectively. SWCNT energies were estimated using the formula from Ref. [6], while those of DWCNT layers were calculated using the adapted code from Ref. [7]. The "std" and "mad" stand for standard deviation and mean absolute deviation. All energy values are given in eV.

SC1@M	**In**	$\mathbf{S_{11}^{in}}$	$\mathbf{S_{22}^{in}}$	$\mathbf{S_{33}^{in}}$	$\mathbf{S_{44}^{in}}$	$\mathbf{S_{55}^{in}}$	$\mathbf{S_{66}^{in}}$
	SWCNT	0.492	0.928	1.718	2.24	2.647	3.282
	std	0.007	0.013	0.036	0.046	0.079	0.104
	DW(1)	-0.061	-0.066	-0.065	-0.064	-0.063	-0.069
	mad	0.001	0.005	0.004	0.004	0.009	0.007
	DW(-1)	-0.060	-0.064	-0.063	-0.067	-0.065	-0.071
	mad	0.001	0.003	0.002	0.005	0.007	0.008
	Out	$\mathbf{M_{11L}^{out}}$	$\mathbf{M_{11H}^{out}}$	$\mathbf{M_{22L}^{out}}$	$\mathbf{M_{22H}^{out}}$	$\mathbf{M_{33L}^{out}}$	$\mathbf{M_{33H}^{out}}$
	SWCNT	0.987	1.029	1.884	2.025	2.578	2.835
	std	0.014	0.011	0.04	0.034	0.068	0.063
	DW(1)	-0.053	-0.053	-0.053	-0.053	-0.053	-0.053
	mad	0.000	0.000	0.001	0.000	0.003	0.001
	DW(-1)	-0.053	-0.053	-0.053	-0.053	-0.053	-0.053
	mad	0.000	0.000	0.000	0.000	0.001	0.000

DWCNT-15: **(11,6)@(18,9), SC@M**

The absorption spectrum of (11,6)@(18,9) DWCNT was previously reported in Ref. [8] (see Fig. 4.23 and Table 4.10). Its fit gives the following DWCNT transition energies: S_{22}^{in} = 1.36 eV, M_{11L}^{out} = 1.46 eV, M_{11H}^{out} = 1.52 eV, M_{22L}^{out} = 2.60 eV, S_{33}^{in} + S_{44}^{in} = 2.77 ± 0.04 eV, M_{22H}^{out} = 2.88 eV.

Table S2.15. Optical transition energies for isolated SWCNTs and van-der-Waals coupled layers of DWCNT (11,6)@(18,9) with equal and opposite handedness, shown as DW(1) and DW(-1), respectively. SWCNT energies were estimated using the formula from Ref. [6], while those of DWCNT layers were calculated using the adapted code from Ref. [7]. The transition energy values are given in eV.

(11,6)@(18,9) **SC@M**	**In**	$\mathbf{S_{11}^{in}}$	$\mathbf{S_{22}^{in}}$	$\mathbf{S_{33}^{in}}$	$\mathbf{S_{44}^{in}}$	$\mathbf{S_{55}^{in}}$	-	-
	SWCNT	0.889	1.444	2.912	2.967	4.127	-	-
	DW(1)	0.783	1.354	2.816	2.709	4.028	-	-
	DW(-1)	0.806	1.373	2.795	2.707	3.943	-	-
	Out	$\mathbf{M_{11L}^{\mathit{in}}}$	$\mathbf{M_{11H}^{\mathit{in}}}$	$\mathbf{M_{22L}^{\mathit{in}}}$	$\mathbf{M_{22H}^{\mathit{in}}}$	$\mathbf{M_{33L}^{\mathit{in}}}$	$\mathbf{M_{33H}^{\mathit{in}}}$	-
	SWCNT	1.420	1.504	2.551	2.839	3.233	3.759	-
	DW(1)	1.424	1.450	2.537	2.785	3.332	3.702	-
	DW(-1)	1.366	1.450	2.489	2.785	3.311	3.701	-

Section S3. Complete set of wide-range Raman and ERS data for investigated DWCNTs

DWCNT-1: **(14,1)@(15,12), SC@M**

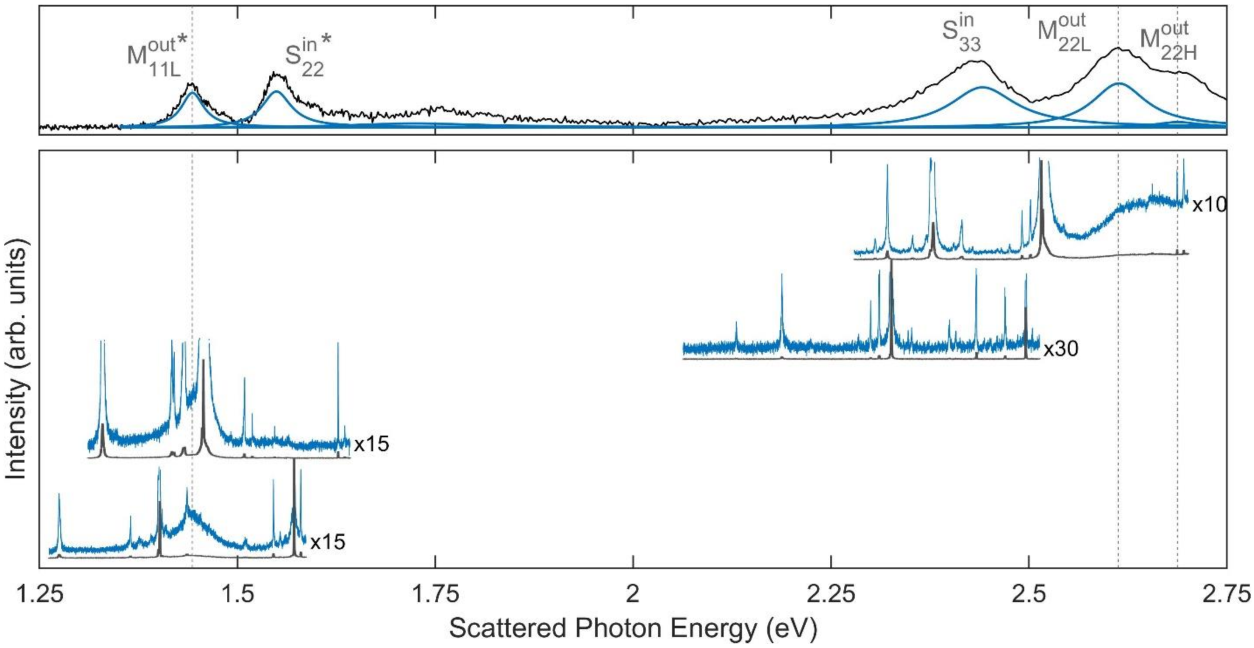

Figure S3.1. Comparison of Rayleigh spectrum (top) and wide-range Raman spectra (bottom) plotted as a function of scattered photon energy for (14,1)@(15,12) DWCNT.

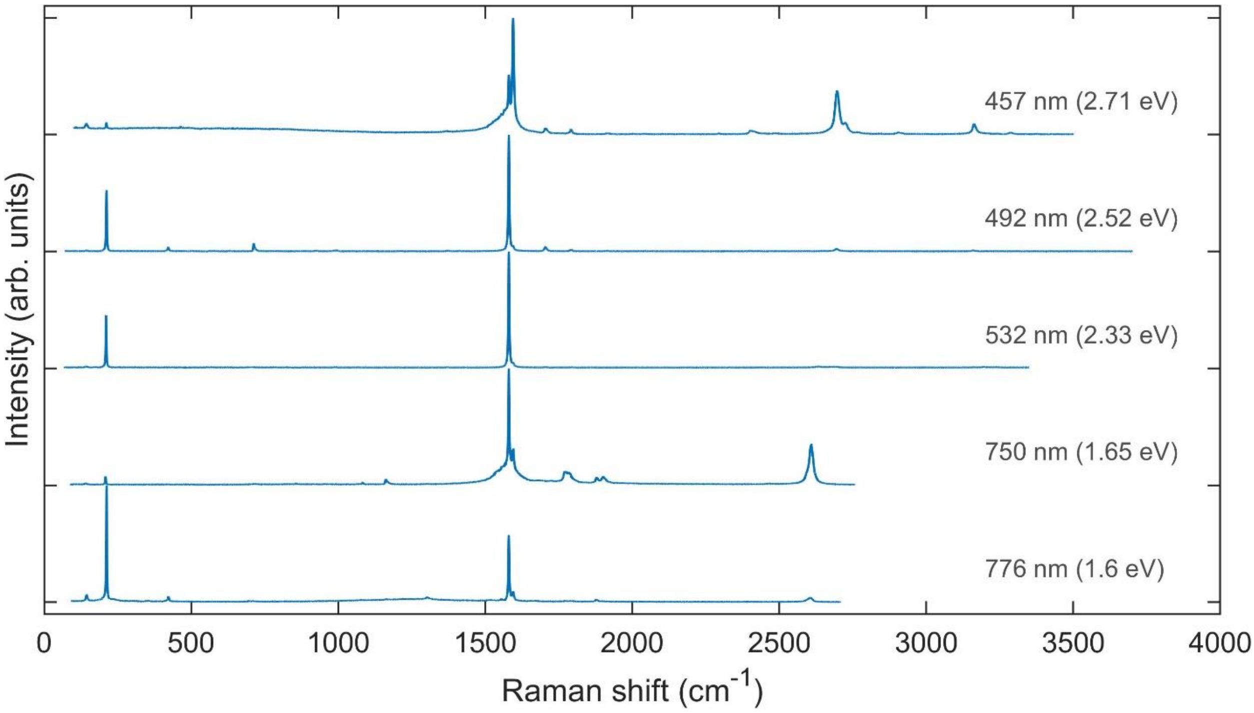

Figure S3.2. All wide-range Raman spectra for (14,1)@(15,12) DWCNT. Labels show the excitation wavelengths of the spectra.

DWCNT-2: **(14,2)@(22,4), M@M**

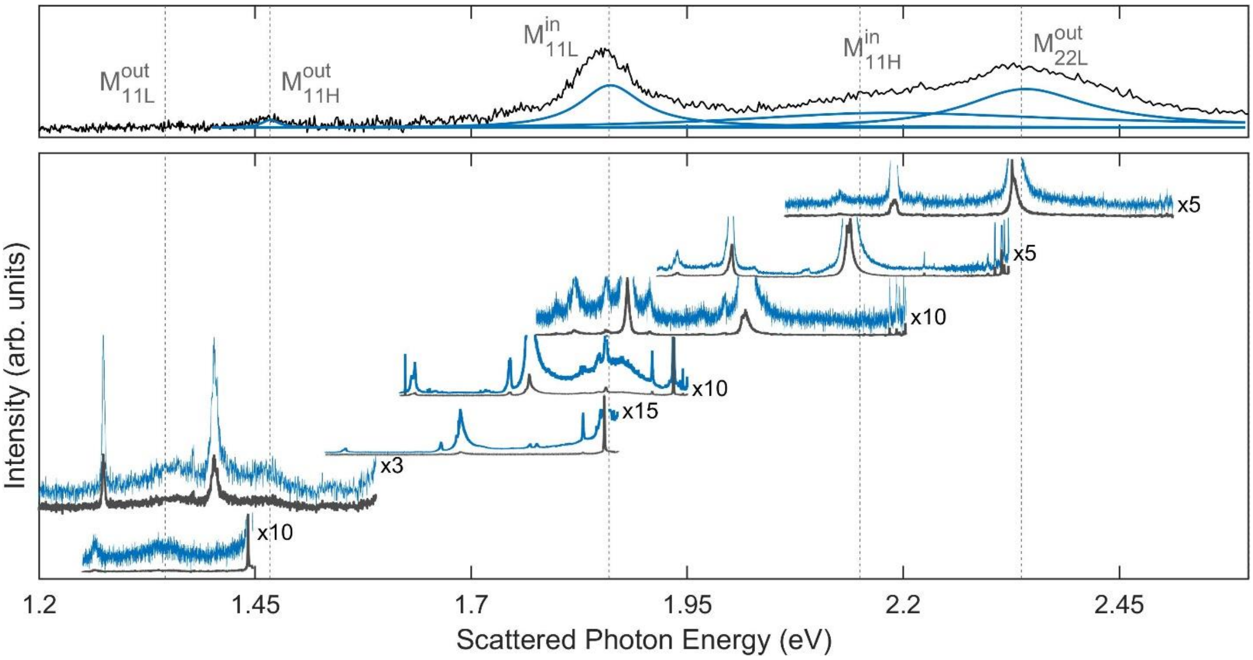

Figure S3.3. Comparison of Rayleigh spectrum (top) and wide-range Raman spectra (bottom) plotted as a function of scattered photon energy for (14,2)@(22,4) DWCNT.

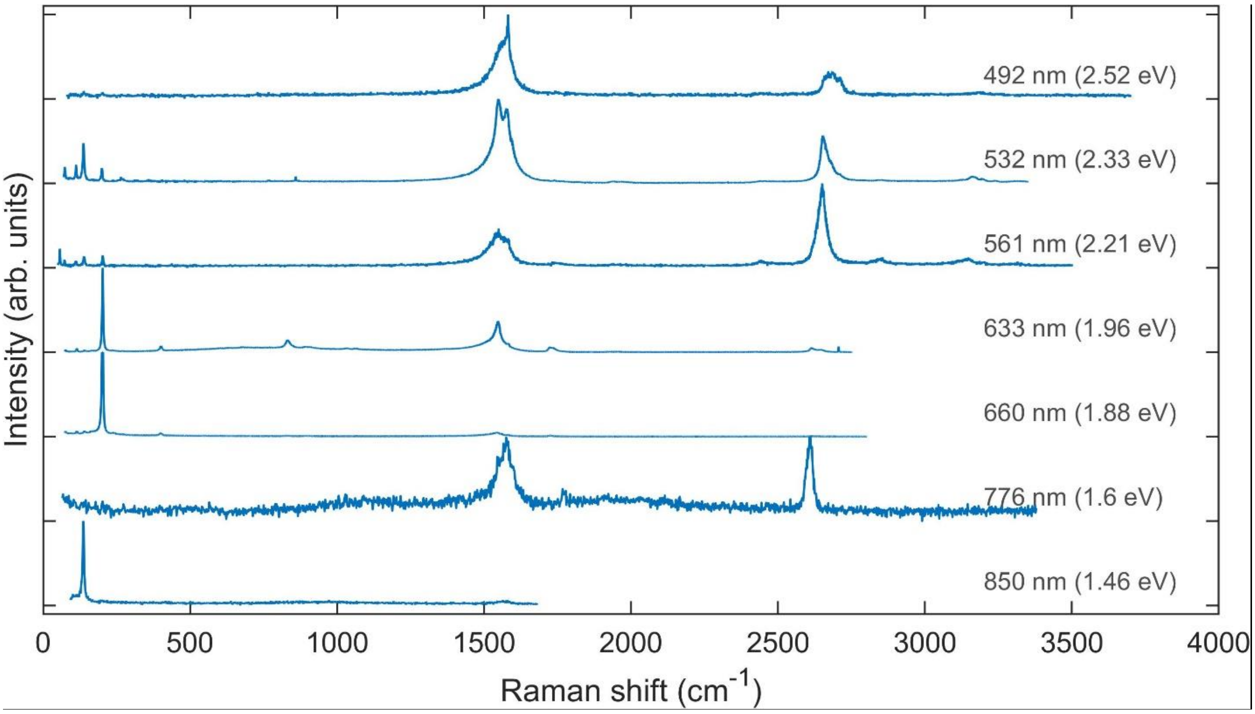

Figure S3.4. All wide-range Raman spectra for (14,2)@(22,4) DWCNT. Labels show the excitation wavelengths of the spectra.

DWCNT-3: **(11,8)@(19,10), M@M**

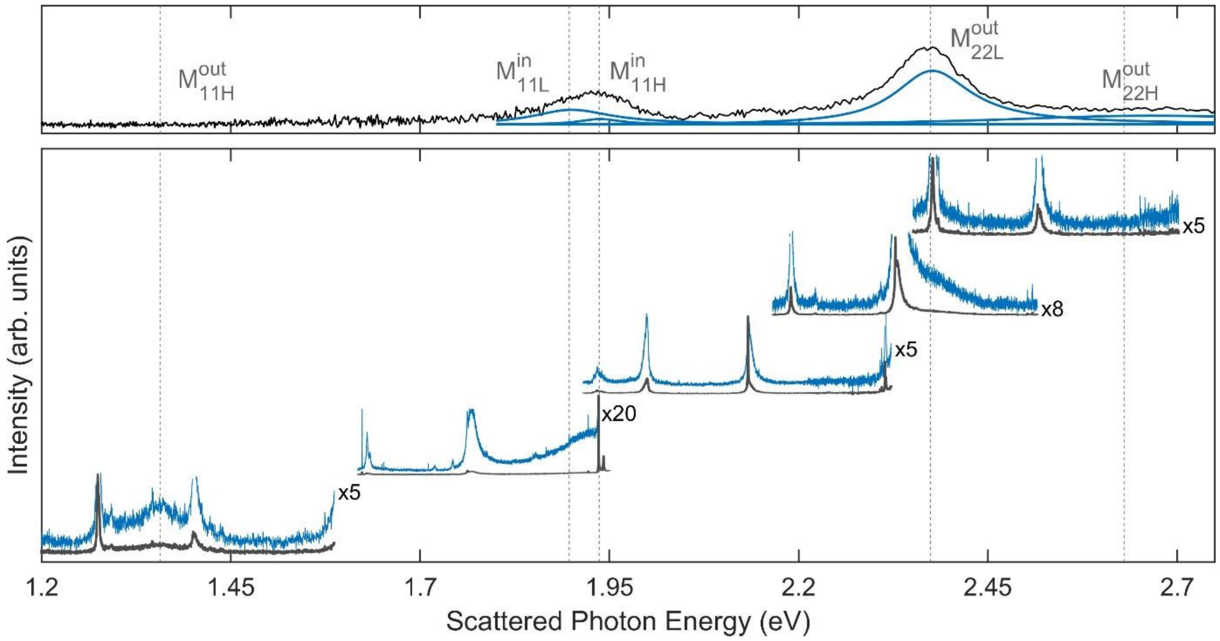

Figure S3.5. Comparison of Rayleigh spectrum (top) and wide-range Raman spectra (bottom) plotted as a function of scattered photon energy for (11,8)@(19,10) DWCNT.

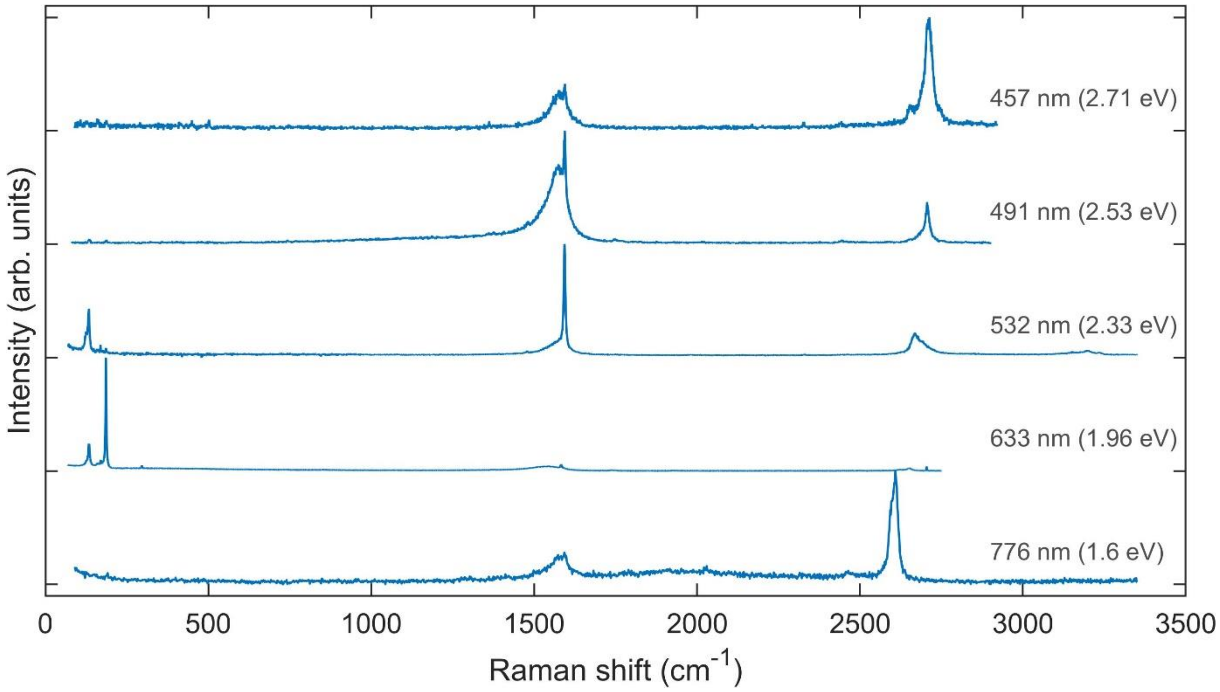

Figure S3.6. All wide-range Raman spectra for (11,8)@(19,10) DWCNT. Labels show the excitation wavelengths of the spectra.

DWCNT-4: **(14,8)@(19,14), M@SC**

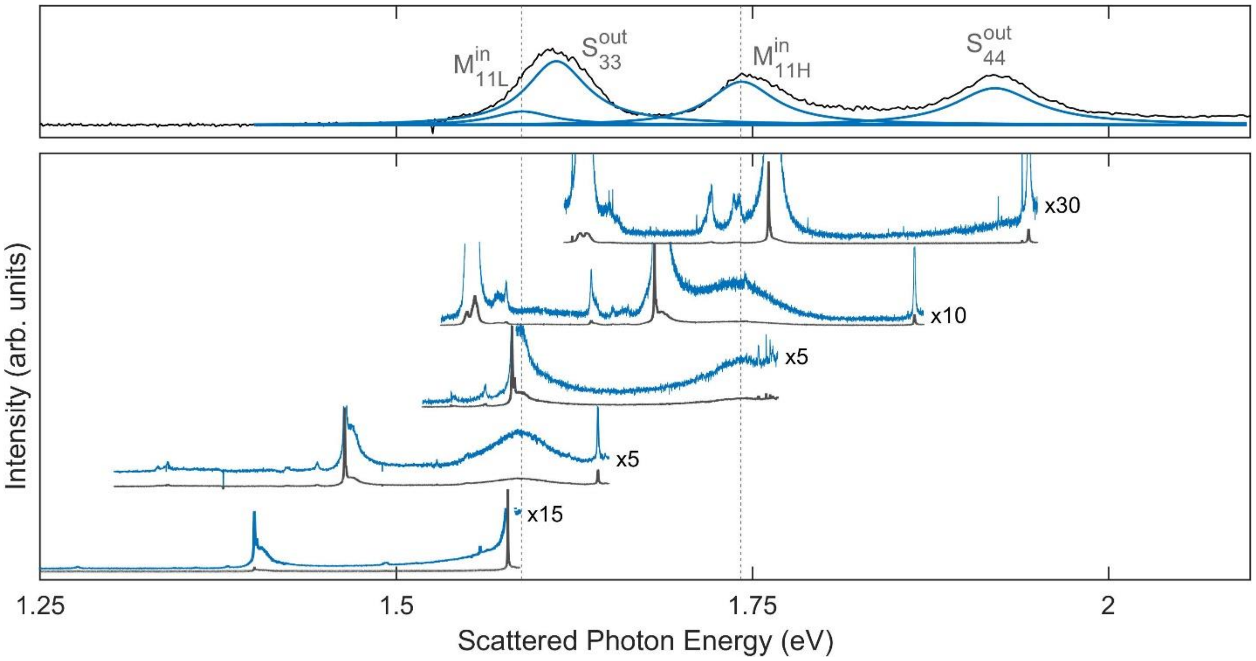

Figure S3.7. Comparison of Rayleigh spectrum (top) and wide-range Raman spectra (bottom) plotted as a function of scattered photon energy for (14,8)@(19,14) DWCNT.

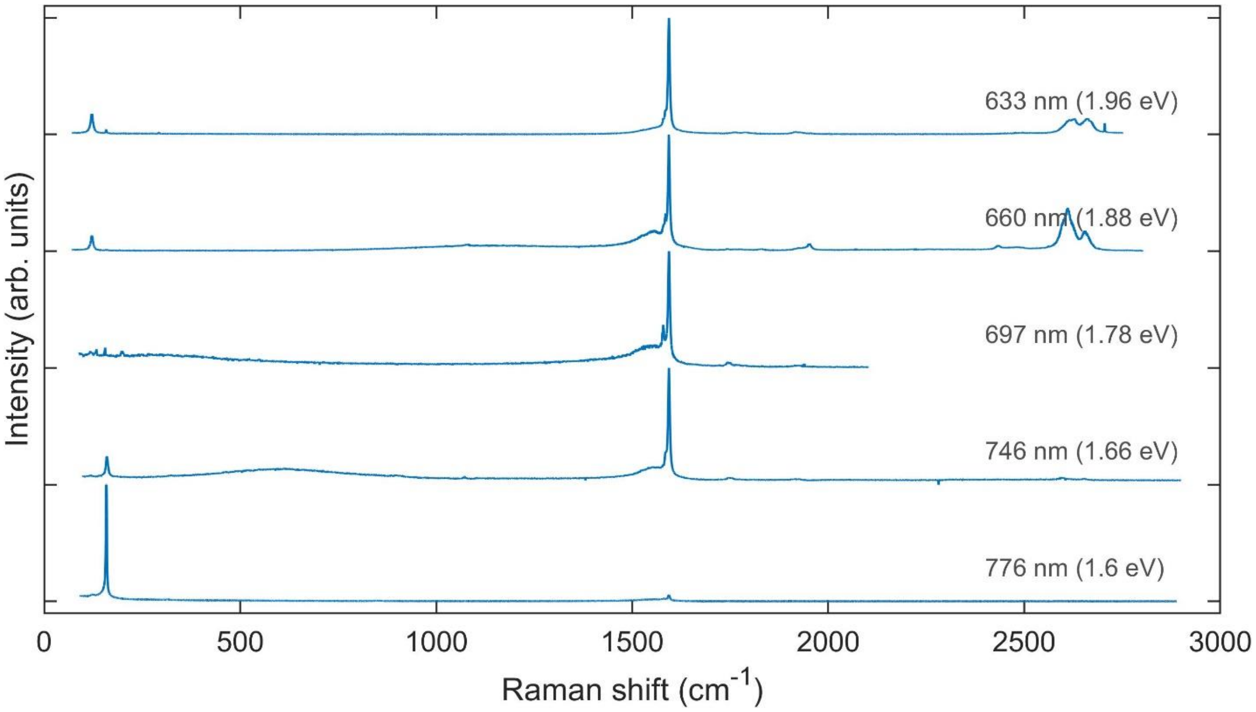

Figure S3.8. All wide-range Raman spectra for (14,8)@(19,14) DWCNT. Labels show the excitation wavelengths of the spectra.

DWCNT-5: **(14,5)@(26,1), M@SC**

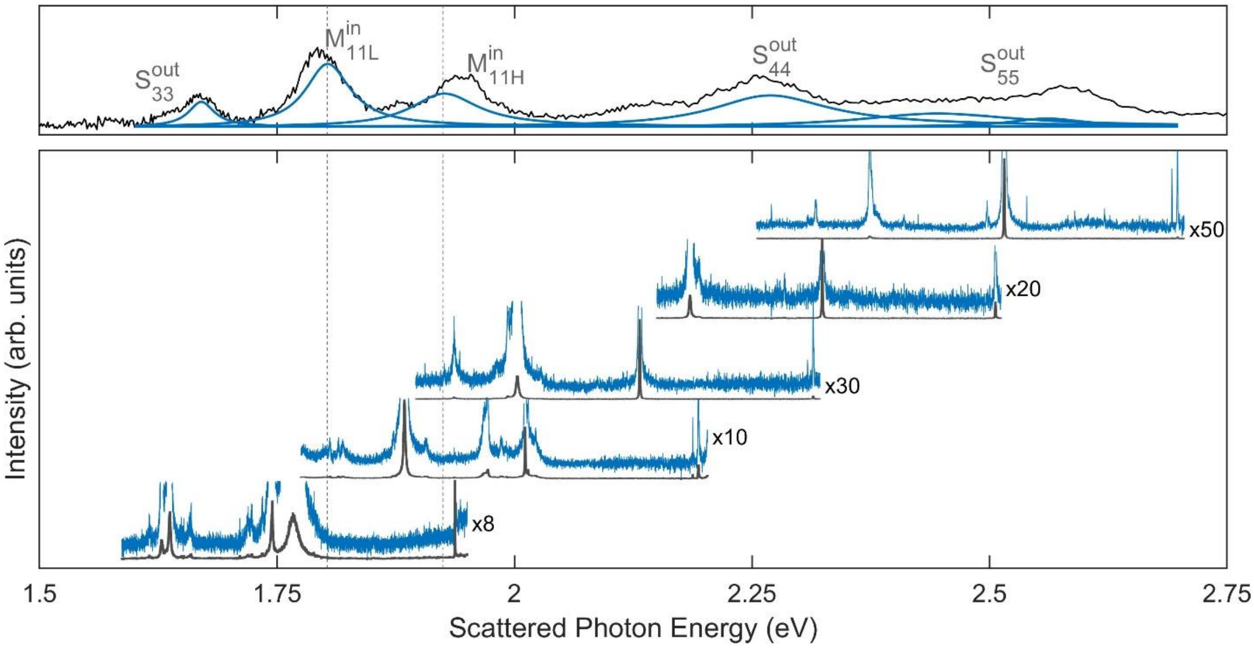

Figure S3.9. Comparison of Rayleigh spectrum (top) and wide-range Raman spectra (bottom) plotted as a function of scattered photon energy for (14,5)@(26,1) DWCNT.

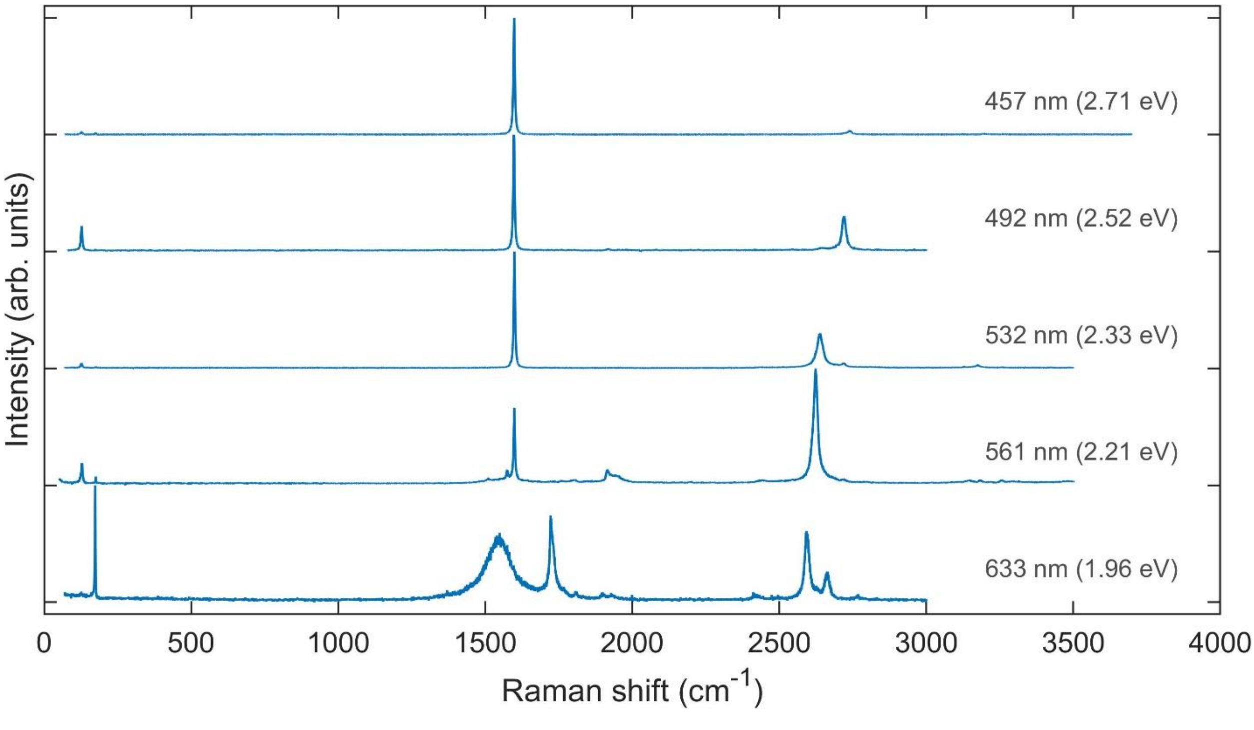

Figure S3.10. All wide-range Raman spectra for (14,5)@(26,1) DWCNT. Labels show the excitation wavelengths of the spectra.

DWCNT-6: **(18,2)@(19,13), SC@M**

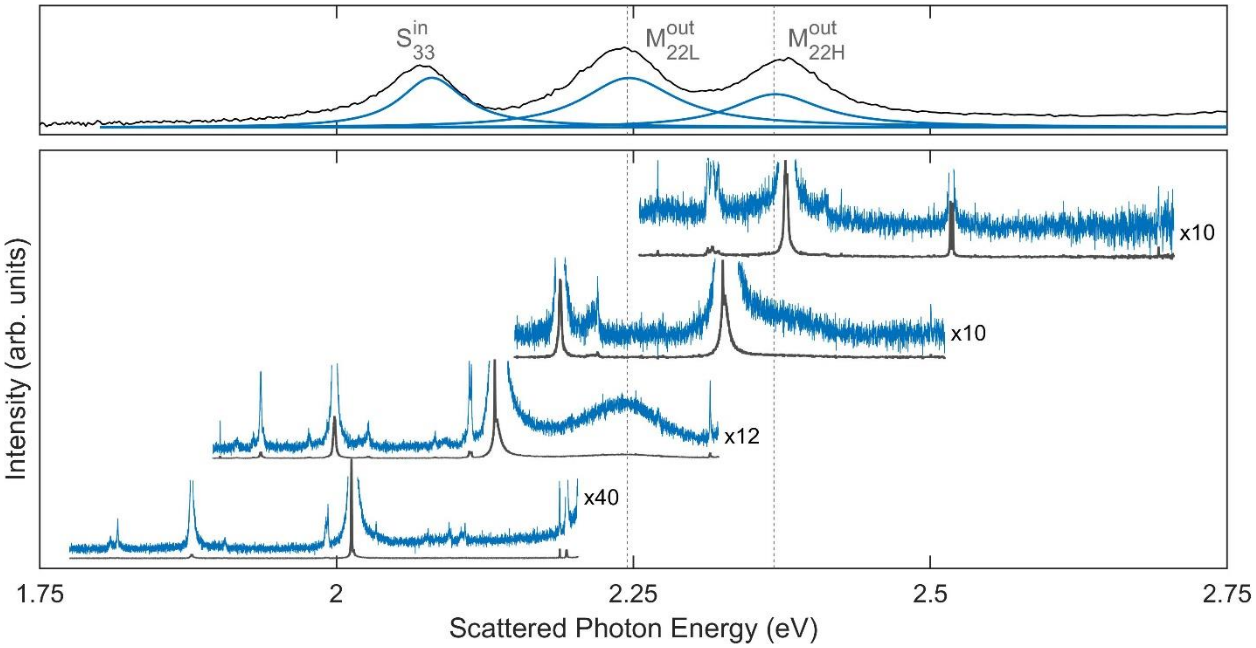

Figure S3.11. Comparison of Rayleigh spectrum (top) and wide-range Raman spectra (bottom) plotted as a function of scattered photon energy for (18,2)@(19,13) DWCNT.

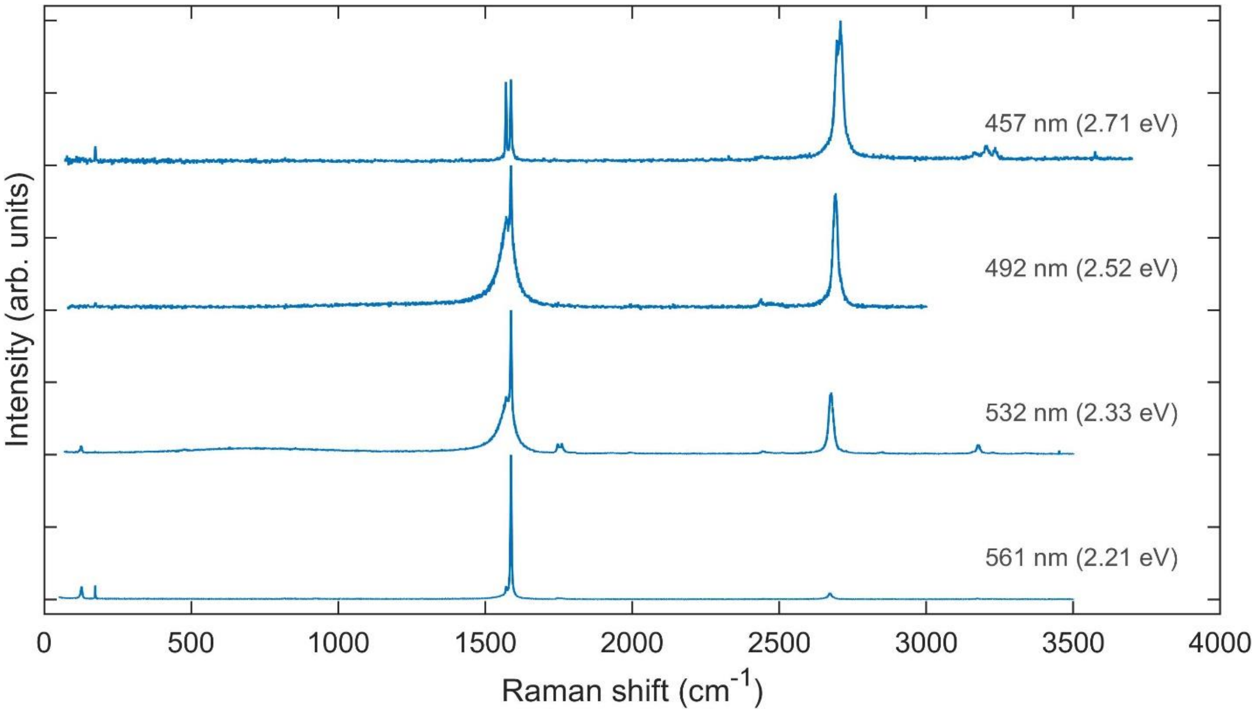

Figure S3.12. All wide-range Raman spectra for (18,2)@(19,13) DWCNT. Labels show the excitation wavelengths of the spectra.

DWCNT-7: **(18,6)@(21,14), M@SC**

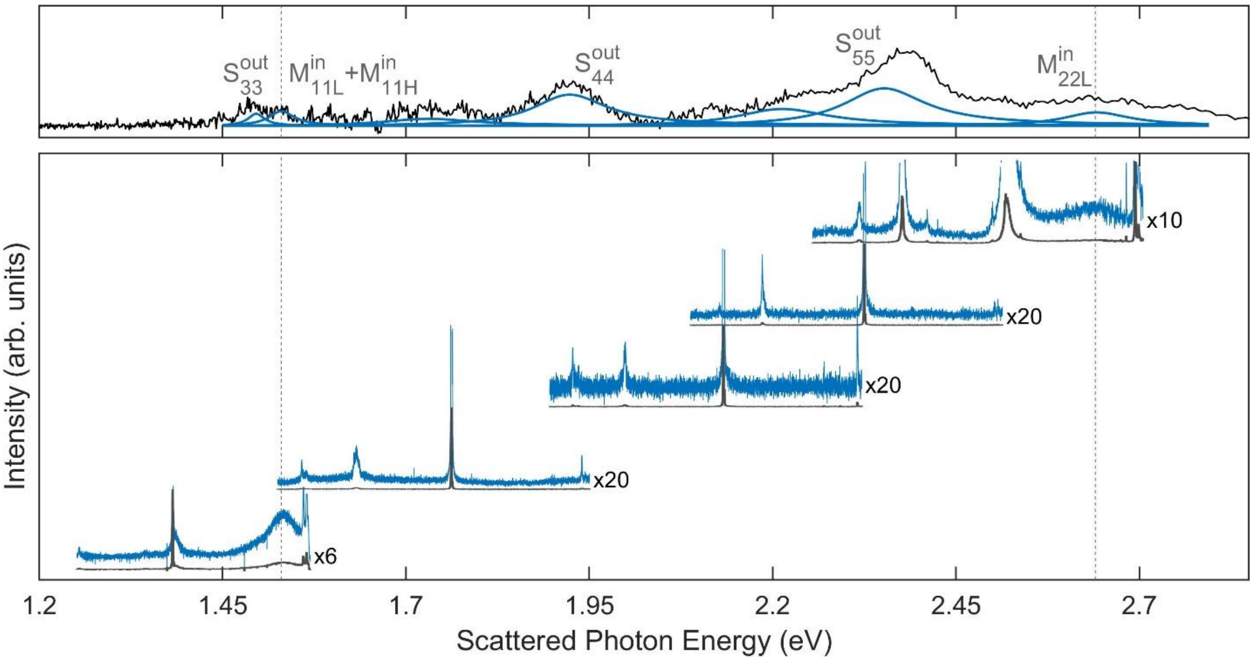

Figure S3.13. Comparison of Rayleigh spectrum (top) and wide-range Raman spectra (bottom) plotted as a function of scattered photon energy for (18,6)@(21,14) DWCNT.

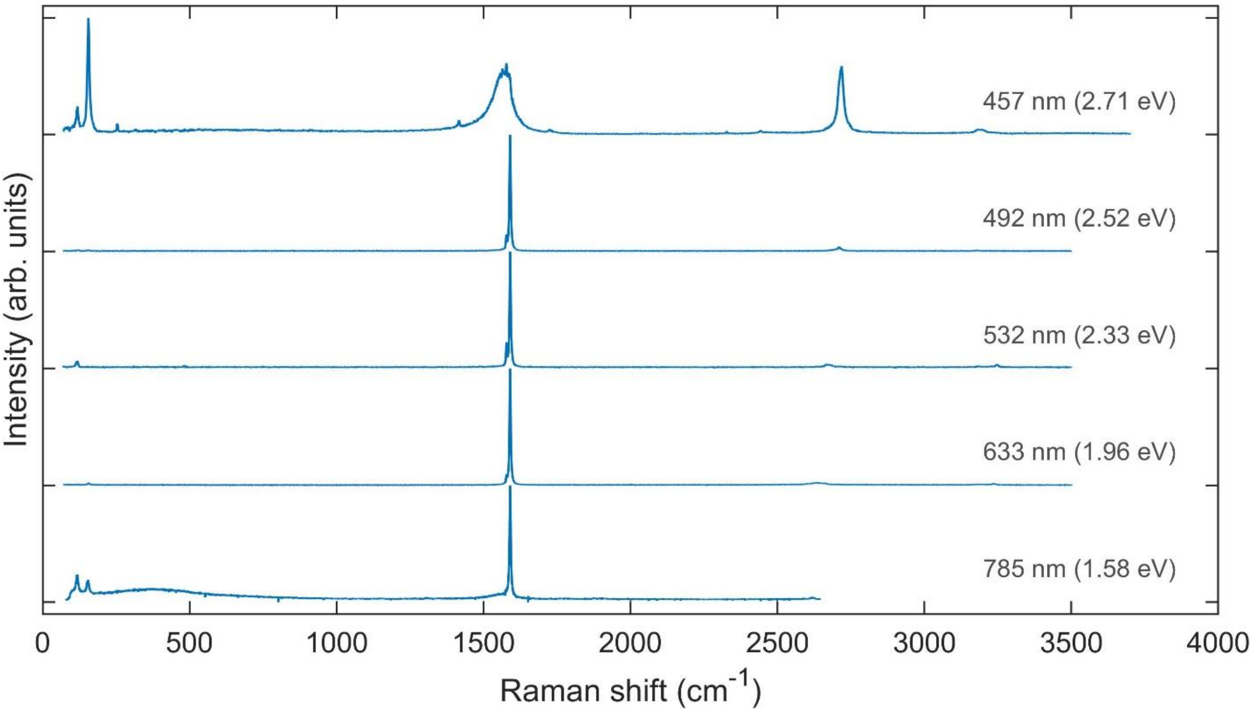

Figure S3.14. All wide-range Raman spectra for (18,6)@(21,14) DWCNT. Labels show the excitation wavelengths of the spectra.

DWCNT-8: **(22,13)@(39,2), M@SC**

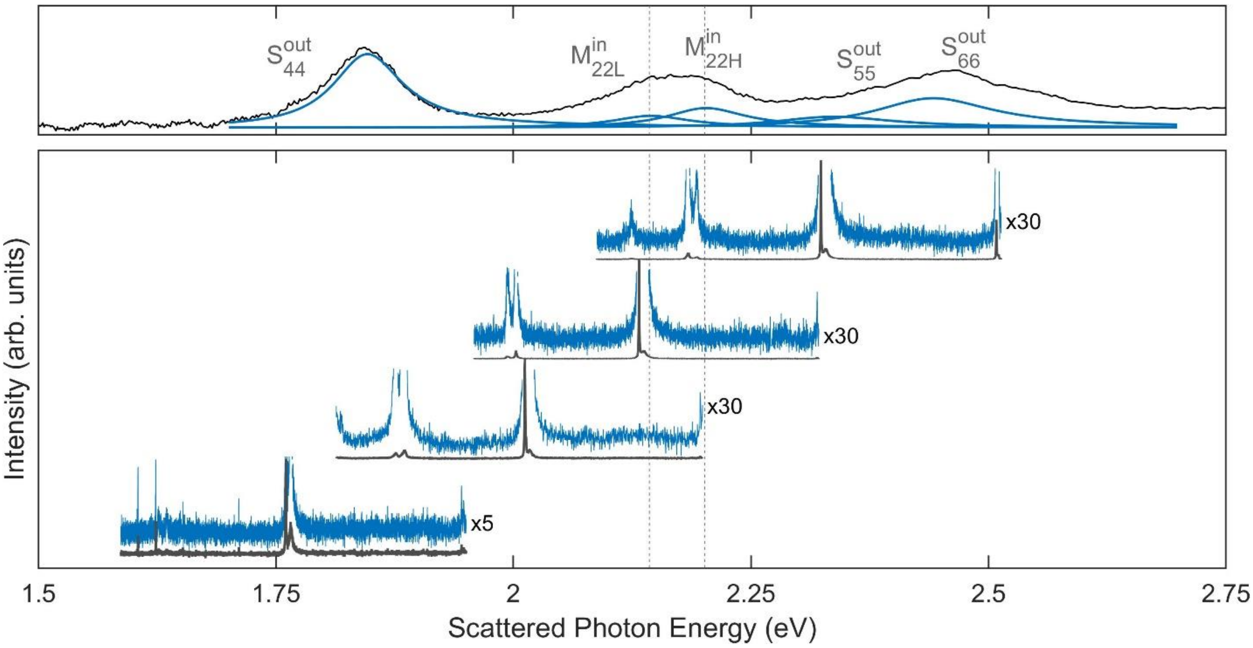

Figure S3.15. Comparison of Rayleigh spectrum (top) and wide-range Raman spectra (bottom) plotted as a function of scattered photon energy for (22,13)@(39,2) DWCNT.

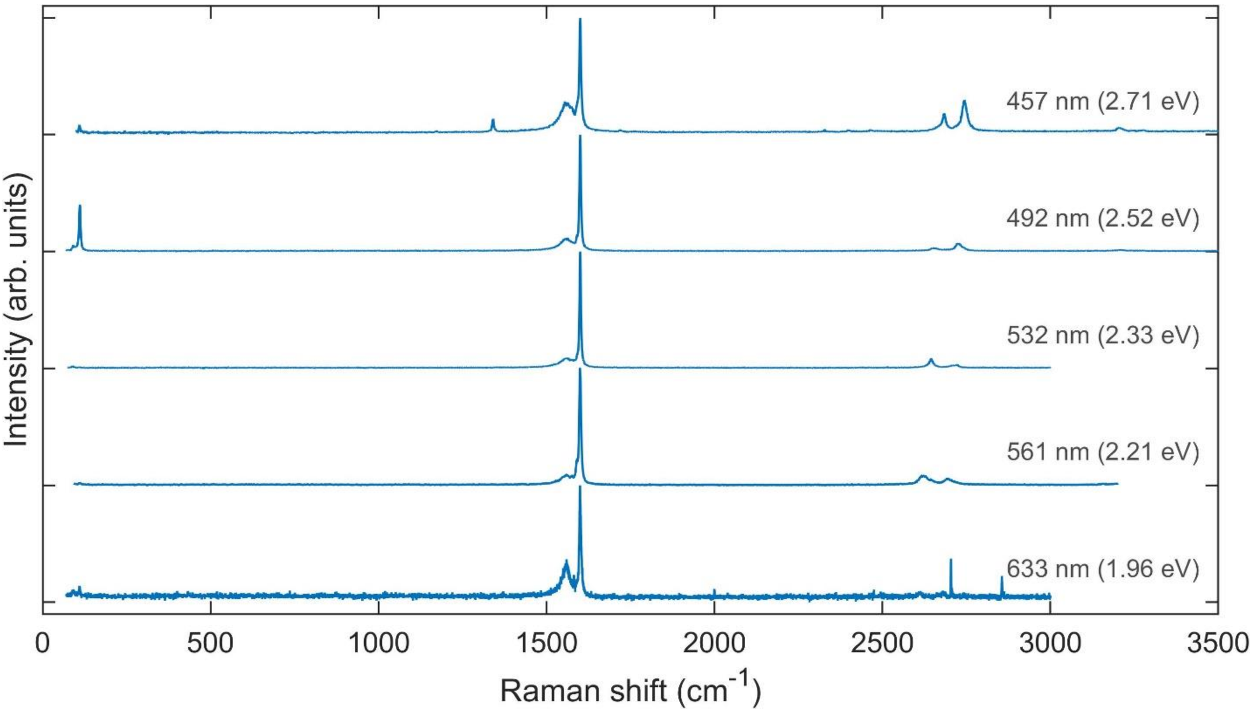

Figure S3.16. All wide-range Raman spectra for (22,13)@(39,2) DWCNT. Labels show the excitation wavelengths of the spectra.

DWCNT-9: **(17,14)@(26,14), M@M**

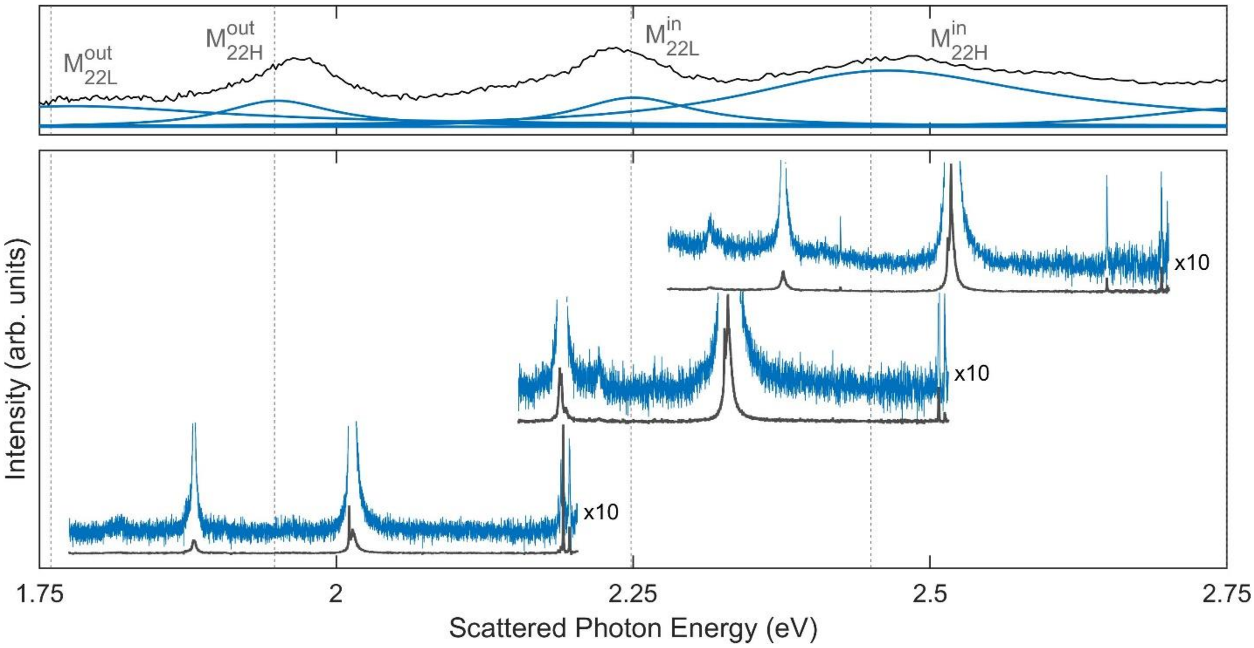

Figure S3.17. Comparison of Rayleigh spectrum (top) and wide-range Raman spectra (bottom) plotted as a function of scattered photon energy for (17,14)@(26,14) DWCNT.

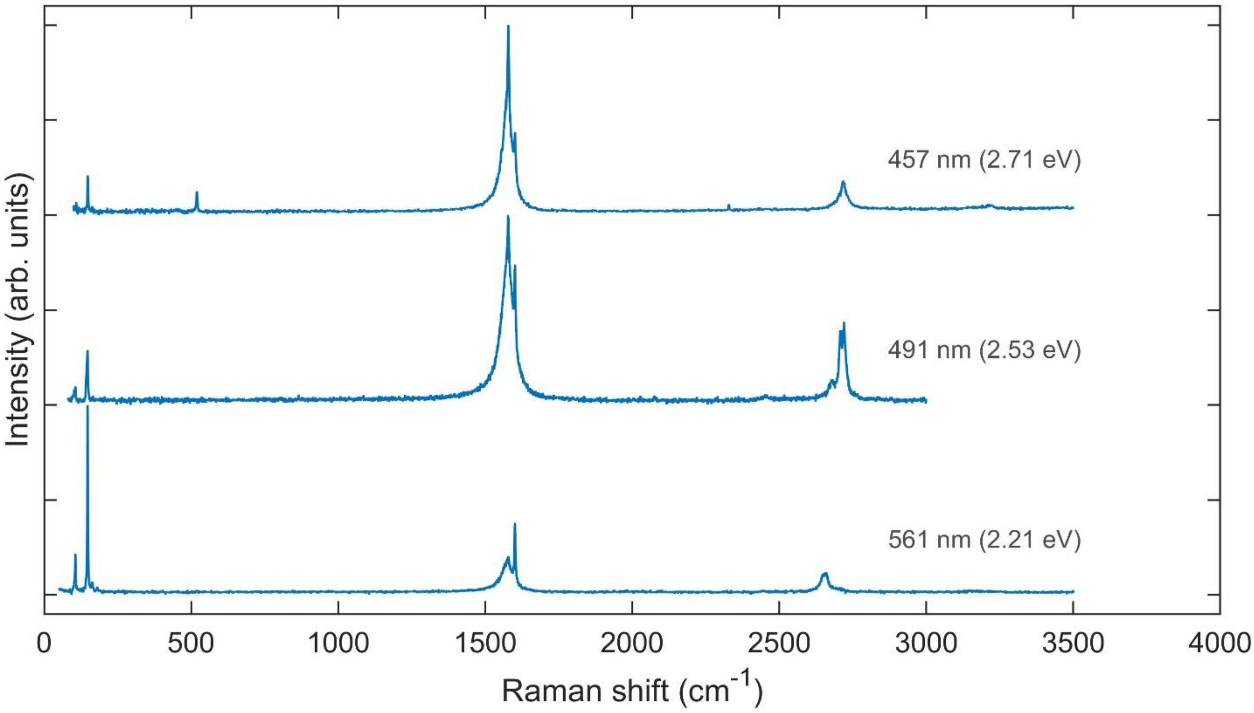

Figure S3.18. All wide-range Raman spectra for (17,14)@(26,14) DWCNT. Labels show the excitation wavelengths of the spectra.

DWCNT-10: **(17,14)@(28,12), M@SC**

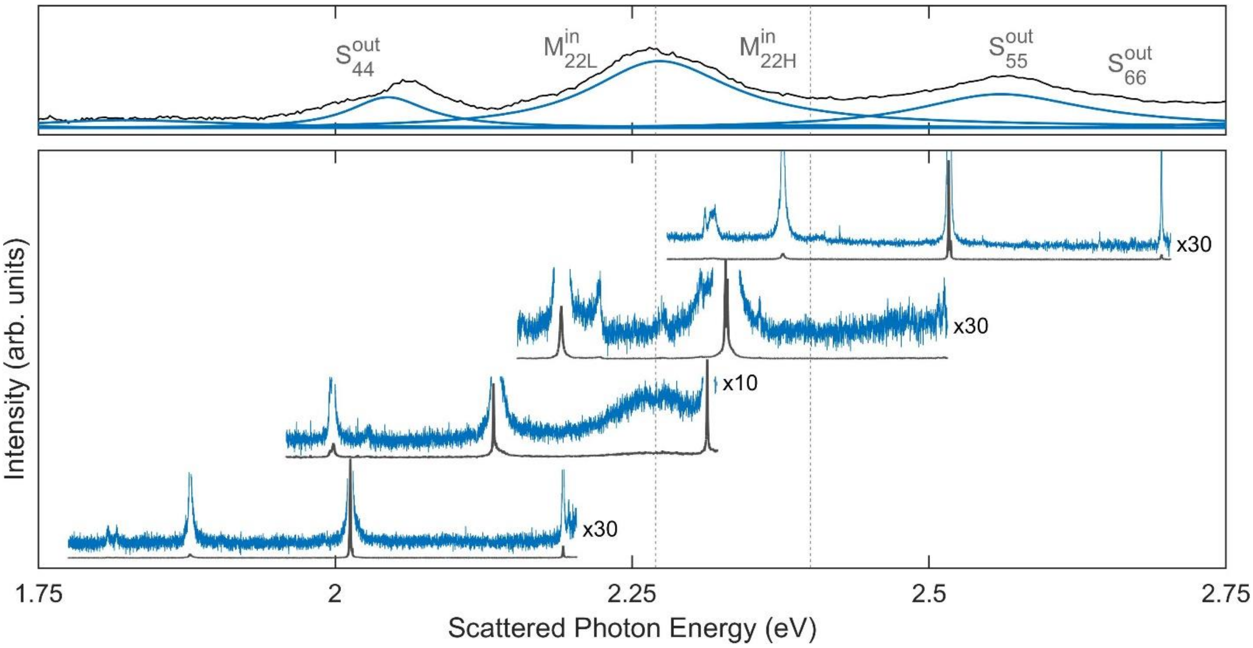

Figure S3.19. Comparison of Rayleigh spectrum (top) and wide-range Raman spectra (bottom) plotted as a function of scattered photon energy for (17,14)@(28,12) DWCNT.

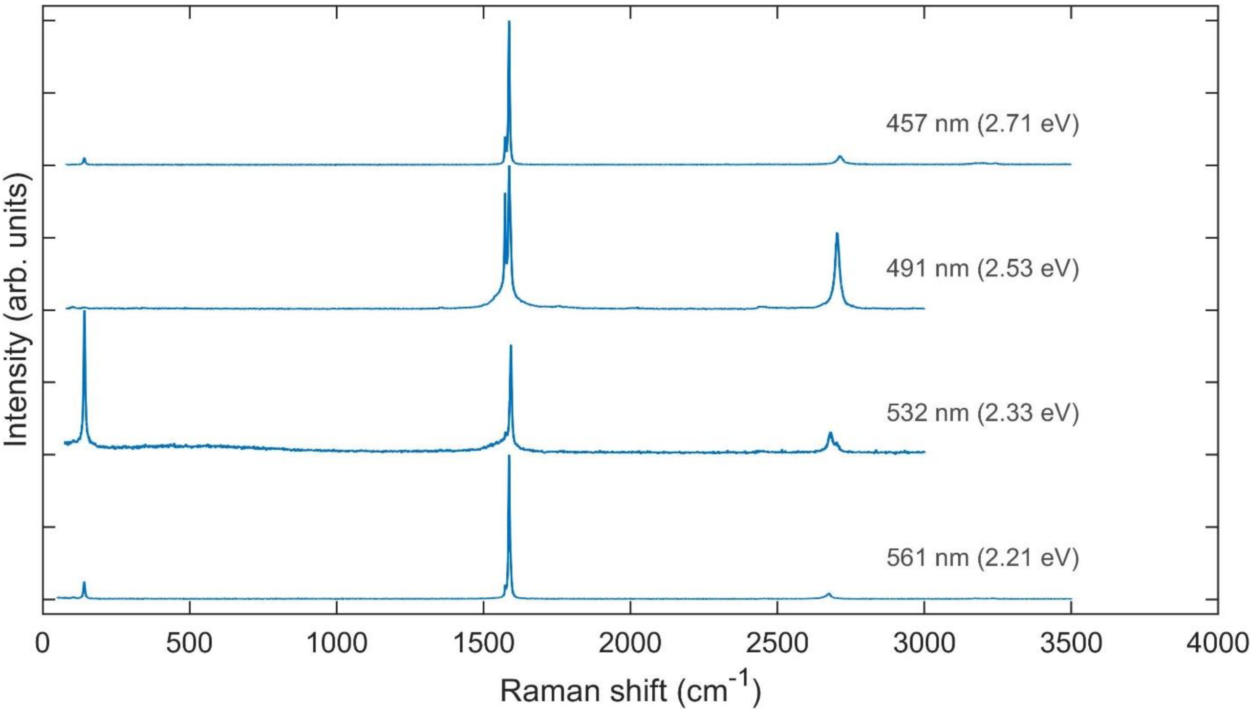

Figure S3.20. All wide-range Raman spectra for (17,14)@(28,12) DWCNT. Labels show the excitation wavelengths of the spectra.

DWCNT-11: **SC1@M**

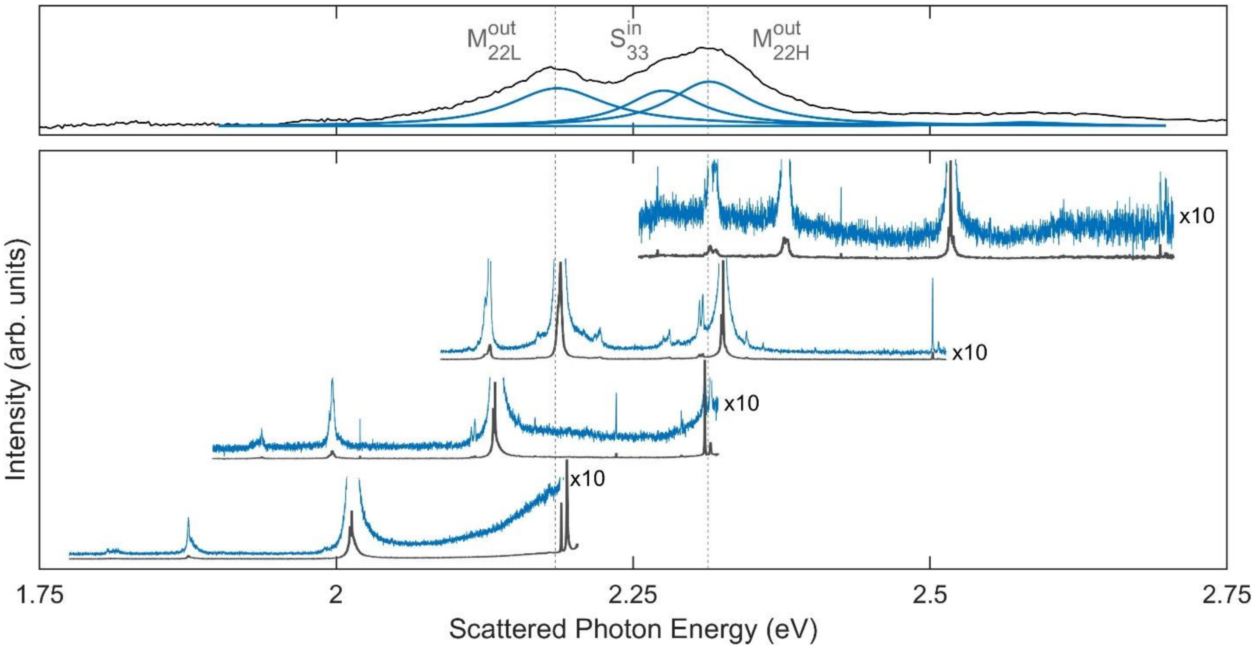

Figure S3.21. Comparison of Rayleigh spectrum (top) and wide-range Raman spectra (bottom) plotted as a function of scattered photon energy for DWCNT-11.

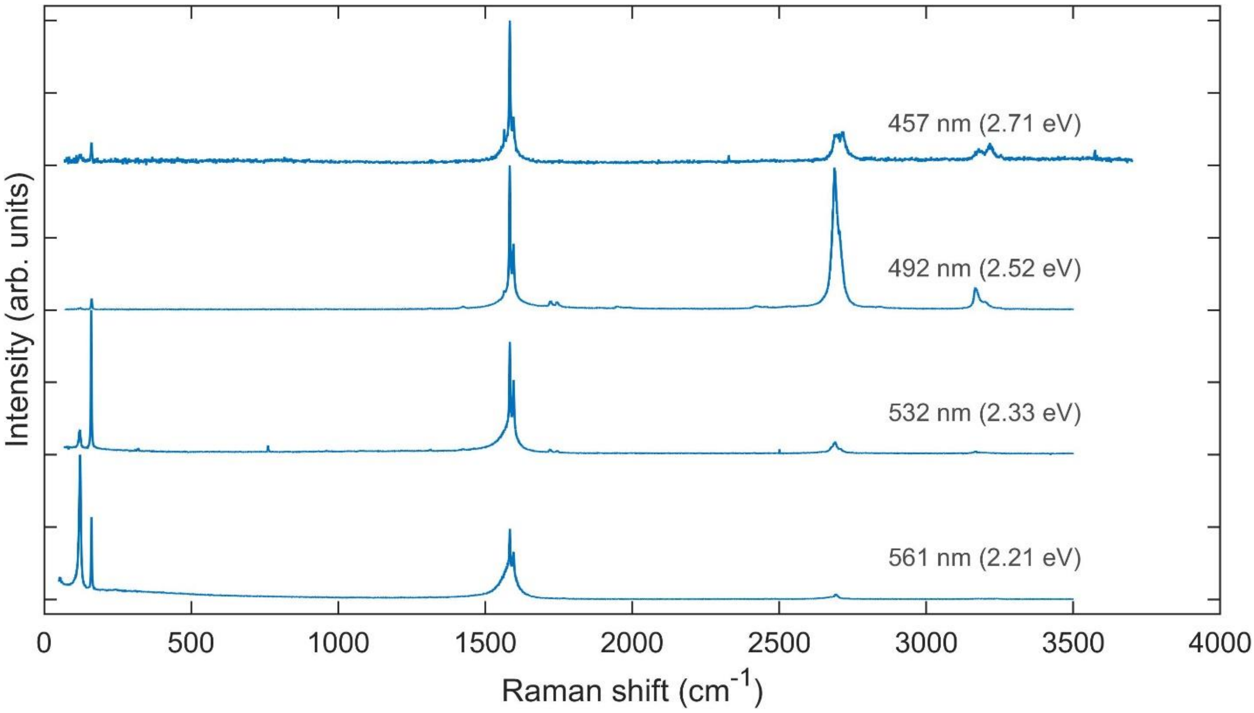

Figure S3.22. All wide-range Raman spectra for DWCNT-11. Labels show the excitation wavelengths of the spectra.

DWCNT-12: **M@SC**

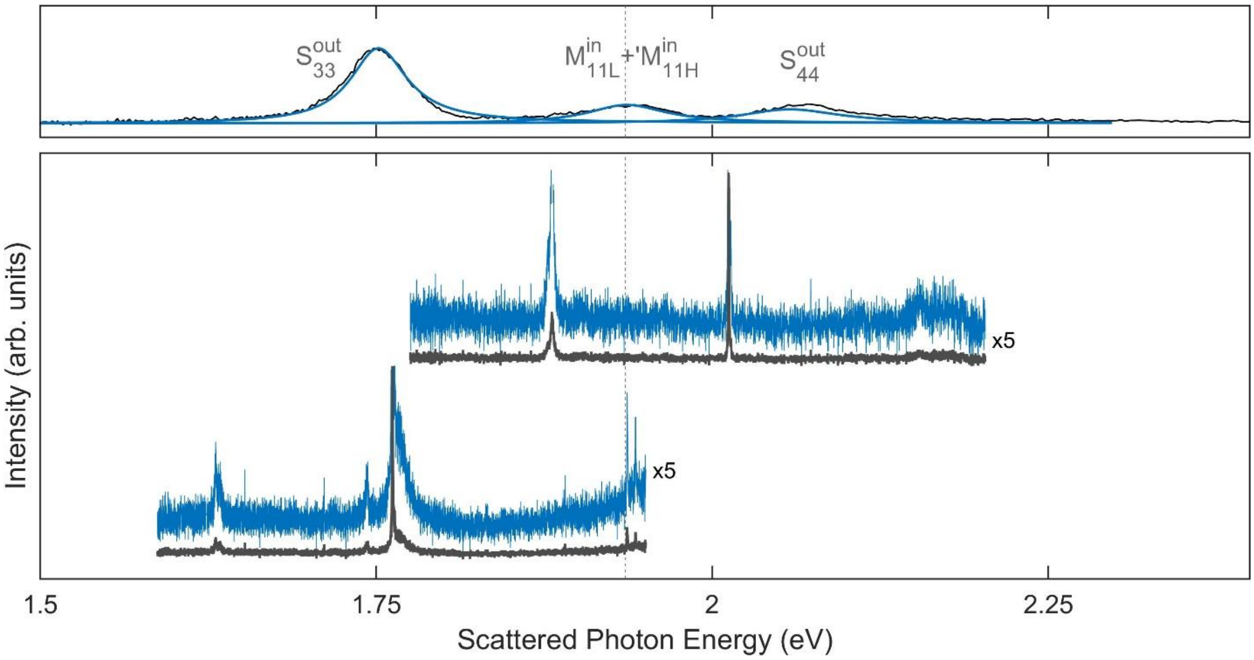

Figure S3.23. Comparison of Rayleigh spectrum (top) and wide-range Raman spectra (bottom) plotted as a function of scattered photon energy for DWCNT-12.

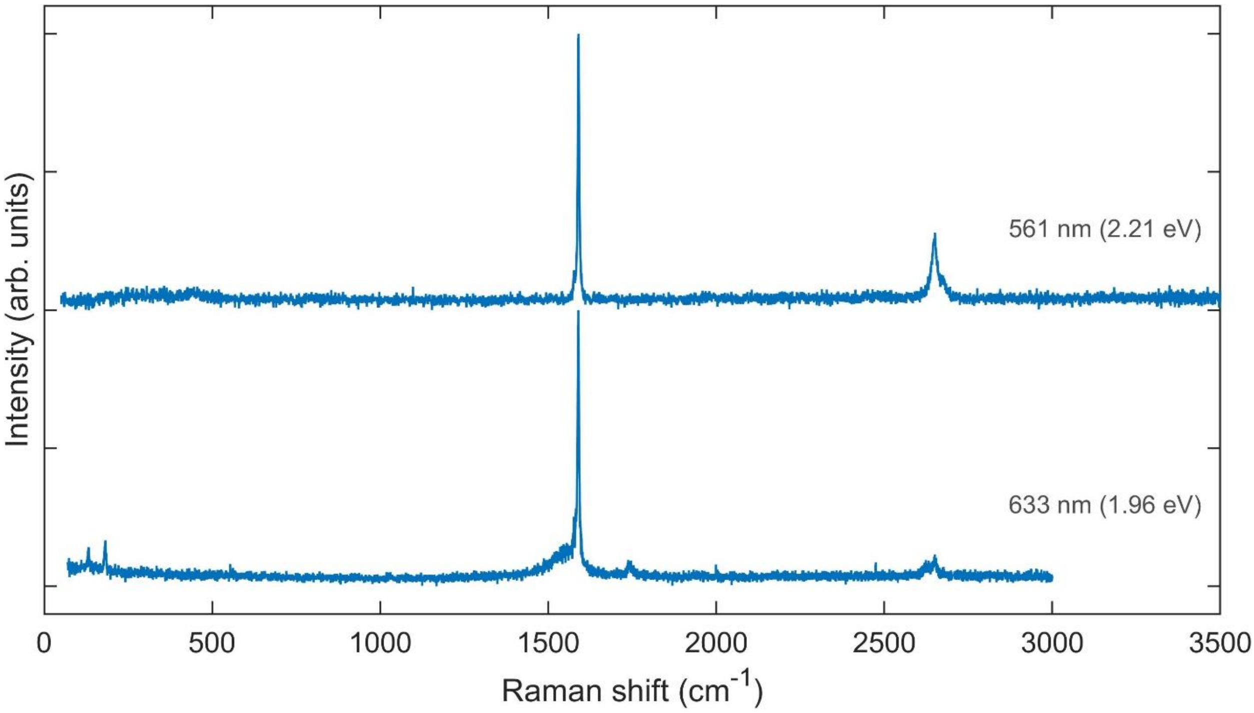

Figure S3.24. All wide-range Raman spectra for DWCNT-12. Labels show the excitation wavelengths of the spectra.

DWCNT-13: **SC@M**

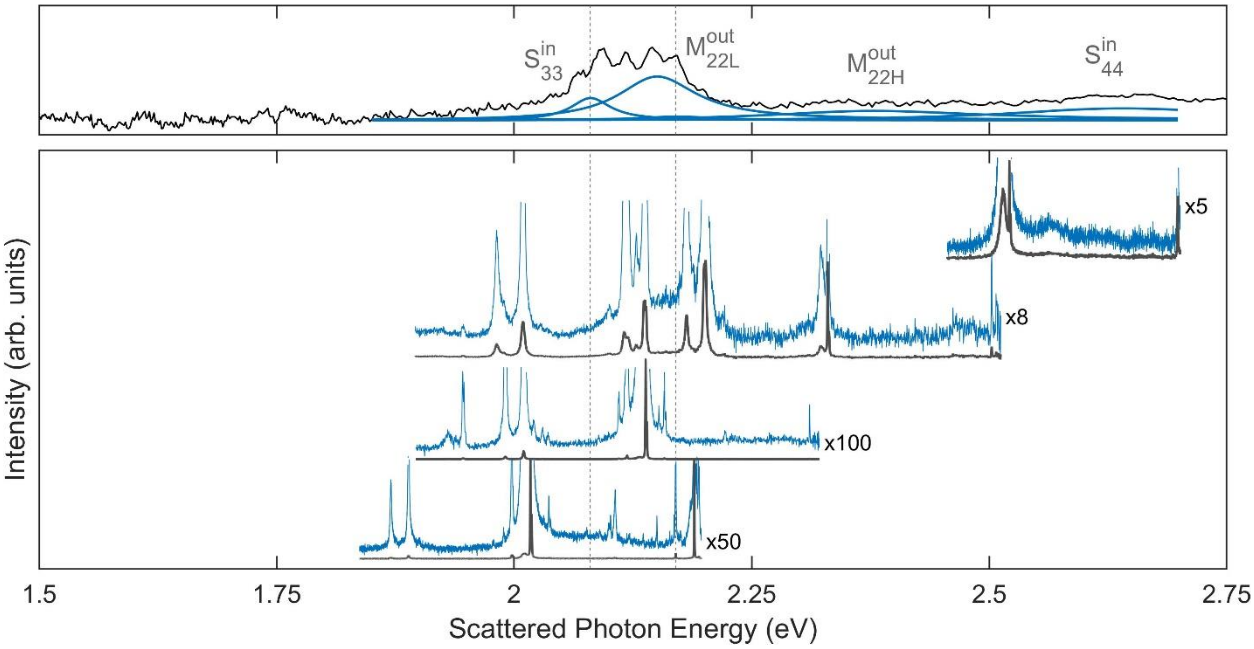

Figure S3.25. Comparison of Rayleigh spectrum (top) and wide-range Raman spectra (bottom) plotted as a function of scattered photon energy for DWCNT-13.

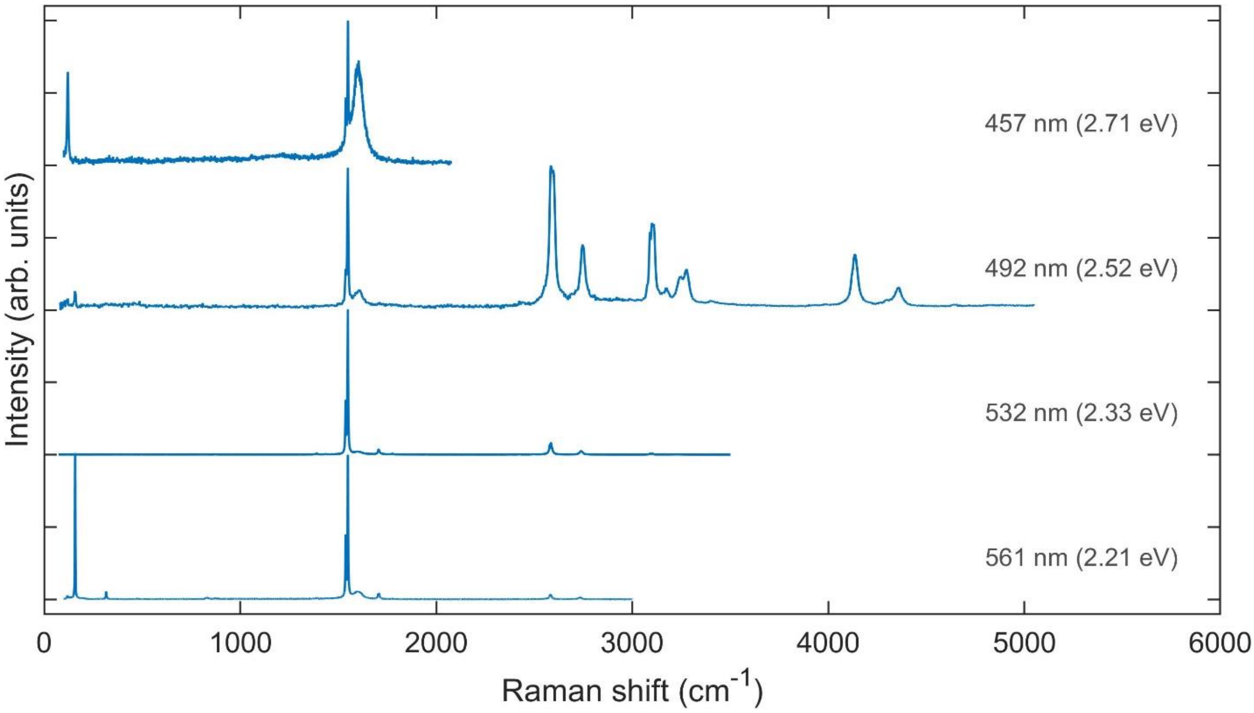

Figure S3.26. All wide-range Raman spectra for DWCNT-13. Labels show the excitation wavelengths of the spectra. The sharp peaks between 2500 and 4500 cm^{-1} in the Raman spectra measured at 492 nm correspond to the multi-phonon Raman lines[9].

DWCNT-14: **SC@M**

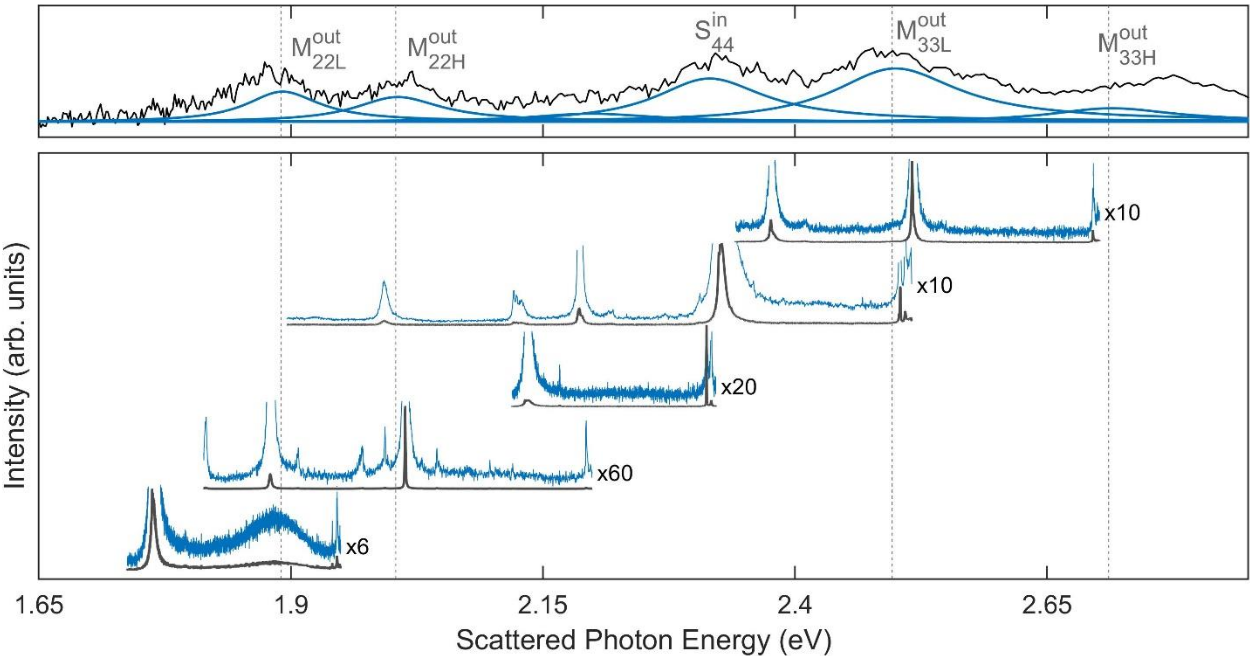

Figure S3.27. Comparison of Rayleigh spectrum (top) and wide-range Raman spectra (bottom) plotted as a function of scattered photon energy for DWCNT-14.

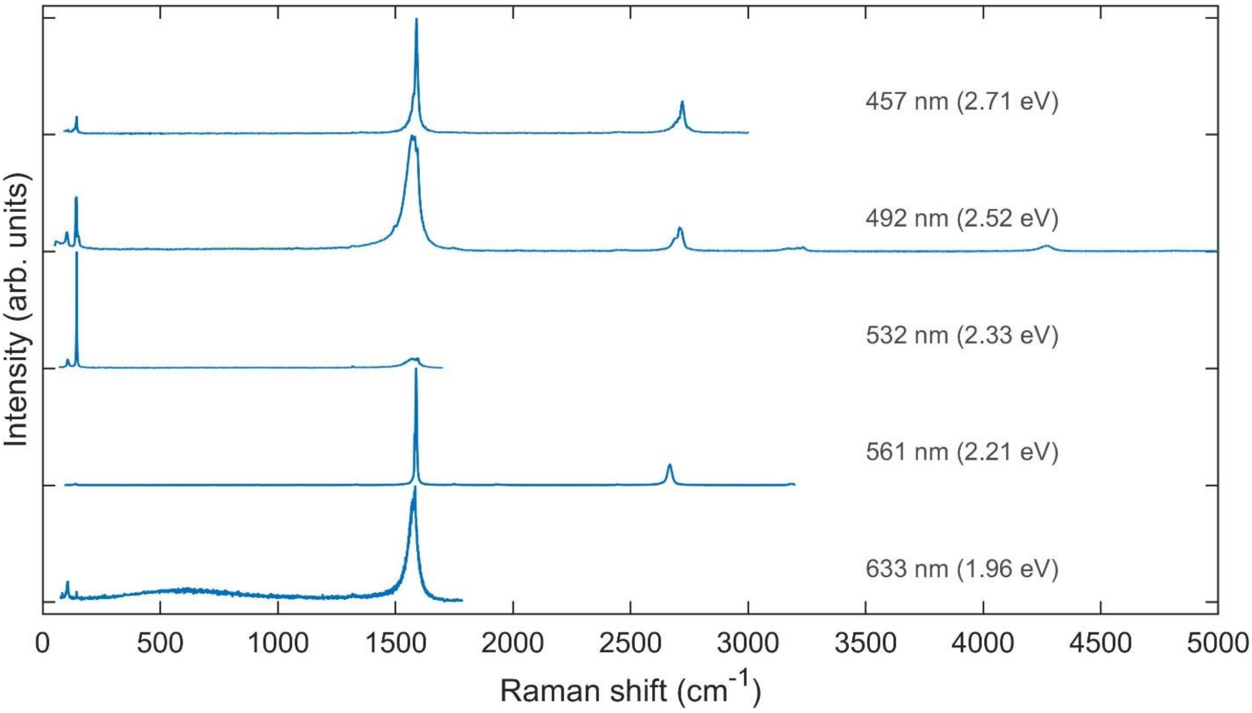

Figure S3.28. All wide-range Raman spectra for DWCNT-14. Labels show the excitation wavelengths of the spectra.

DWCNT-15: **(11,6)@(18,9), SC@M**

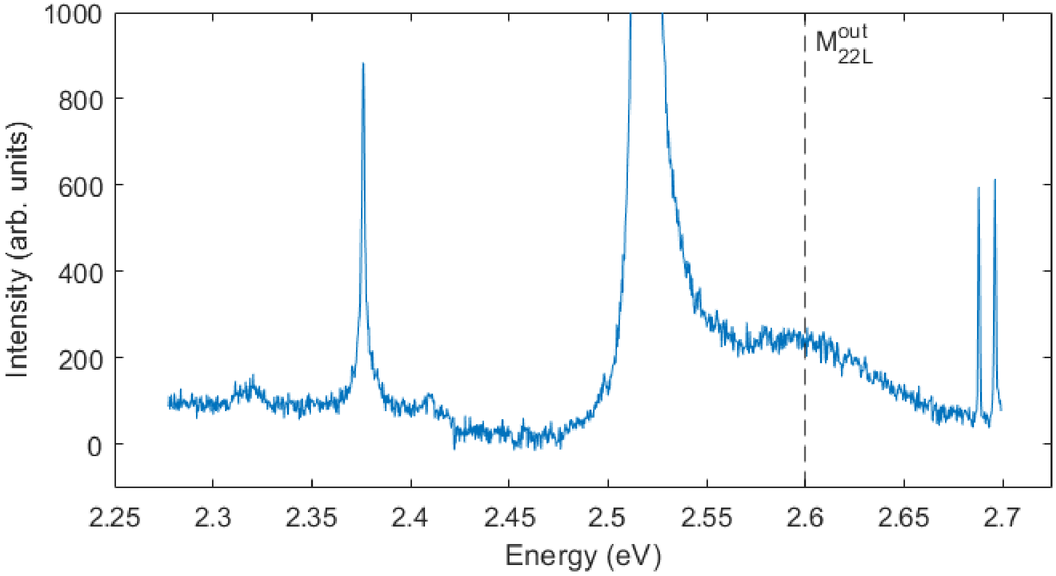

Figure S3.29. The wide-range Raman spectrum plotted as a function of scattered photon energy for DWCNT-15. The vertical dashed line represent the energy of the M_{22L} of the DWCNT outer layer obtained from the fit of absorption spectrum in Ref. [8] (see Table 4.10).

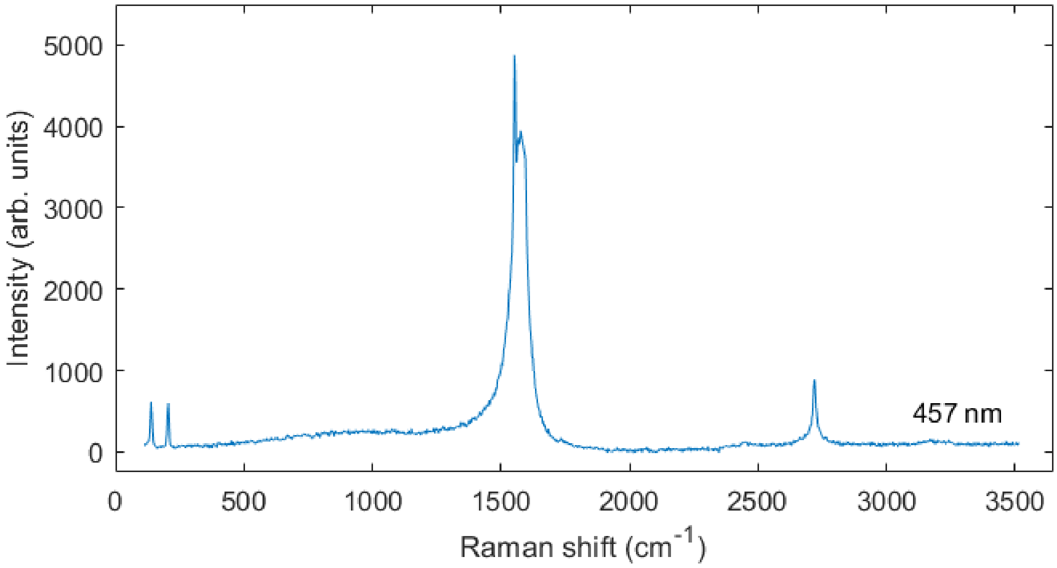

Figure S3.30. The wide-range Raman spectrum for DWCNT-15. The label shows the excitation wavelength.

Section S4. Complete set of tunable Raman spectra and results of absorption spectrum calculations for DWCNTs (14,1)@(15,12) and (18,6)@(21,14)

DWCNT-1: **(14,1)@(15,12), SC@M**

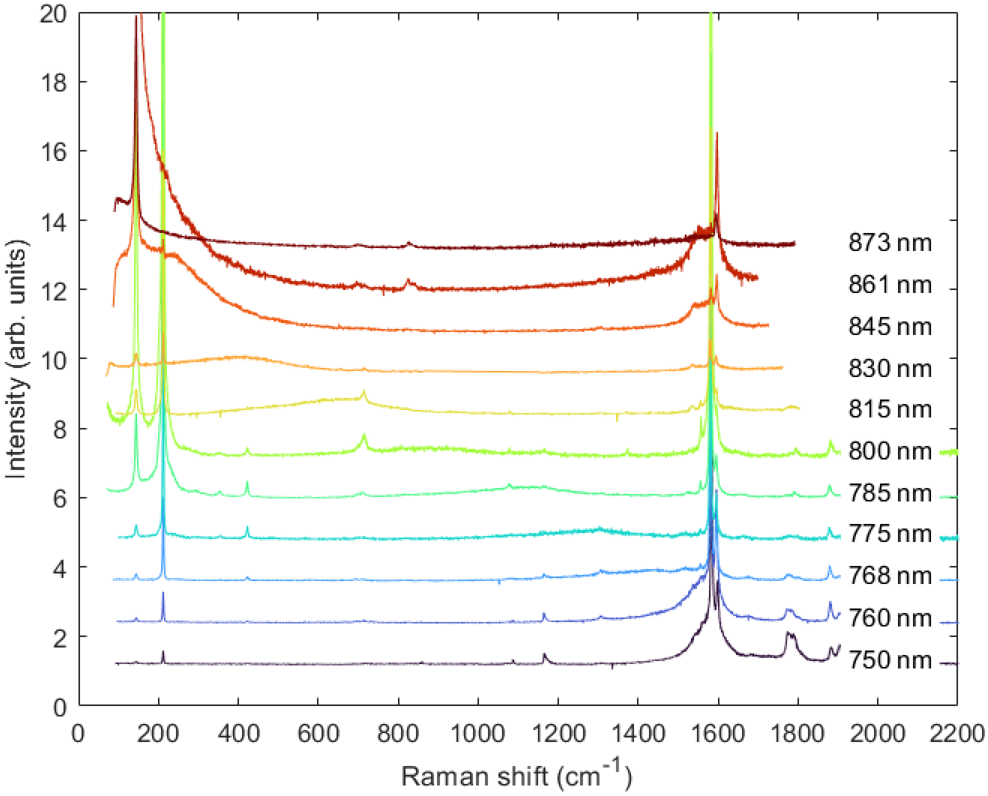

Figure S4.1. Raman spectra of DWCNT-1 (14,1)@(15,12) with ERS features measured in the range 750 – 873 nm. These spectra are shown in the form of the REM in Figure 3a.

Table S4.1. Optical transition energies for DWCNT-1 (14,1)@(15,12) with equal and opposite handedness calculated within an ab initio-based NTB approach [10]. The energy values are given in eV and represent the raw NTB data from the recursion method, *i.e.*, no upshift is applied and no dielectric downshift is added.

(14,1)@(15,12) SC1@M	**In**	$\mathbf{S_{11}^{in}}$	$\mathbf{S_{22}^{in}}$	$\mathbf{S_{33}^{in}}$	$\mathbf{S_{44}^{in}}$
	SWCNT	0.61	1.32	2.18	-
	DW(1)	0.62	1.27	2.09	-
	DW(−1)	0.62	1.27	2.13	
	Out	$\mathbf{M_{11L}^{out}}$	$\mathbf{M_{11H}^{out}}$	$\mathbf{M_{22L}^{out}}$	$\mathbf{M_{22H}^{out}}$
	SWCNT	1.17	1.21	2.25	2.32
	DW(1)	1.19	1.21	2.26	2.58
	DW(−1)	1.18	1.19	2.26	2.32

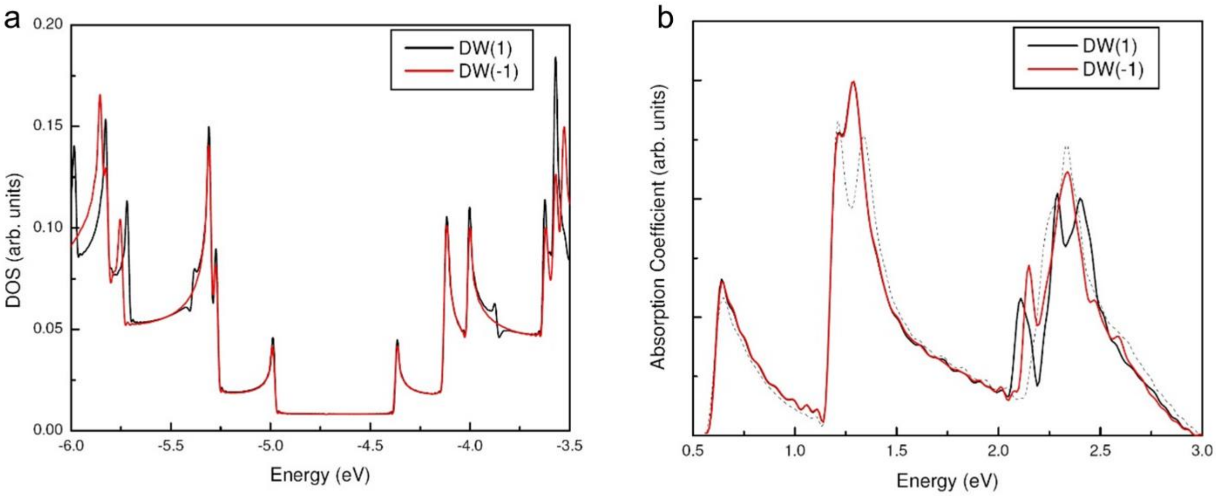

Figure S4.2 (a) Electronic DOS and (b) absorption coefficient of DWCNT-1 (14,1)@(15,12) with equal (DW(1), black line) and opposite (DW(-1), red line) handedness calculated within an *ab initio*-based NTB approach [10]. The dotted line in (b) represents the weighted sum of absorption coefficients of DWCNT layers in the absence of van der Waals interactions. The transition energies are summarized in Table S4.1.

On the transition energy assignment of (14,1)@(15,12) DWCNT

In our previous work on the detection of PL from individual DWCNTs [5], we assigned two peaks at ~1.44 and ~1.54 eV in the Rayleigh spectrum of (14,1)@(15,12) DWCNT (*e.g.*, Figure 1b in the main text) to M_{11L} and M_{11H} + S_{22} transitions, respectively. The main arguments for this assignment were as follows:

i) the RBM REP of the (15,12) layer has two maxima at ~1.44 and ~1.54 eV (Figure S4.3, upper panels) which may originate from M_{11L} and M_{11H} transitions, given their energies for non-interacting layers are expected at 1.47 and 1.5 eV, respectively (see Table S2.1);

ii) the best fit of the TO REP of the (15,12) layer can be obtained only when M_{11L} and M_{11H} transitions are well separated (compare bottom panels in Figure S4.3a,b).

However, new absorption spectrum calculations (Table S4.1) suggest an alternative assignment: M_{11L} and M_{11H} transitions of the outer (15,12) layer are overlapping at 1.44 eV, while the peak at 1.54 eV is solely due to the S_{22} transition. This interpretation can be supported by previous studies on isolated metallic SWCNTs [11] which established that the value of $|M_{iiH} - M_{iiL}|$ is least sensitive to environmental interaction. As a first approximation, it may be true also for the interlayer interactions in DWCNTs at least in what concerns the dielectric screening effect. Therefore, considering the transition energies of air-suspended (15,12) SWCNT (Table S2.1), we obtain $M_{11H} - M_{11L} = 0.032$ eV. Given the experimental error, we should expect M_{11H} in the DWCNT-1 at 1.47~1.50 eV. Combined with the fact that the intensity of M_{11H} should be much lower than M_{11L}, the former can correspond to the side peak of the 1.44 eV peak. In this interpretation, the appearance of the second maxima in the RBM REP at ~1.54 eV (Figure S4.3, upper panels) can be due to the mechanical coupling of inner and outer layers as previously reported for DWCNTs [12,13]. The behavior of the TO REP of the (15,12) layer is more difficult to understand but can also be related to the coupling between the layers.

In summary, we carefully considered all arguments in favor of both interpretations, but at this moment we cannot discriminate unambiguously between them. Therefore, we marked the possibility of two assignments with asterisks in Figure 1b, Figure 2a, and Figure 3b. We note that considering one or the other doesn't change the conclusions drawn here or in Ref. [5].

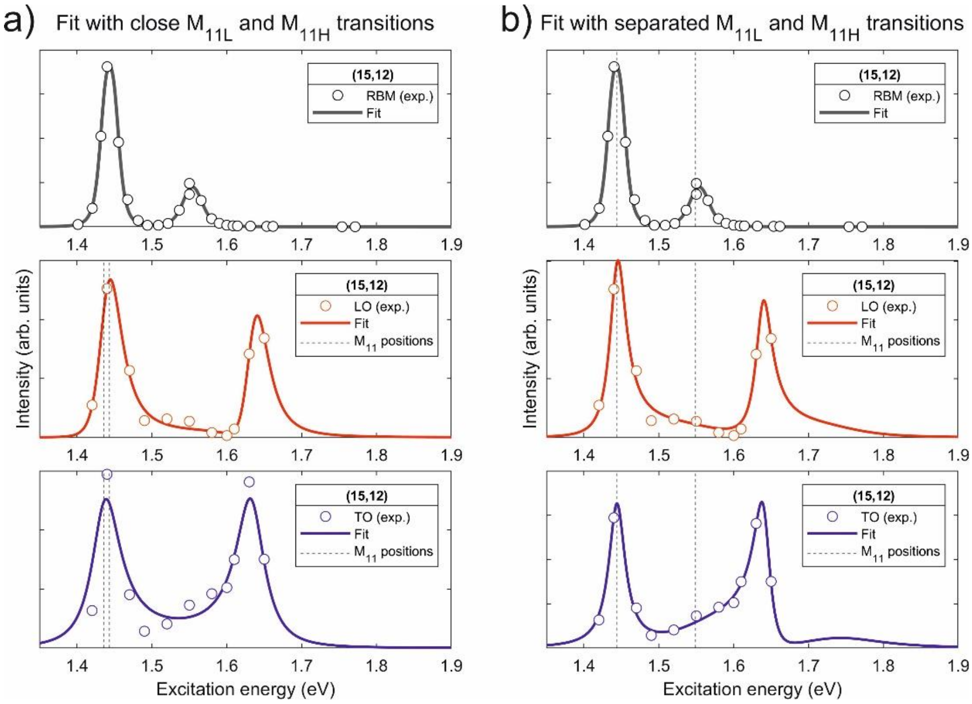

Figure S4.3. REPs of RBM, LO- and TO-modes for (15,12) layer of the DWCNT-1 (14,1)@(15,12). The fit of the LO and TO REPs with (a) two close M_{11L} and M_{11H} transitions and (b) two separated M_{11L} and M_{11H} transitions.

DWCNT-7: **(18,6)@(21,14), M@SC**

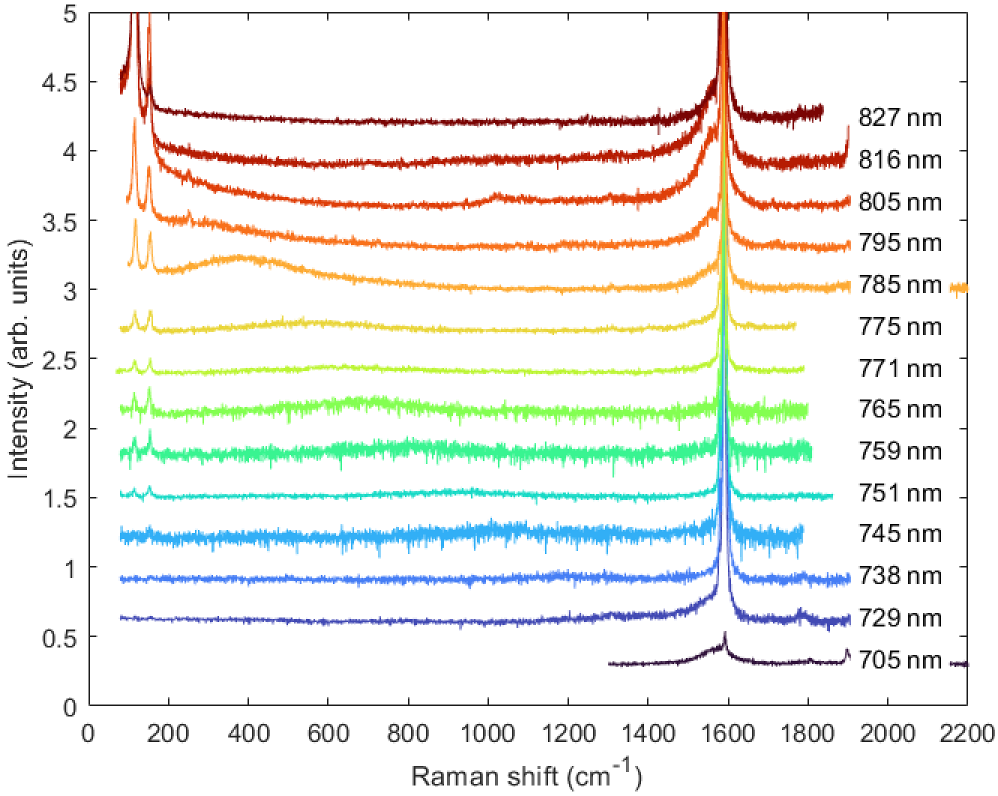

Figure S4.4. Raman spectra of DWCNT-7 (18,6)@(21,14) with ERS features measured in the range 705 – 816 nm. These spectra are shown in the form of the REM in Figure 3c.

Table S4.2. Optical transition energies for DWCNT-7 (18,6)@(21,14) with equal and opposite handedness calculated within ab initio-based NTB approach [10]. The energy values are given in eV and represent the raw NTB data from the recursion method, *i.e.*, no upshift is applied and no dielectric downshift is added.

(18,6)@(21,14) M@SC1	**In**	$\mathbf{M}_{\mathbf{11L}}^{in}$	$\mathbf{M}_{\mathbf{11H}}^{in}$	$\mathbf{M}_{\mathbf{22L}}^{in}$	$\mathbf{M}_{\mathbf{22H}}^{in}$	$\mathbf{M}_{\mathbf{33L}}^{in}$	$\mathbf{M}_{\mathbf{33H}}^{in}$	**-**
	SWCNT	1.23	1.33	2.30	2.67			
	DW(1)	1.19	1.32	2.31	2.55	-	-	-
	DW(-1)	1.21	1.29	2.23	2.61	-	-	-
	Out	$\mathbf{S}_{\mathbf{11}}^{\mathbf{out}}$	$\mathbf{S}_{\mathbf{22}}^{\mathbf{out}}$	$\mathbf{S}_{\mathbf{33}}^{\mathbf{out}}$	$\mathbf{S}_{\mathbf{44}}^{\mathbf{out}}$	$\mathbf{S}_{\mathbf{55}}^{\mathbf{out}}$	$\mathbf{S}_{\mathbf{66}}^{\mathbf{out}}$	$\mathbf{S}_{\mathbf{77}}^{\mathbf{out}}$
	SWCNT	0.31	0.61	1.19	1.53	2.02	2.41	2.76
	DW(1)	0.31	0.60	1.19	1.57	2.02	2.46	2.75
	DW(-1)	0.31	0.59	1.20	1.53	2.02	2.41	2.69

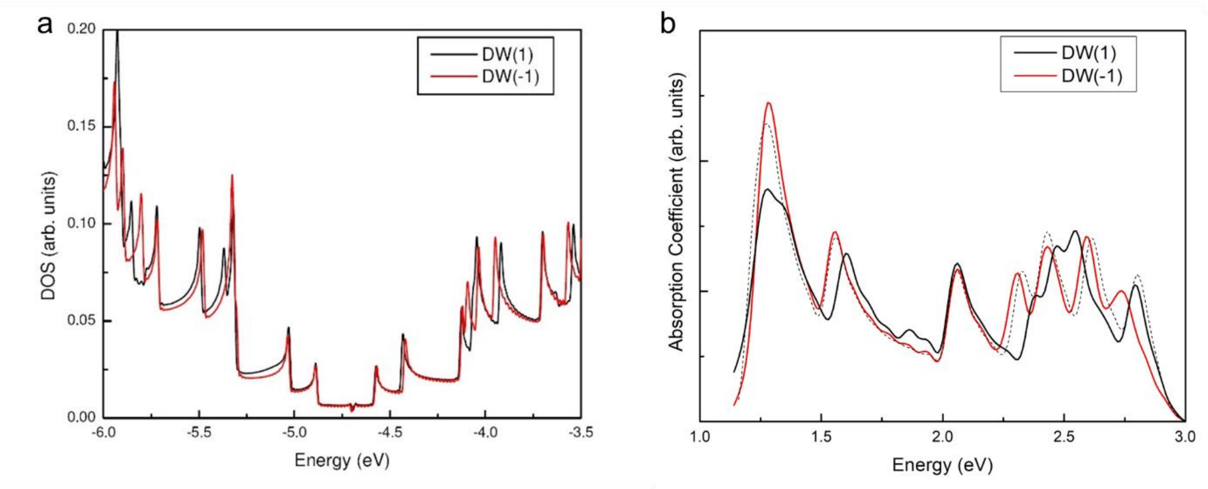

Figure S4.5. (a) Electronic DOS and (b) absorption coefficient of DWCNT-7 (18,6)@(21,14) with equal (DW(1), black line) and opposite (DW(-1), red line) handedness calculated within *ab initio*-based NTB approach [10]. The dotted line in (b) represents the weighted sum of absorption coefficients of DWCNT layers in the absence of van der Waals interactions. The transition energies are summarized in Table S4.2.

Section S5. Details on the Rayleigh data processing and fitting procedures

The experimental Rayleigh spectra were first converted from wavelength to energy scale using the Jacobian transformation, as described in Ref. [14]. Then, each spectrum was fitted by a least-squares optimization procedure with the following complex optical susceptibility function [15]:

$$I_{Rayleigh} = \omega^3(|\chi_{in}|^2 + |\chi_{out}|^2)$$

$$\chi_{in} = \sum_{i=1}^{N1} \frac{A_i^{in}}{\omega_i^{in} - \omega - i\gamma_i^{in}/2} + \chi_{non-res}^{in}$$

$$\chi_{out} = \sum_{i=1}^{N2} \frac{A_i^{out}}{\omega_i^{out} - \omega - i\gamma_i^{out}/2} + \chi_{non-res}^{out}$$

where A_k, ω_k, γ_k (k = in, out) correspond to the amplitude, resonance frequency and linewidth of the complex Lorentzian function, respectively. The total number of transitions N_1 and N_2 and their approximated energies were estimated based on the SWCNT energies from the Atlas [6] and the shifts due to van der Waals electronic coupling [7] (see Tables in Section S2). The $\chi_{in}^{non-res}$ and $\chi_{out}^{non-res}$ modeled by real linear functions represent the effective non-resonant contributions of the transitions outside of the measured experimental range. These contributions were shown to be essential to account for the observed asymmetry of Rayleigh spectrum features [15].

Section S6. Details on the ERS data processing and fitting procedures

We present here the details of the processing and fitting of the wide-range Raman spectra presented in Sections S3-S4.

Data processing. First, we subtracted the background spectrum from all Raman spectra measured on the Acton SP2500 spectrometer to remove the artifact at ~ 400-500 cm^{-1} (Figure S6.1). Besides, we correct all Raman spectra measured in the NIR (shown as REMs in Figure 3 and in Section S4) for the instrument response and laser power variation during the measurements.

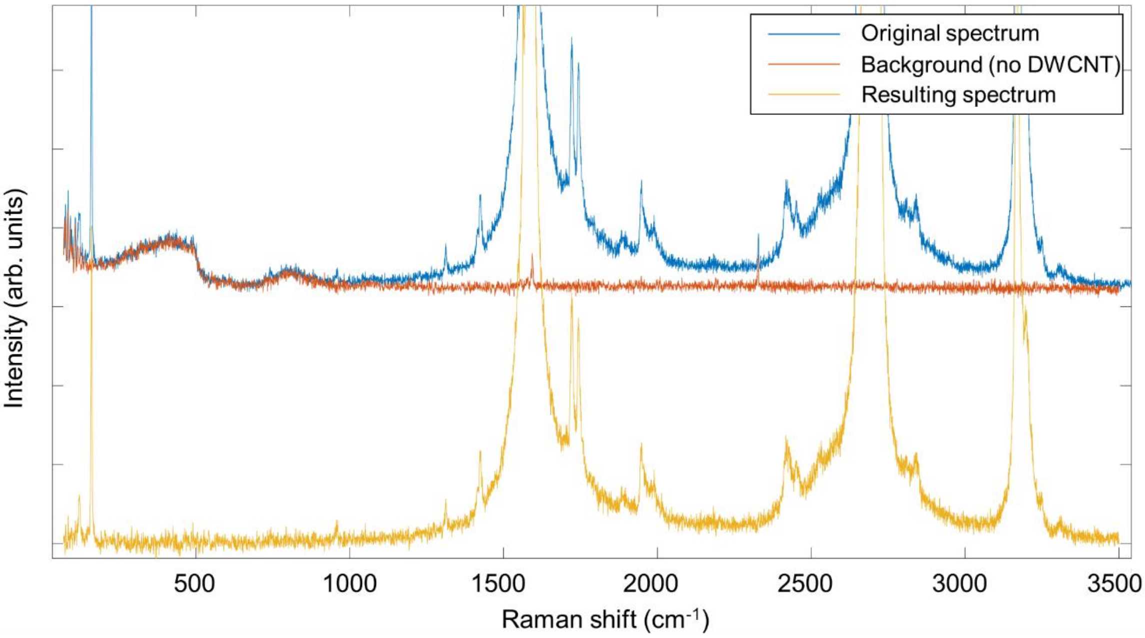

Figure S6.1. Result of the background subtraction for a DWCNT.

Data fitting. We fitted the wide-range Raman spectra for the given DWCNT simultaneously, *i.e.*, by sharing peak parameters between all spectra, with the following function:

$$I_j^{Raman} = \sum_{i=1}^{N1} F_i^{phonon} + \sum_{k=1}^{N2} F_k^{ERS} + F_{bkg}$$

where I_j^{Raman} is the intensity of the j-th Raman spectrum, F_{bkg} is a linear function representing the remaining background, $F_i^{phonon}$and $F_k^{ERS}$are Lorentzian functions for phonon and ERS lines, respectively defined as:

$$F_i^{phonon} = \frac{A_i^{phonon}}{\left(x - \omega_i^{phonon}\right)^2 + \left(0.5\gamma_i^{phonon}\right)^2}$$

$$F_k^{ERS} = \frac{A_k^{ERS}}{(x - \omega_k^{ERS})^2 + (0.5\gamma_k^{ERS})^2}$$

where ω_i^{phonon}, γ_i^{phonon}, A_i^{phonon}, $\omega_k^{ERS} = f(\lambda_{laser})$, γ_k^{ERS}, A_k^{ERS} are phonon frequency, phonon linewidth, phonon line amplitude, ERS frequency at the given excitation wavelength λ_{laser}, ERS linewidth and ERS amplitude, respectively. The ERS frequency (in cm^{-1}) for a given spectrum (i.e. at the excitation wavelength λ_{laser} in nm) is determined from the M_{ii} energy in eV by:

$$\omega_k^{ERS} = \frac{10^7}{\lambda_{laser}} - \frac{M_{ii}}{0.000124}$$

The examples of the simultaneous fit for DWCNT-4 and DWCNT-10 are shown in Figure S6.2.

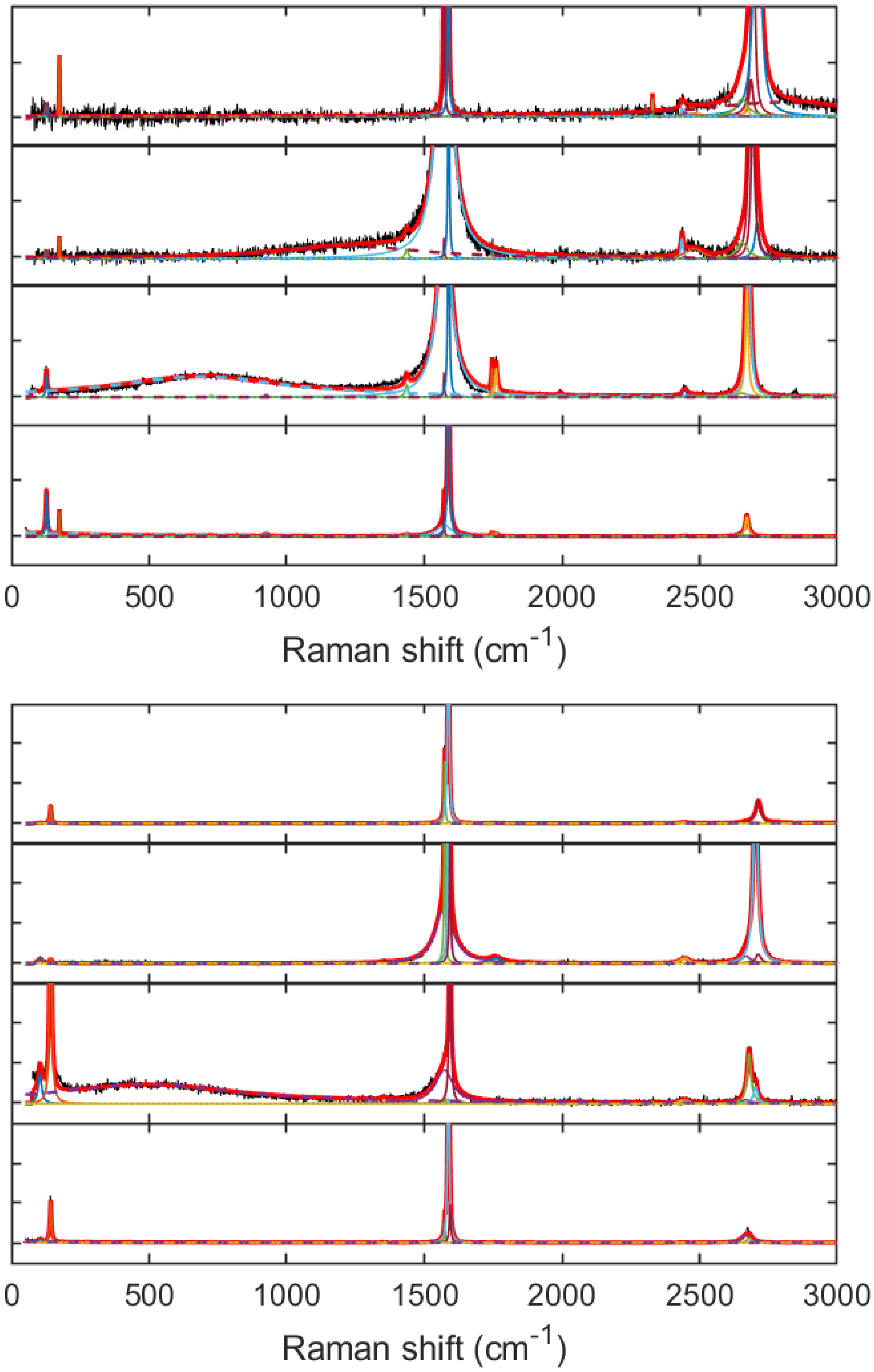

Figure S6.2. Simultaneous fit results for DWCNT-4 (upper) and DWCNT-10 (bottom). Solid black and red curves represent experimental and fitted spectra, respectively. Solid and dashed colored lines correspond to the phonon and ERS peaks, respectively.

Role of interference effects between ERS and phonon lines. Saito *et al.* [16] previously predicted that the quantum interference between ERS and RBLM (or G-band) leads to the frequency shifts and changes in the lineshape (from symmetric to asymmetric) of the phonon lines. These changes become more pronounced if the intensity of ERS peaks is large relative to phonon peaks. However, we find that in DWCNTs, the ERS line due to its suppressed intensity leads to minor changes in the phonon properties. For instance, it is evidenced in Figure S6.3, where the frequencies of RBLM and G-band barely change as a function of excitation wavelengths.

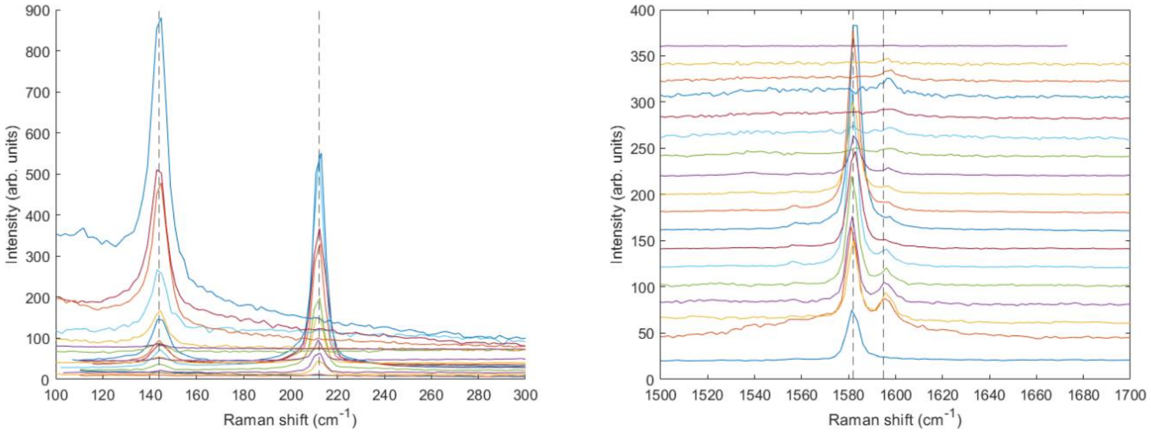

Figure S6.3. RBLM (left) and G-band (right) regions of Raman spectra of DWCNT-1 measured with 300 grooves/mm grating at 699.9, 750, 768.2, 771, 780, 785.2, 792, 800, 807, 815, 822, 837, 845, 852, 861.4, 865.9, 872.9 and 885 nm (from top to bottom).

Section S7. Table with results of the ERS fitting for DWCNTs

We note that we chose to present the results of the ERS data fit in the form of intensity (height) ratio I_{ERS}/I_{LO} because it allows the direct comparison with the available literature data on SWCNTs. The broad LO mode was chosen for reference since it is considered representative of metallic SWCNT [17], and from our experience it is much easier to identify it in the rich *G*-band spectra of DWCNTs. The only problem may occur with the armchair SWCNTs, where the LO mode is absent, but we did not observe such chiralities in our experimental data set. On the other hand, choosing the narrow TO mode for the reference may complicate the analysis of (close) zig-zag metallic DWCNT layers, where the narrow TO component is absent or hard to identify due to the overlap with the narrow LO modes of semiconducting layers.

Table S7.1. Results of the ERS data fitting for investigated individual DWCNTs. For each *(n,m)* chirality, the diameter *d*, uncertainty in diameter *δd* (relevant for DWCNTs characterized by optical spectroscopy), interlayer distance *Δr*, chiral angle *θ*, the cutting line index *p (*L or H stand for the lower and higher transitions), laser excitation energy E_L, experimental transition energy E_{ERS} and energy separation $dE = E_L – E_{ERS}$ are given. R_H and δR_H correspond to the ratio (I_{ERS}/I_{LO}) and its uncertainty (two standard deviations), respectively; ω_{LO} is the frequency of the LO phonon.

DWCNT	*n*	*m*	*d* (nm)	*δd* (nm)	*θ* (°)	Layer	*Δr* (nm)	*p*		E_{ERS}	*dE* (eV)	R_H	δR_H	E_L(eV)	ω_{LO} (cm^{-1})
(14,1)@(15,12)	15	12	1.834	0.000	26.33	out	0.3486	3	L	1.44	0.212	0.218	0.091	1.650	1568.6
(14,1)@(15,12)	15	12	1.834	0.000	26.33	out	0.3486	3	L	1.44	0.022	16.066	10.186*	1.460	1568.6
(14,1)@(15,12)	15	12	1.834	0.000	26.33	out	0.3486	6	L	2.63	0.079	0.228	0.029	2.710	1568.6
(14,1)@(15,12)	15	12	1.834	0.000	26.33	out	0.3486	6	H	2.68	0.029	0.180	0.069	2.710	1568.6
(14,2)@(22,4)	14	2	1.182	0.000	6.59	in	0.3581	3	L	1.86	0.351	0.124	0.014	2.210	1547.4
(14,2)@(22,4)	14	2	1.182	0.000	6.59	in	0.3581	3	L	1.86	0.101	0.215	0.025	1.960	1547.4
(14,2)@(22,4)	14	2	1.182	0.000	6.59	in	0.3581	3	L	1.86	0.021	0.734	0.219	1.880	1547.4
(14,2)@(22,4)	14	2	1.182	0.000	6.59	in	0.3581	3	H	2.15	0.369	0.039	0.017	2.520	1547.4
(14,2)@(22,4)	14	2	1.182	0.000	6.59	in	0.3581	3	H	2.15	0.179	0.018	0.013	2.330	1547.4
(14,2)@(22,4)	14	2	1.182	0.000	6.59	in	0.3581	3	H	2.15	0.059	0.038	0.017	2.210	1547.4
(14,2)@(22,4)	22	4	1.898	0.000	8.21	out	0.3581	3	L	1.35	0.254	0.259	0.022	1.600	1577.0
(14,2)@(22,4)	22	4	1.898	0.000	8.21	out	0.3581	3	L	1.35	0.114	1.313	0.253	1.460	1577.0
(14,2)@(22,4)	22	4	1.898	0.000	8.21	out	0.3581	3	H	1.47	0.133	0.217	0.023	1.600	1577.0
(14,2)@(22,4)	22	4	1.898	0.000	8.21	out	0.3581	3	H	1.47	-0.007	2.778	0.564	1.460	1577.0
(14,2)@(22,4)	22	4	1.898	0.000	8.21	out	0.3581	3	H	2.34	0.182	0.019	0.006	2.520	1577.0
(14,2)@(22,4)	22	4	1.898	0.000	8.21	out	0.3581	3	H	2.34	-0.008	0.083	0.021	2.330	1577.0
(11,8)@(19,10)	11	8	1.294	0.000	24.79	in	0.3520	3	L	1.90	0.433	0.156	0.069	2.330	1521.9
(11,8)@(19,10)	11	8	1.294	0.000	24.79	in	0.3520	3	L	1.90	0.063	0.365	0.162	1.960	1521.9
(11,8)@(19,10)	11	8	1.294	0.000	24.79	in	0.3520	3	H	1.96	0.373	0.340	0.129	2.330	1521.9
(11,8)@(19,10)	11	8	1.294	0.000	24.79	in	0.3520	3	H	1.96	0.003	1.286	0.448	1.960	1521.9
(11,8)@(19,10)	19	10	1.998	0.000	19.84	out	0.3520	3	H	1.36	0.244	0.546	0.064	1.600	1572.3
(11,8)@(19,10)	19	10	1.998	0.000	19.84	out	0.3520	6	L	2.38	0.334	0.047	0.015	2.710	1572.3
(11,8)@(19,10)	19	10	1.998	0.000	19.84	out	0.3520	6	L	2.38	0.154	0.092	0.008	2.530	1572.3
(11,8)@(19,10)	19	10	1.998	0.000	19.84	out	0.3520	6	L	2.38	-0.046	2.404	0.243	2.330	1572.3
(14,5)@(26,1)	14	5	1.336	0.000	14.70	in	0.3701	3	L	1.81	0.401	0.175	0.102	2.210	1545.5
(14,5)@(26,1)	14	5	1.336	0.000	14.70	in	0.3701	3	L	1.81	0.151	0.000	-	1.960	1545.5
(14,5)@(26,1)	14	5	1.336	0.000	14.70	in	0.3701	3	H	1.96	0.249	0.202	0.034	2.210	1545.5
(14,5)@(26,1)	14	5	1.336	0.000	14.70	in	0.3701	3	H	1.96	-0.001	0.087	0.007	1.960	1545.5
(18,2)@(19,13)	19	13	2.182	0.000	23.82	out	0.3443	6	L	2.25	0.275	0.013	0.003	2.520	1572.4
(18,2)@(19,13)	19	13	2.182	0.000	23.82	out	0.3443	6	L	2.25	0.085	0.113	0.006	2.330	1572.4
(18,2)@(19,13)	19	13	2.182	0.000	23.82	out	0.3443	6	L	2.25	-0.035	0.600	0.055	2.210	1572.4
(18,2)@(19,13)	19	13	2.182	0.000	23.82	out	0.3443	6	H	2.37	0.152	0.063	0.004	2.520	1572.4
(14,8)@(19,14)	14	8	1.510	0.000	21.05	in	0.3680	3	L	1.59	0.372	0.000	-	1.960	1542.2
(14,8)@(19,14)	14	8	1.510	0.000	21.05	in	0.3680	3	L	1.59	0.292	0.130	0.012	1.880	1542.2
(14,8)@(19,14)	14	8	1.510	0.000	21.05	in	0.3680	3	L	1.59	0.192	0.373	0.044	1.780	1542.2
(14,8)@(19,14)	14	8	1.510	0.000	21.05	in	0.3680	3	L	1.59	0.072	0.920	0.047	1.660	1542.2

(14,8)@(19,14)	14	8	1.510	0.000	21.05	in	0.3680	3	L	1.59	0.012	2.086	0.278	1.600	1542.2
(14,8)@(19,14)	14	8	1.510	0.000	21.05	in	0.3680	3	H	1.74	0.218	0.031	0.039	1.960	1542.2
(14,8)@(19,14)	14	8	1.510	0.000	21.05	in	0.3680	3	H	1.74	0.138	0.334	0.016	1.880	1542.2
(14,8)@(19,14)	14	8	1.510	0.000	21.05	in	0.3680	3	H	1.74	0.038	0.838	0.067	1.780	1542.2
(14,8)@(19,14)	14	8	1.510	0.000	21.05	in	0.3680	3	H	1.74	-0.082	0.631	0.170	1.660	1542.2
(18,6)@(21,14)	18	6	1.694	0.000	13.90	in	0.3476	3	L	1.53	0.046	1.526	0.114	1.580	1561.0
(18,6)@(21,14)	18	6	1.694	0.000	13.90	in	0.3476	6	L	2.64	0.07	0.060	0.007	2.710	1561.0
(17,14)@(26,14)	17	14	2.105	0.000	26.80	in	0.3237	6	L	2.25	0.462	0.000	-	2.710	1573.8
(17,14)@(26,14)	17	14	2.105	0.000	26.80	in	0.3237	6	L	2.25	0.282	0.000	-	2.530	1573.8
(17,14)@(26,14)	17	14	2.105	0.000	26.80	in	0.3237	6	H	2.45	0.26	0.000	-	2.710	1573.8
(17,14)@(26,14)	17	14	2.105	0.000	26.80	in	0.3237	6	H	2.45	0.08	0.000	-	2.530	1573.8
(17,14)@(26,14)	26	14	2.752	0.000	20.17	out	0.3237	6	L	1.76	0.45	0.000	-	2.210	1573.8
(17,14)@(26,14)	26	14	2.752	0.000	20.17	out	0.3237	6	H	1.95	0.262	0.000	-	2.210	1573.8
(17,14)@(28,12)	17	14	2.105	0.000	26.80	in	0.3392	6	L	2.27	0.26	0.016	0.005	2.530	1572.2
(17,14)@(28,12)	17	14	2.105	0.000	26.80	in	0.3392	6	L	2.27	0.06	0.590	0.032	2.330	1572.2
(22,13)@(39,2)	22	13	2.399	0.000	21.56	in	0.3677	6	L	2.14	0.381	0.000	-	2.520	1558.8
(22,13)@(39,2)	22	13	2.399	0.000	21.56	in	0.3677	6	L	2.14	0.191	0.026	0.083	2.330	1558.8
(22,13)@(39,2)	22	13	2.399	0.000	21.56	in	0.3677	6	L	2.14	0.071	0.058	0.189	2.210	1558.8
(22,13)@(39,2)	22	13	2.399	0.000	21.56	in	0.3677	6	H	2.20	0.324	0.000	-	2.520	1558.8
(22,13)@(39,2)	22	13	2.399	0.000	21.56	in	0.3677	6	H	2.20	0.134	0.109	0.125	2.330	1558.8
(22,13)@(39,2)	22	13	2.399	0.000	21.56	in	0.3677	6	H	2.20	0.014	0.010	0.172	2.210	1558.8
DWCNT-11	-	-	2.208	0.048	-	out	-	6	L	2.19	0.335	0.094	0.010	2.520	1575.6
DWCNT-11	-	-	2.208	0.048	-	out	-	6	L	2.19	0.145	0.113	0.007	2.330	1575.6
DWCNT-11	-	-	2.208	0.048	-	out	-	6	L	2.19	0.025	0.336	0.017	2.210	1575.6
DWCNT-11	-	-	2.208	0.048	-	out	-	6	H	2.31	0.207	0.173	0.014	2.520	1575.6
DWCNT-11	-	-	2.208	0.048	-	out	-	6	H	2.31	0.017	0.189	0.014	2.330	1575.6
DWCNT-13	-	-	2.227	0.044	-	out	-	6	L	2.08	0.437	0.017	0.012	2.520	1602.0
DWCNT-13	-	-	2.227	0.044	-	out	-	6	L	2.08	0.247	0.060	0.063	2.330	1602.0
DWCNT-13	-	-	2.227	0.044	-	out	-	6	L	2.08	0.127	0.088	0.072	2.210	1602.0
DWCNT-13	-	-	2.227	0.044	-	out	-	6	H	2.17	0.348	0.392	0.059	2.520	1602.0
DWCNT-13	-	-	2.227	0.044	-	out	-	6	H	2.17	0.158	0.073	0.060	2.330	1602.0
DWCNT-13	-	-	2.227	0.044	-	out	-	6	H	2.17	0.038	0.021	0.039	2.210	1602.0
DWCNT-14	-	-	2.830	0.025	-	out	-	6	L	1.88	0.079	0.130	0.008	1.960	1572.1
DWCNT-14	-	-	2.830	0.025	-	out	-	6	H	2.02	-0.063	0.000	-	1.960	1572.1
(11,6)@(18,9)	18	9	1.864	0.000	19.11	out	0.3475	6	L	2.60	0.115	0.055	0.019	2.710	1572.0

*the large value of δR_H is due to the large uncertainty in the LO intensity determined from the fit

Section S8. Table with results of the ERS data digitization for SWCNTs

Table S8.1. Results of the ERS data digitization for SWCNTs from the literature [18–20]. For each *(n,m)* chirality, the diameter *d*, chiral angle *θ*, the cutting line index *p (*L or H stand for the lower and higher transitions), laser excitation energy E_L, experimental transition energy E_{ERS} and energy separation $dE = E_L - E_{ERS}$ are given. R_H and δR_H correspond to the ratio (I_{ERS}/I_{LO}) and its uncertainty (determined from the pixels in the image), respectively.

n	***m***	***d* (nm)**	***θ* (°)**	**E_L (eV)**	**I_{ERS} (pix)**	**I_{LO} (pix)**	**R_H**	**δR_H**	**E_{ERS} (eV)**	***p***		***dE* (eV)**
23	14	2.53	22.01	2.14	134	505	0.265	0.006	2.095	6	L	0.045
12	9	1.43	25.28	1.96	52	62	0.839	0.060	1.888	3	H	0.071
12	9	1.43	25.28	1.96	69	62	1.113	0.068	1.817	3	L	0.142
13	7	1.38	20.17	1.96	92	148	0.622	0.023	1.836	3	L	0.123
14	5	1.34	14.70	1.96	124	150	0.827	0.024	1.837	3	L	0.122
15	3	1.31	8.95	1.96	144	176	0.818	0.021	1.835	3	L	0.124
16	1	1.29	3.00	1.96	141	161	0.876	0.023	1.834	3	L	0.125
12	9	1.43	25.28	2.33	18	17	1.059	0.242	1.884	3	H	0.446
14	5	1.34	14.70	2.33	41	40	1.025	0.101	2.044	3	H	0.286
11	8	1.29	24.79	2.33	18	12	1.500	0.425	2.028	3	H	0.302
11	8	1.29	24.79	2.33	32	12	2.667	0.671	1.936	3	L	0.394
12	6	1.24	19.11	2.33	62	241	0.257	0.012	2.155	3	H	0.175
12	6	1.24	19.11	2.33	32	241	0.133	0.012	1.956	3	L	0.374
13	4	1.21	13.00	2.33	250	492	0.508	0.006	2.244	3	H	0.086
13	4	1.21	13.00	2.33	43	492	0.087	0.006	1.942	3	L	0.388
14	2	1.18	6.59	2.33	117	426	0.275	0.007	1.949	3	L	0.381
17	5	1.56	12.52	1.96	34	130	0.262	0.022	1.793	3	H	0.166
17	5	1.56	12.52	1.96	22	130	0.169	0.022	1.624	3	L	0.335
13	10	1.56	25.69	1.96	10	135	0.074	0.021	1.750	3	H	0.209
13	10	1.56	25.69	1.96	21	135	0.156	0.021	1.688	3	L	0.271
16	1	1.29	3.00	2.33	52	229	0.227	0.013	2.182	3	H	0.148
16	1	1.29	3.00	2.33	25	229	0.109	0.012	1.823	3	L	0.507
13	7	1.38	20.17	2.33	39	29	1.345	0.163	1.979	3	H	0.351
13	7	1.38	20.17	2.33	44	29	1.517	0.177	1.826	3	L	0.504
13	7	1.38	20.17	1.96	111	216	0.514	0.015	1.820	3	L	0.139
14	5	1.34	14.70	2.33	37	84	0.440	0.037	2.066	3	H	0.264
14	5	1.34	14.70	2.33	116	84	1.381	0.057	1.825	3	L	0.505

Section S9. Comparison of I_{ERS}/I_{LO} ratios in individual free-standing SWCNTs and DWCNTs.

About comparison of SWCNT and DWCNT data. As we mentioned in Section S7, presenting the results of the ERS data fit in the form of intensity (height) ratio I_{ERS}/I_{LO} allows the direct comparison with the available literature data on SWCNTs. However, there are certain remarks to be made:

- SWCNT and DWCNT data should be analyzed by keeping in mind that they were obtained under (possibly) different lab conditions (*e.g.*, humidity, room temperature), which may affect the presented values. In the future, the best approach would be to probe the same chiralities in the SWCNT and DWCNT forms under the same lab conditions.
- Some of the *(n,m)* chiralities in SWCNT and DWCNT from Table 1 (main text) were measured at slightly different resonance conditions (e.g., values of $dE = E_L - E_{ii}$) despite the same laser excitation wavelengths were used. It is explained by the fact that electronic transition energies in DWCNTs are shifted by interlayer van der Waals electronic coupling. Nevertheless, for large *dE* values, the resonance effect should be less important relative to intrinsic factors like dielectric screening and IET (see slowly changing ERS intensity values away from resonance in Figure 3b,d) and should not change the conclusions of the work.
- Finally, we discuss the possible origin of high I_{ERS}/I_{LO} values in SWCNTs [18–20] for $E_L - E_{ii} > 300$ meV (Figure 2c, top panel) compared to DWCNT data. Since the ERS lines in this spectral region overlap with the intense higher-order modes (e.g., *2D* or *G+2D*), they could be misinterpreted with some of the phonon modes during the fit. In the future, the behavior of ERS lines in this spectral region should be studied further.

Dependence of I_{ERS}/I_{LO} ratios on *d* and θ. We present in Figure S9 the dependence of the I_{ERS}/I_{LO} ratios on the diameter and chiral angle for SWCNTs from the literature [18–20] and DWCNTs from this work.

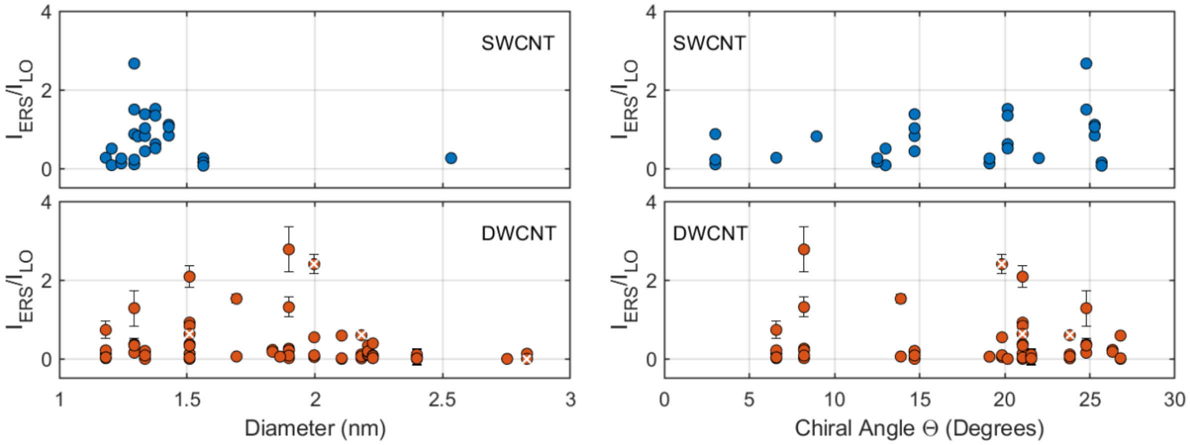

Figure S9. Dependence of I_{ERS}/I_{LO} ratio on the diameter and chiral angle for SWCNTs from the literature [18–20] and DWCNTs from this work. The error bars for DWCNTs correspond to two standard deviations. White crosses indicate data points with $E_{Laser} - E_{ii} < -0.01$ eV obtained through simultaneous fit of ERS peak tails in Stokes Raman spectra (SI Section S6; peak linewidths and positions in these cases were fixed by the parameters of the same ERS lines in other spectra with E_{Laser} - E_{ii} > 0) and do not correspond to Anti-Stokes Raman spectra.

Section S10. Dependence of I_{ERS}/I_{LO} ratio on structural parameters of DWCNT layers

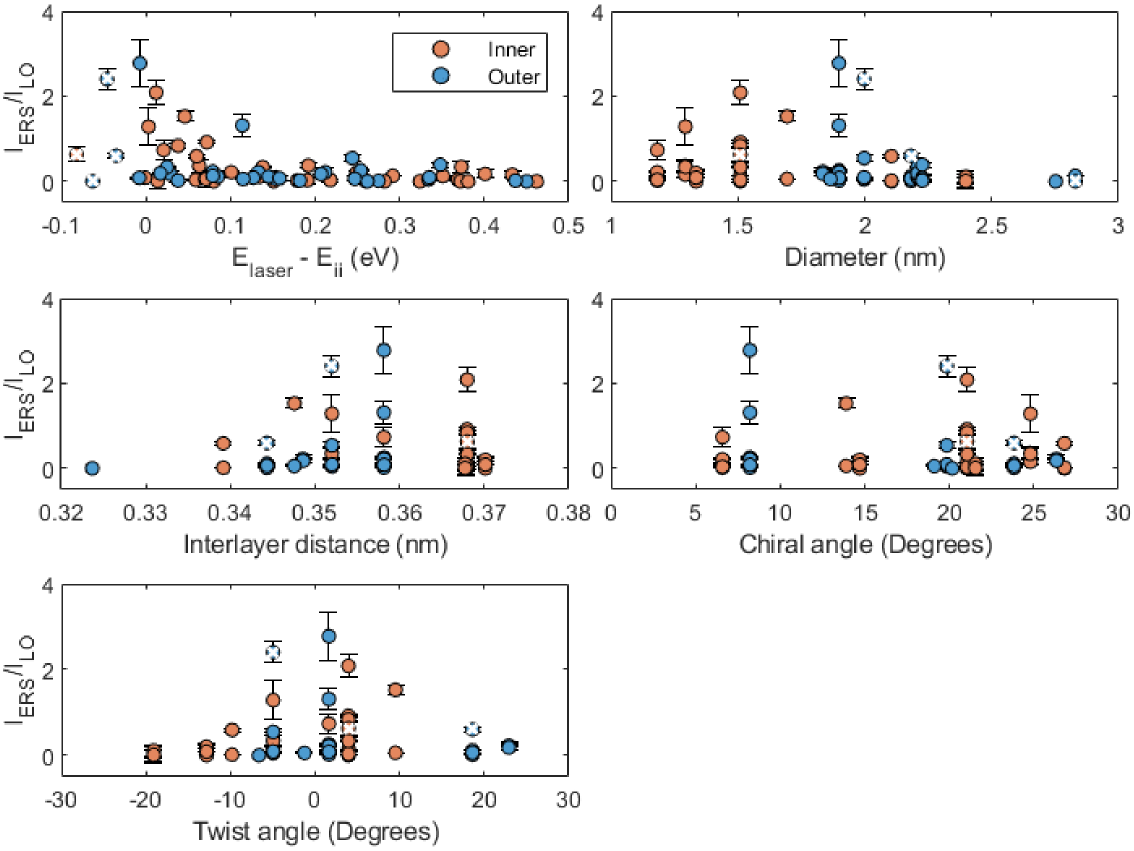

Figure S10. Dependence of I_{ERS}/I_{LO} ratio on the resonance condition and structural parameters of inner and outer layers of DWCNTs. The error bars for DWCNTs correspond to two standard deviations. White crosses indicate data points with E_{Laser} - E_{ii} < -0.01 eV obtained through simultaneous fit of ERS peak tails in Stokes Raman spectra (SI Section S6; peak linewidths and positions in these cases were fixed by the parameters of the same ERS lines in other spectra with E_{Laser} - E_{ii} > 0) and do not correspond to Anti-Stokes Raman spectra.

Section S11. Effect of curvature-induced bandgap on ERS lines

We calculated the curvature-induced bandgap values for all geometrically possible metallic SWCNTs with diameters below 3 nm using the equation [21]:

$$E_{gap} = \frac{3 \cdot \gamma_0 \cdot a_{c-c}^2}{4 \cdot d} \cdot \cos(3\theta)$$

The dependences of this bandgap value on the metallic SWCNT diameter and chiral angle are plotted in Figure S11.1. In principle, if the Raman spectrum of a metallic SWCNT is excited under condition $E_L - M_{ii} < E_{gap}$, the ERS process is affected by the curvature-induced bandgap since there are no low-energy excitons available for inelastic scattering. We show what it means in practice by plotting the bandgap energy in terms of Raman shift (horizontal dashed lines labeled 100, 200 and 300 cm^{-1}) in Figure S11.1. SWCNTs lying below the 100 cm^{-1} dashed line have such a bandgap that exciting them under the resonance conditions $E_L - M_{ii} > E_{gap} = 100$ cm^{-1} will always result in the observation of ERS peaks above 100 cm^{-1}. On the other hand, we define all SWCNTs above 100 cm^{-1} as belonging to Zone I in Figure 5 (main text).

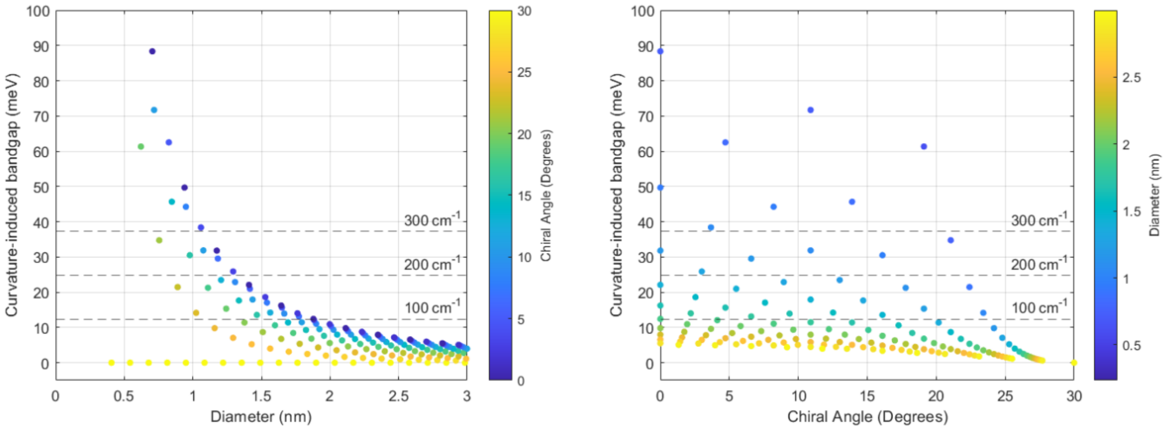

Figure S11.1. Dependence of the curvature-induced bandgap opening in metallic SWCNTs on the diameter and chiral angle. The horizontal dashed lines show the bandgap energy in terms of Raman shift.

Section S12. Estimation of the interlayer charge transfer between the layers of DWCNTs

The interlayer charge transfer density (in units of *e*/Å) for the probed DWCNTs was calculated using the formula from Zólyomi *et al.* [22]:

$$Q_{CT} = -0.06 \cdot \Delta r + 0.23$$

The calculated Q_{CT} values for inner and outer layers were then converted into units of e^-/C atom and are shown in Table S12.1 and Figure S12. The charge transfer necessary for the complete quenching of ERS peaks in individual metallic SWCNTs ($Q_{CT} \leq 0.005$ *e*/C atom) was previously estimated by Farhat *et al.* [20] and is represented by the dashed line in Figure S12.

Table S12.1. Charge transfer density for investigated DWCNTs calculated using the formula from Zólyomi *et al.* [22].

#	**n_{in}**	**m_{in}**	**D_{in} (nm)**	**Type**	**n_{out}**	**m_{out}**	**D_{out} (nm)**	**Type**	**<D> (nm)**	**Δr (nm)**	**Q_{in} (10^{-5} e/C atom)**	**Q_{out} (10^{-5} e/C atom)**
1	**14**	**1**	1.137	1	**15**	**12**	1.834	0	1.486	0.349	88	55
2	**11**	**6**	1.169	2	**18**	**9**	1.864	0	1.517	0.348	89	56
3	**14**	**2**	1.182	0	**22**	**4**	1.898	0	1.540	0.358	62	38
4	**11**	**8**	1.294	0	**19**	**10**	1.998	0	1.646	0.352	70	45
5	**14**	**5**	1.336	0	**26**	**1**	2.076	1	1.706	0.370	29	18
6	**18**	**2**	1.494	1	**19**	**13**	2.182	0	1.838	0.344	75	52
7	**14**	**8**	1.510	0	**19**	**14**	2.246	2	1.878	0.368	29	20
8	**18**	**6**	1.694	0	**21**	**14**	2.389	1	2.041	0.348	61	43
9	**17**	**14**	2.105	0	**26**	**14**	2.752	0	2.429	0.324	82	63
10	**17**	**14**	2.105	0	**28**	**12**	2.783	1	2.444	0.339	61	46
11	**22**	**13**	2.399	0	**39**	**2**	3.134	1	2.767	0.368	19	14

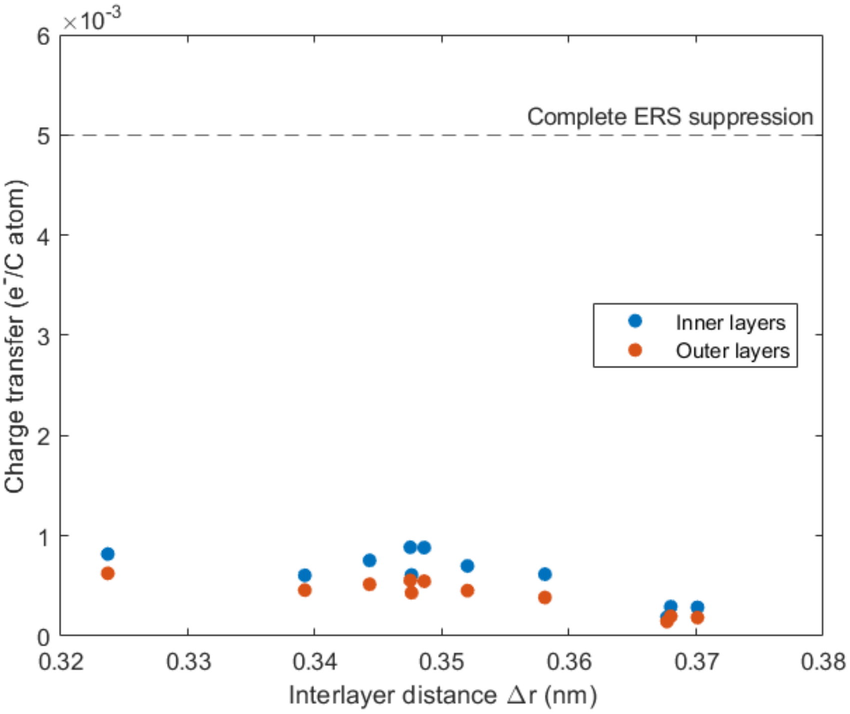

Fig. S12. Estimation of the charge transfer between the layers of DWCNTs according to Zólyomi *et al.* [22]

References

[1] D.I. Levshov, H.N. Tran, M. Paillet, R. Arenal, X.T. Than, A.A. Zahab, Y.I. Yuzyuk, J.-L. Sauvajol, T. Michel, Accurate determination of the chiral indices of individual carbon nanotubes by combining electron diffraction and Resonant Raman spectroscopy, Carbon. 114 (2017) 141–159. doi:10.1016/j.carbon.2016.11.076.

[2] S. Berciaud, V. V. Deshpande, R. Caldwell, Y. Miyauchi, C. Voisin, P. Kim, J. Hone, T.F. Heinz, All-optical structure assignment of individual single-walled carbon nanotubes from Rayleigh and Raman scattering measurements, Phys. Status Solidi. 249 (2012) 2436–2441. doi:10.1002/pssb.201200152.

[3] S. Rochal, D. Levshov, M. Avramenko, R. Arenal, T.T. Cao, V.C. Nguyen, J.-L. Sauvajol, M. Paillet, Chirality manifestation in elastic coupling between the layers of double-walled carbon nanotubes, Nanoscale. 11 (2019) 16092–16102. doi:10.1039/C9NR03853A.

[4] D.I. Levshov, H.N. Tran, T. Michel, T.T. Cao, V.C. Nguyen, R. Arenal, V.N. Popov, J.-L. Sauvajol, A.-A. Zahab, M. Paillet, Interlayer Interaction Effects on the G Modes in Double-Walled Carbon Nanotubes With Different Electronic Configurations, Phys. Status Solidi. 254 (2017) 1700251. doi:10.1002/pssb.201700251.

[5] D.I. Levshov, R. Parret, H.-N. Tran, T. Michel, T.T. Cao, V.C. Nguyen, R. Arenal, V.N. Popov, S.B. Rochal, J.-L. Sauvajol, A.-A. Zahab, M. Paillet, Photoluminescence from an individual double-walled carbon nanotube, Phys. Rev. B. 96 (2017) 195410. doi:10.1103/PhysRevB.96.195410.

[6] K. Liu, J. Deslippe, F. Xiao, R.B. Capaz, X. Hong, S. Aloni, A. Zettl, W. Wang, X. Bai, S.G. Louie, E. Wang, F. Wang, An atlas of carbon nanotube optical transitions, Nat. Nanotechnol. 7 (2012) 325–329. doi:10.1038/nnano.2012.52.

[7] D. V. Chalin, S.B. Rochal, Band structure and inter-tube optical transitions in double-walled carbon nanotubes, Phys. Rev. B. 102 (2020) 115426. doi:10.1103/PhysRevB.102.115426.

[8] H. Tran, Raman Scattering and Optical Spectroscopies of Individual Pristine and Functionalized Carbon Nanotubes, University Montpellier, 2015. https://tel.archives-ouvertes.fr/tel-01391869.

[9] F. Wang, W. Liu, Y. Wu, M.Y. Sfeir, L. Huang, J. Hone, S. O’Brien, L.E. Brus, T.F. Heinz, Y.R. Shen, Multiphonon Raman Scattering from Individual Single-Walled Carbon Nanotubes, Phys. Rev. Lett. 98 (2007) 047402. doi:10.1103/PhysRevLett.98.047402.

[10] V.N. Popov, Theoretical evidence of a significant modification of the electronic structure of double-walled carbon nanotubes due to the interlayer interaction, Carbon. 170 (2020) 30–36. doi:10.1016/j.carbon.2020.07.036.

[11] J. Yang, D. Zhang, Y. Hu, C. Xia, S. Sun, Y. Li, Bilayer Plots for Accurately Determining the Chirality of Single-Walled Carbon Nanotubes Under Complex Environments, ACS Nano. 11 (2017) acsnano.7b05860. doi:10.1021/acsnano.7b05860.

[12] D. Levshov, T.X. Than, R. Arenal, V.N. Popov, R. Parret, M. Paillet, V. Jourdain, A.A. Zahab, T. Michel, Y.I. Yuzyuk, J.-L. Sauvajol, Experimental Evidence of a Mechanical Coupling between Layers in an Individual Double-Walled Carbon Nanotube, Nano Lett. 11 (2011) 4800–4804. doi:10.1021/nl2026234.

[13] K. Liu, X. Hong, M. Wu, F. Xiao, W. Wang, X. Bai, J.W. Ager, S. Aloni, A. Zettl, E. Wang, F. Wang, Quantum-coupled radial-breathing oscillations in double-walled carbon nanotubes, Nat. Commun. 4 (2013) 1375. doi:10.1038/ncomms2367.

[14] J. Mooney, P. Kambhampati, Get the Basics Right: Jacobian Conversion of Wavelength and Energy Scales for Quantitative Analysis of Emission Spectra, J. Phys. Chem. Lett. 4 (2013) 3316–3318. doi:10.1021/jz401508t.

[15] S. Berciaud, C. Voisin, H. Yan, B. Chandra, R. Caldwell, Y. Shan, L.E. Brus, J. Hone, T.F. Heinz, Excitons and high-order optical transitions in individual carbon nanotubes: A Rayleigh scattering spectroscopy study, Phys. Rev. B. 81 (2010) 041414.

doi:10.1103/PhysRevB.81.041414.
[16] R. Saito, A.R.T. Nugraha, E.H. Hasdeo, N.T. Hung, W. Izumida, Electronic and Optical Properties of Single Wall Carbon Nanotubes, Top. Curr. Chem. 375 (2017) 7. doi:10.1007/s41061-016-0095-2.
[17] T. Michel, M. Paillet, a Zahab, D. Nakabayashi, V. Jourdain, R. Parret, J.-L. Sauvajol, About the indexing of the structure of single-walled carbon nanotubes from resonant Raman scattering, Adv. Nat. Sci. Nanosci. Nanotechnol. 1 (2011) 045007. doi:10.1088/2043-6262/1/4/045007.
[18] D. Zhang, J. Yang, M. Li, Y. Li, (n , m) Assignments of Metallic Single-Walled Carbon Nanotubes by Raman Spectroscopy: The Importance of Electronic Raman Scattering, ACS Nano. 10 (2016) 10789–10797. doi:10.1021/acsnano.6b04453.
[19] D. Zhang, J. Yang, E.H. Hasdeo, C. Liu, K. Liu, R. Saito, Y. Li, Multiple electronic Raman scatterings in a single metallic carbon nanotube, Phys. Rev. B. 93 (2016) 245428. doi:10.1103/PhysRevB.93.245428.
[20] H. Farhat, S. Berciaud, M. Kalbac, R. Saito, T.F. Heinz, M.S. Dresselhaus, J. Kong, Observation of Electronic Raman Scattering in Metallic Carbon Nanotubes, Phys. Rev. Lett. 107 (2011) 157401. doi:10.1103/PhysRevLett.107.157401.
[21] R. Bruce Weisman, J. Kono, Introduction to Optical Spectroscopy of Single-Wall Carbon Nanotubes, World Sci. Ser. Carbon Nanosci. 9–10 (2019) 1–43. doi:10.1142/9789813235465_0001.
[22] V. Zólyomi, J. Koltai, Á. Rusznyák, J. Kürti, Á. Gali, F. Simon, H. Kuzmany, Á. Szabados, P. Surján, Intershell interaction in double walled carbon nanotubes: Charge transfer and orbital mixing, Phys. Rev. B. 77 (2008) 245403. doi:10.1103/PhysRevB.77.245403.